

AD A067567

DDC FILE COPY

AFAL-TR-77-202

LEVEL II

2



ADVANCED ARCHIVAL MEMORY

Corporate Research and Development
General Electric Company
Schenectady, New York 12301



APRIL 1977

Fourth Interim Report January 16, 1977 - April 15, 1977

Approved for public release; distribution unlimited.

AIR FORCE AVIONICS LABORATORY
AIR FORCE WRIGHT AERONAUTICAL LABORATORIES
AIR FORCE SYSTEMS COMMAND
WRIGHT-PATTERSON AIR FORCE BASE, OHIO 45433

79 04 16 006

NOTICE

When Government drawings, specifications, or other data are used for any purpose other than in connection with a definitely related Government procurement operation, the United States Government thereby incurs no responsibility nor any obligation whatsoever; and the fact that the government may have formulated, furnished, or in any way supplied the said drawings, specifications, or other data, is not to be regarded by implication or otherwise as in any manner licensing the holder or any other person or corporation, or conveying any rights or permission to manufacture, use, or sell any patented invention that may in any way be related thereto.

This report has been reviewed by the Information Office (OI) and is releasable to the National Technical Information Service (NTIS). At NTIS, it will be available to the general public, including foreign nations.

This technical report has been reviewed and is approved for publication.

Millard G. Mier
MILLARD G. MIER
Project Engineer

FOR THE COMMANDER

Robert D. Larson
ROBERT D. LARSON, Chief
Electronic Research Branch
Electronic Technology Division

"If your address has changed, if you wish to be removed from our mailing list, or if the addressee is no longer employed by your organization please notify AFAL(DNR) N-PAPS, ON 45433 to help us maintain a current mailing list".

Copies of this report should not be returned unless return is required by security considerations, contractual obligations, or notice on a specific document.

SECURITY CLASSIFICATION OF THIS PAGE (When Data Entered)

REPORT DOCUMENTATION PAGE		READ INSTRUCTIONS BEFORE COMPLETING FORM
1. TITLE NUMBER	2. GOVT ACCESSION NO.	3. RECIPIENT'S CATALOG NUMBER
4. TITLE (and Subtitle)		5. TYPE OF REPORT & PERIOD COVERED
ADVANCED ARCHIVAL MEMORY		Fourth Interim Report, no Jan. 16, 1977-Apr. 15, 1977
6. AUTHOR		7. PERFORMING ORG. REPORT NUMBER
C. Q./Lemmond, Dr. C.G./Kirkpatrick, J.F./Norton, H.G./Parks, G.E./Possin		16 pnt + 15 apr 77
8. PERFORMING ORGANIZATION NAME AND ADDRESS		9. CONTRACT OR GRANT NUMBER(s)
Corporate Research and Development General Electric Company Schenectady, New York 12301		F33615-76-C-1322, ARPA Order - 3194
10. CONTROLLING OFFICE NAME AND ADDRESS		11. REPORT DATE
Air Force Avionics Laboratory (AFAL/DHR) Wright Patterson Air Force Base, Ohio 45433		APRIL 1977
12. MONITORING AGENCY NAME & ADDRESS (if different from Controlling Office)		13. NUMBER OF PAGES
12-165p.		162
14. DISTRIBUTION STATEMENT (of this Report)		15. SECURITY CLASS. (of this report)
Approved for public release, distribution unlimited.		Unclassified
16. DISTRIBUTION STATEMENT (of the abstract entered in Block 20, if different from Report)		17. DECLASSIFICATION/DOWNGRADING SCHEDULE
18. SUPPLEMENTARY NOTES		
*Prepared for Advanced Research Project Agency under ARPA Order No. 3194.		
19. KEY WORDS (Continue on reverse side if necessary and identify by block number)		
Computer Memory Systems Electron Optics Ion Optics	Ion Implantation Alloy Junction	
20. ABSTRACT (Continue on reverse side if necessary and identify by block number)		
During this reporting period, effort on the Advanced Archival Memory Program included experimental work and theoretical studies on planar diode structures (memory target substrate), ion implantation of inert ions to form sub-micron bit sites, theoretical studies of bit packing density, experimental alloy junction writing using laser and electron beams, and completion of (continued on other side)		

DD FORM 1473
1 JAN 73

SECURITY CLASSIFICATION OF THIS PAGE (When Data Entered)

20. Abstract (continued) *fip*

both electron and ion write optics studies.

Experimental implants were made and bit sites of 0.1 ± 0.05 microns were achieved. Bit packing studies indicate that bits spaced 0.1 microns apart may be possible.

ACCESSION for		White Section <input checked="" type="checkbox"/>
NTIS		Ref Section <input type="checkbox"/>
DQC		
UNCLASSIFIED		
JUSTIFICATION		
BY		
DISTRIBUTION/AVAILABILITY CODES		
Dist	AVAIL	or SPECIAL
<i>A</i>		

PREFACE

→ The objective of this basic research program is to investigate the feasibility of new storage techniques for large archival memories using ion and electron beam with semiconductor targets.

The goal is the development of an archival memory capable of storing 10^{14} to 10^{15} bits with rapid access to the stored information.

(10 to the (14th to 15th) power)

The currently funded effort (Phase I) deals with feasibility studies of key technical areas. The program covers experimental and analytical investigations: (1) to demonstrate the feasibility of ion implanted and alloy junction storage media, (2) to determine the feasibility of beam optics design required for writing/reading on the media, and (3) to select the better of the two storage methods and perform a preliminary paper design of the concept for further development. (cont on p. 2)

This report covers the fourth quarter effort. The three previous quarters were described in reports AFAL-TR-76-213, AFAL-TR-77-35 and AFAL-TR-77-157. During this reporting period, effort on the Advanced Archival Memory Program included experimental work and theoretical studies on planar diode structures (memory target substrates), ion implantation of inert ions to form sub-micron bit sites, theoretical studies of bit packing density, experimental alloy junction writing using laser and electron beams, and completion of both electron and ion write optics studies.

Experimental implants were made and bit sizes of 0.1 \pm 0.05 microns were achieved. Bit packing studies indicate that bits spaced 0.1 microns apart may be possible.

TABLE OF CONTENTS

<u>Section</u>	<u>Page</u>
I INTRODUCTION AND SUMMARY.	1
Bit Packing Density Studies.	3
Planar Diode Studies	3
Ion Writing Experiments.	4
Alloy Junction Writing Experiments	4
Write Optics Study	4
II THEORETICAL STUDIES - BIT PACKING DENSITY	5
Depletion Field Spreading.	5
Ion Beam Scattering During Writing	8
Electron Scattering During Reading	10
Definition of Bit Packing Density Criteria	10
Calculation of G_0	14
Calculation of G_1	18
Effect of the Mode Boundary Condition on Packing Density	23
III THEORETICAL STUDIES - PLANAR DIODE ONE-DIMENSIONAL MODEL.	31
n^+p -Arsenic Planar Diodes.	31
n^+-n-p As^+ Diodes.	37
IV EXPERIMENTAL STUDIES - PLANAR DIODE	49
Germanium Planar Diodes.	49
Silicon Diodes	53
V ION WRITING EXPERIMENTS	63
Discussion of Ion Writing Results.	69
VI ALLOY JUNCTION WRITING EXPERIMENTS.	87
Laser Writing.	87
Electron Writing	93
Summary.	101
VII WRITE OPTICS STUDY.	103
Introduction	103
Optics Study - 3rd Quarter	103
Source Selection	112
Ion Optics Analysis.	117
Beam Deflection	128
Electron Write Optics Analysis	136
Summary.	149
REFERENCES	151

LIST OF ILLUSTRATIONS

<u>Figure</u>		<u>Page</u>
1	Two Approaches for Archival Storage of Information. (a) Ion Implant Method (b) Alloy Junction Method. .	2
2	Idealized Target Geometry	6
3	Maximum Depletion Width for MIS (Metal Insulator Semiconductor) Structures	7
4	Lateral Ion Scattering Model.	9
5a	Grün Range for Silicon and Germanium.	11
5b	Grün Energy Loss Function	11
6	Radial Increase in Electron Beam Spot Size Due to Scattering and Silicon	12
7	Worst Case Bit Patterns (a) Isolated Zero (b) Isolated One.	13
8a	Model Approximation to Isolated Zero.	15
8b	Normalized Gain for the Geometry Shown in Figure 8a	15
9	Calculated Collection Probability vs Depth for an As ⁺ Implanted Sample Profile Shown in Figure 15 . .	17
10	Isolated Zero and One Readout Gain vs Bit Spacing for Ar ⁺ Writing at 50 keV with an As Planar Diode Such as A48A (Figure 15).	19
11	Readout of a Small Written Region	20
12	Effect of Ion Species on Isolated Zero Gain for an Ion Spot Size $S_E = 0.1 \mu$ and a Bit Spacing $W = 0.1 \mu$	22
13	Effect of a Weak Diode Boundary Condition on Readout of Large Bits (a) and Small Bits (b). . . .	26
14	Effect of Beam Current and Diode Bias on the Collection Efficiency of Target AR1-17(1). Elec- tron Beam Energy 2.15 keV. (a) Area Written with 60 keV As ⁺ to $2 \times 10^{12} \text{ cm}^{-2}$ and (b) Unwritten . . .	27

LIST OF ILLUSTRATIONS (Cont'd)

<u>Figure</u>		<u>Page</u>
15	Carrier Density vs Depth for Samples A48A and A22A.	32
16	Measured Surface Conductance vs Silicon Thickness Removed for Sample A48A Fabricated by a 100 keV As ⁺ Implantation Through 800 Å of SiO ₂ . . .	33
17	A Model Calculation of Collection Probability vs Beam Energy Based on the Doping Profile of Sample A48A (Figure 15).	35
18	Measurements of Electron Beam Gain at 2 keV for Samples Fabricated by a 100 keV As ⁺ Implantation Through Various Oxide Thicknesses Compared to Model Predictions	36
19	Model Calculation Based on the Profile of Figure 15 for Sample A48A for the Collection Probability P(z) vs Depth	38
20	Doping Profiles for Typical Planar Diodes -- n ⁺ p (dotted) and n ⁺ -n-p(solid).	39
21	Calculated Collection Probability vs Generation Depth z for the Doping Profiles in Figure 20. . . .	40
22	Measured Collection Efficiency for n ⁺ -n-p Planar Diode 105-7(1) Compared to Prediction of the One-Dimensional Gain Model Assuming the Solid Profile in Figure 20.	41
23a	Collection Efficiency vs Beam Energy Based on Collection Probability Curves of Figure 21 for a n ⁺ -n-p Planar Diode	44
23b	Collection Efficiency at 10 keV from Figure 23a vs Peak Damage Depth d _p	45
24	Cross Section of a Planar Diode Substrate Processed in Lot AR-1	56
25	Gel Permeation Chromatograph of du Pont Elvacite 2041	65
26	Electron Lithographic System Using Video Input to Scanning Electron Microscope	66
27	Resolution Patterns Used with Video Input to Scanning Electron Microscope.	67

LIST OF ILLUSTRATIONS (Cont'd)

<u>Figure</u>		<u>Page</u>
28	Electron Beam Readout of Written Patterns in Sample B13A.	71
29	Secondary Imagery of an Etched 'Hole' in a Metal Film. (a) Secondary Generation as a Function of Beam Position (b) Secondary Signal as a Function of Beam Position	72
30	Electron Beam Readout of Written Patterns in Sample B13A.	75
31	Normalized Gain Data from Sample B13A.	76
32	Electron Beam Readout of Written Patterns in Sample B13D.	78
33	Normalized Gain Data from Sample B13D.	79
34	Electron Beam Readout of Written Patterns in Sample B13D.	81
35	Electron Beam Readout of Written Patterns in Sample A51B.	82
36	Normalized Gain Data from Sample A51B.	83
37	Normalized Gain Data from Sample AR1-17(1)	84
38	Laser Writing Patterns on In-Si Target (SEM) . . .	89
39	Close-up of Laser Irradiated Spot from Line 4. . .	91
40	Planar Diode Current Signal and z Modulated Display from Readout of Line 3 Before Removal of the Indium Layer	92
41	Planar Diode Current Signal and z Modulated Display from Readout of Line 3 After Indium Layer was Removed.	92
42	Secondary Emission Surface Scan of Electron Beam Writing Area	94
43	Planar Diode Current z Modulated Display of Electron Beam Writing Area	94
44	Secondary Electron Surface Scan of Stacking Fault.	96
45	Planar Diode Readout of Stacking Fault in Figure 44.	96

LIST OF ILLUSTRATIONS (Cont'd)

<u>Figure</u>		<u>Page</u>
46	Planar Diode z Modulated Display of Writing Area on 500 Å Au on Si Showing Stacking Fault Readout with Writing Raster Superimposed.	97
47	Etch Pit Formation on Sputtered Au-Si Target-Secondary Emission Surface Scan	99
48	Planar Diode Readout of Etch Pit on Sputtered Au-Si Target.	99
49	Electron Writing Attempts on SiO ₂ -Au-Si Co-sputtered Target @ Thermal Bias: (a) 245°C, (b) 310°C, (c) 320°C, (d) 340°C	100
50	Focused Ion Optics.	106
51	Two-Lens All Magnetic Optics.	107
52	Short Focus Plus Relay Matrix Optics.	108
53	Two-Lens Collimating Optical System	109
54	Three-Lens Optical System	110
55	Electrostatic Lens Characteristics.	113
56	Ion Range Characteristics	118
57	Grün Range vs Landing Potential for Several Materials	119
58	Three-Element Cylinder Lens	122
59	Three-Element Cylinder Lens and Source.	123
60	Spherical Aberration Constants for Lens Types 1 to 5.	125
61	Chromatic Aberration Constants for Lens Types 1 to 5.	126
62	Beam Current vs Spot Size for Focused Ion Optics at Various Magnifications	129
63	Final Lens with Post-Lens Deflection.	130
64	Beam Current vs Spot Size for Deflection Limit on Magnification with Lens #1.	133

LIST OF ILLUSTRATIONS (Cont'd)

<u>Figure</u>		<u>Page</u>
65	Beam Current vs Spot Size for Deflection Limit on Magnification with Lens #2.	134
66	Deflection Aberrations for Ion Optics - 40 kV Neon.	135
67	Low Spherical Aberration Magnetic Lens.	138
68	General Schematic for a Magnetic Lens	139
69	Magnetic Lens Data - Normalized Focal Length, f_o/R , vs Lens Drive, k^2 , for $S/D = 0.2$	140
70	Magnetic Lens Data - Normalized Spherical Aberration Constant, C_s/R , vs Lens Drive, k^2 , for $S/D = 0.2$	141
71	Magnetic Lens Data - Normalized Chromatic Aberration, C_c/R , vs Lens Drive, k^2 , for $S/D = 0.2$	142
72	Beam Current vs Spot Size for a Two-Magnetic-Lens Column at Various Landing Potentials - V_L	144
73	Beam Current vs Spot Size for SFPR Column at Landing Potential of 4000	147

LIST OF TABLES

<u>Table</u>		<u>Page</u>
1	Calculated Lateral Ion Scattering for Inert Ions. .	8
2	Germanium Samples for Planar Diode (n ⁺ p) Studies. .	50
3	Germanium Samples for Planar Diode (n ⁺ p) Studies. .	51
4	Processing Steps for the AR-1 Lot of Archival Targets	57
5	Silicon Material Removed as a Result of Timed Etches.	60
6	Listing of Ion Writing Experiments on Samples with High Resolution Patterns Produced by Electron Beam Lithography (all but As1 samples had back contacts). .	70
7	Electron Source Properties.	104
8	Ions Source Properties.	104
9	Einzel Lens Cases	127
10	Properties of Lenses 1 and 2.	127
11	Parameters at 500 V Peak Deflection	132
12	Magnetic Lens Properties for Maximum Current Column.	145
13	Results of Space Charge Effects	145
14	Estimated Temperature Rise at Target Two- Magnetic Lens Column - S.l.cm/Metal Target, R _g = 500 Å, d = 500 Å	148

SECTION I

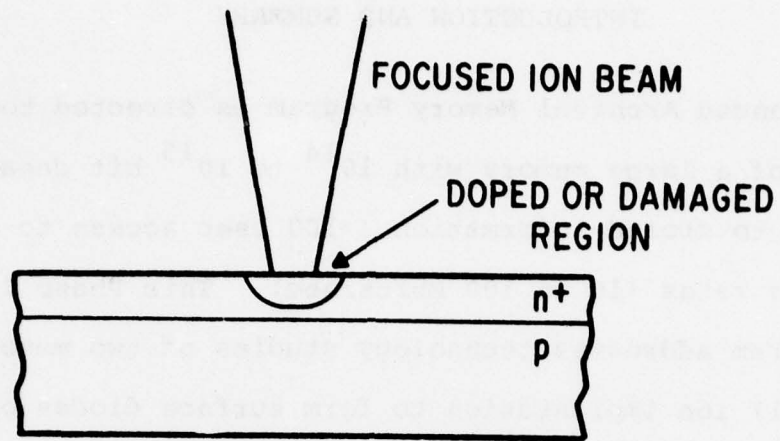
INTRODUCTION AND SUMMARY

The Advanced Archival Memory Program is directed toward the development of a large memory with 10^{14} to 10^{15} bit capacity, with rapid access to stored information (<100 μ sec access to a block) and high data rates (10 to 100 Mbits/sec). This Phase I of the overall program addresses technology studies of two memory approaches: (1) ion implantation to form surface diodes or damage bit sites, and (2) electron beam formed alloy junction surface diodes. These studies include not only memory target physics but also feasibility of the beam optics required to form bit sites by either of the approaches. At the conclusion of the studies, the better of the two storage methods will be selected based on feasibility of the memory target and beam optics, and applicability of such a memory to a large, rapid-access archival memory system.

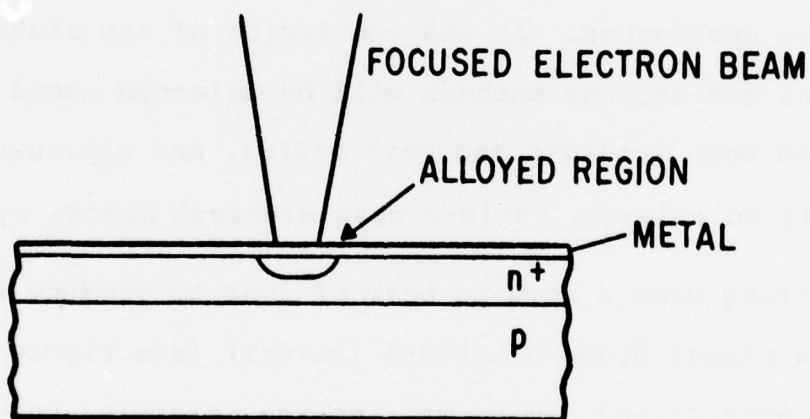
Ion writing uses a focused beam of ions to produce written regions in a planar diode substrate (target) (see Figure 1a). Both dopant writing and damage writing are feasible, however, damage writing is preferred since it requires less ion fluence.

The alloy writing method depends upon the formation of eutectic alloy between a semiconductor and an overlying metal layer as indicated in Figure 1b. By locally heating the device with a focused electron beam, a small alloyed region is formed.

In both cases, the storage is of archival quality, and read-out of the bit sites is by use of an electron beam.



(a)



(b)

Figure 1. Two Approaches for Archival Storage of Information.
 (a) Ion Implant Method (b) Alloy Junction Method

During this quarter of the Advanced Archival Memory Program, a number of technical advances were made and directions for future research established in the following areas:

- Bit packing density
- Planar diode studies
- Ion writing
- Alloy junction writing
- Writing optics studies

BIT PACKING DENSITY STUDIES

A quantitative model for the bit packing density of the planar diode target was developed. The effects of electron beam and ion beam scattering and minority carrier diffusion during reading were included in the model. The ion written regions are modeled as damaged regions, assumed to be a region of very high recombination with zero excess carrier density at the boundary. The studies show that for the present target construction, the modulated read-out signal falls rapidly at about 0.1μ because of lateral carrier diffusion limited by the layer thickness of 0.06μ .

PLANAR DIODE STUDIES

The one-dimensional model developed earlier in the contract was applied to additional anodic oxide profile measurements. The model was also used to study a new planar diode structure ($n^+ - n - p$).

The new diode structure separates the diode depletion region from the surface of the device. It is desirable to separate the depletion region from the surface to reduce leakage current and increase breakdown voltage, and to improve resolution.

Germanium planar structures were fabricated, but the quality was unsatisfactory. Silicon diodes with improved characteristics were produced.

ION WRITING EXPERIMENTS

Lines and spots were implanted and read out with an electron beam demonstrating readout of structures as small as $0.1 \pm 0.05 \mu$. These studies have demonstrated the capability for bit spacings in the 0.2μ range. Bit spacings approaching 0.1μ should be possible with improved target construction.

ALLOY JUNCTION WRITING EXPERIMENTS

Additional laser beam formed alloy junctions indicate that In-Si may be a usable combination, since the low temperature of the eutectic point would be advantageous. Laser writing on this target system was successful. Electron beam writing appears to melt the indium, but eutectic formation of diodes was not observed. Electron beam writing experiments, using a heated sample stage, will continue.

WRITE OPTICS STUDY

Detailed analytical studies of the write optics for both the ion implant and the alloy junction approach were completed. This report contains a comprehensive description of these studies, and concludes that optical systems for both writing approaches are feasible.

Section II

THEORETICAL STUDIES - BIT PACKING DENSITY

A quantitative model for the bit packing density of the planar diode target was developed during this reporting period. The effects of electron beam and ion beam scattering and minority carrier diffusion during reading were included in the model. The ion written regions are modeled as damaged regions of depth R_D and lateral dimensions are determined by the writing ion beam (Figure 2). The written region is assumed to be a region of very high recombination with zero excess carrier density at the boundary.

DEPLETION FIELD SPREADING

This was discussed in the First Quarterly Report for the case of doping writing. For damage writing, it is not clear how severe these effects are. One effect of damage writing is carrier compensation; thus the written area tends to become intrinsic, and depletion field spreading occurs. However, the dominant effect is believed to be increased recombination so that, at the low writing fluences contemplated here (10^{11} to 10^{12} cm^{-2}), carrier compensation should not be significant.

In the worst case, the written region could become intrinsic. Then depletion layer formation would be primarily determined by the surface charge on the device. If the layer below the compensated (written) region is uniformly doped, then the maximum depth of the depletion layer is as shown in Figure 3 [1]. For the currently designed devices, the doping in this region is $\sim 10^{18}$ cm^{-3} , so the effect is small, even in the worst case. It is planned to

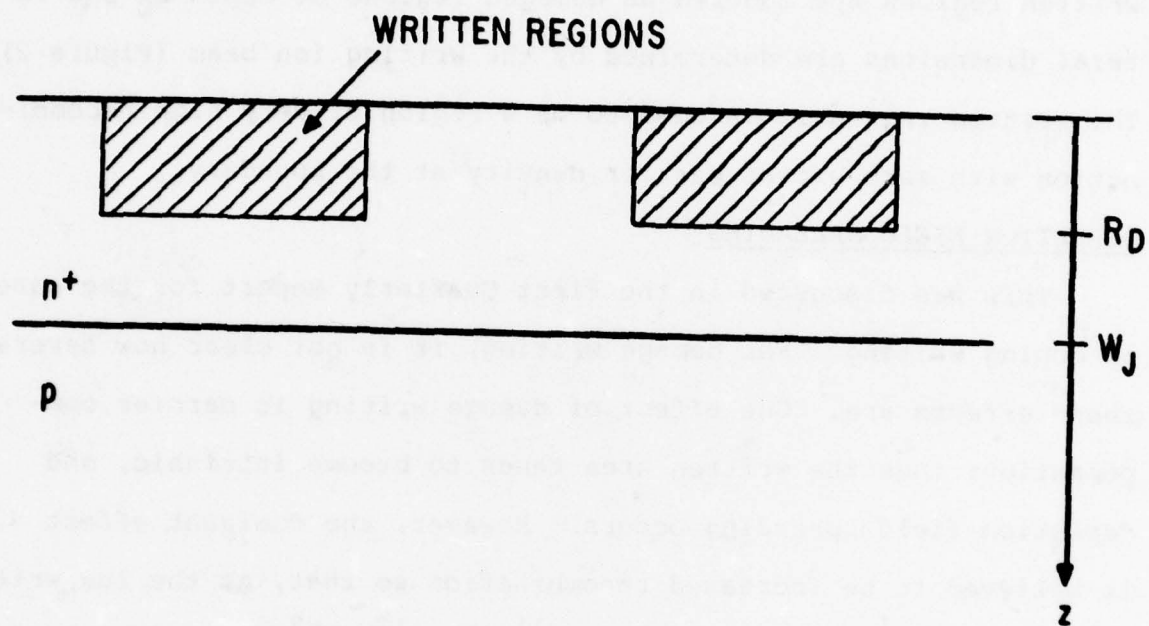


Figure 2. Idealized Target Geometry

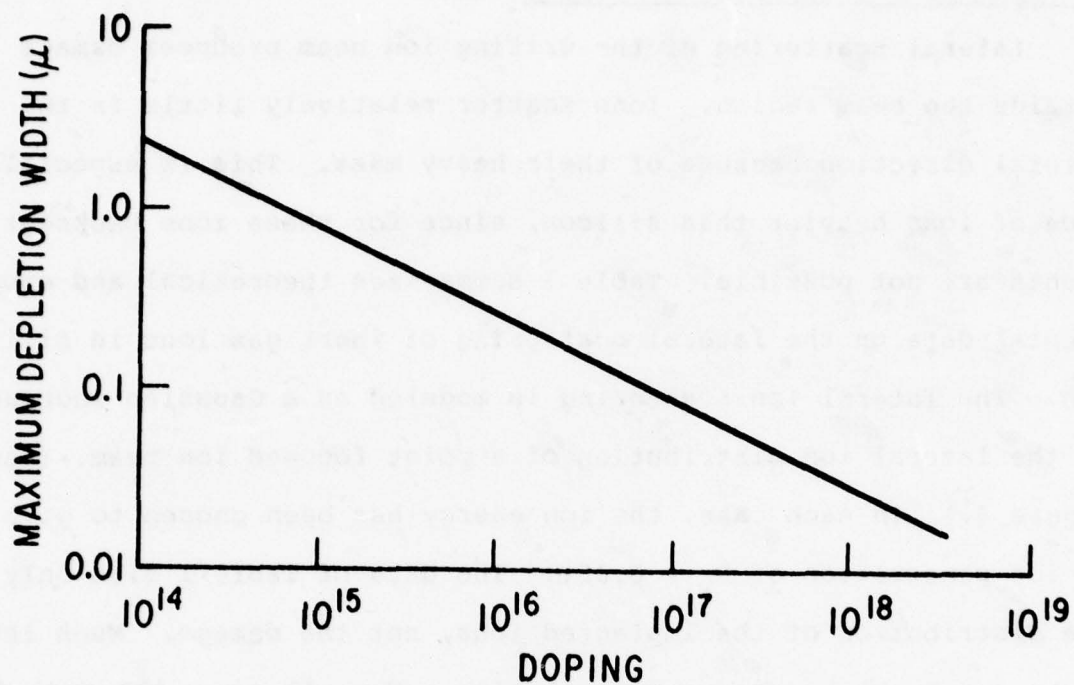


Figure 3. Maximum Depletion Width for MIS (Metal Insulator Semiconductor) Structures

investigate this further by measuring the effect of doping on resolution. In the present analysis, depletion field spreading is neglected.

ION BEAM SCATTERING DURING WRITING

Lateral scattering of the writing ion beam produces damage outside the beam region. Ions scatter relatively little in the lateral direction because of their heavy mass. This is especially true of ions heavier than silicon, since for these ions backscatter events are not possible. Table 1 summarizes theoretical and experimental data on the lateral scattering of inert gas ions in silicon. The lateral ion scattering is modeled as a Gaussian increase in the lateral ion distribution of a point focused ion beam. (See Figure 4.) In each case, the ion energy has been chosen to give an ion penetration of $R_p = 0.05\mu$. The data of Table 1 give only the distribution of the implanted ions, not the damage. Much less is known about the damage distribution. For all ions, the peak in

TABLE 1

CALCULATED LATERAL ION SCATTERING FOR INERT IONS

Ion	Energy (keV)	Calculated Lateral Ion Scattering σ_I (μ)
Ne ⁺	25	0.0375
Ar ⁺	50	0.0231
Kr ⁺	90	0.0175
Xe ⁺	115	0.0121

Note: Inert ions at energies for an estimated projected range = 0.05μ [2]

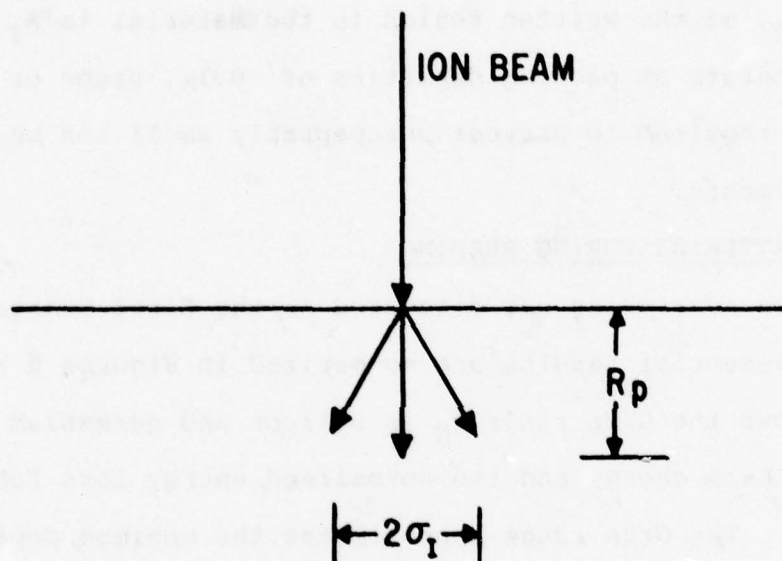


Figure 4. Lateral Ion Scattering Model

the damage distribution should lag the peak in the ion distribution, i.e., the damage depth and scatter should be less than the ion depth and scatter. Hence, the ion scattering estimates in Table 1 will tend to overestimate the width of the damage distribution.

To illustrate the effect of ion scattering on packing density, let S_I be the diameter of the incident writing ion beam. Then the diameter, W_I , of the written region in the material is $S_I + 2\sigma_I = W_I$. To operate at packing densities of $\sim 0.1\mu$, argon or heavier ions may be required to prevent unacceptably small ion beam spot size requirements.

ELECTRON SCATTERING DURING READING

Electron scattering was discussed in the First Quarterly Report. The essential results are summarized in Figures 5 and 6. Figure 5 shows the Grün range R_G in silicon and germanium as a function of beam energy and the normalized energy loss function λ (Figure 5b). The Grün range approximates the maximum depth of energy generation; about 98% of the beam energy is generated at depths $z \leq R_G$. The lateral scattering of a sharp edged beam is σ_E . This is plotted in Figure 6 vs beam energy for silicon. If S_E is the spot size of the incident reading electron beam, then $W_E = 2\sigma_E + S_E$, where W_E is the diameter of the ionization region in the silicon. Hence to permit reading 0.1μ patterns, beam energies ≤ 2.5 keV are required.

DEFINITION OF BIT PACKING DENSITY CRITERIA

The readout gain difference between the two worst case patterns is a good bit packing density criterion (Figure 7). These

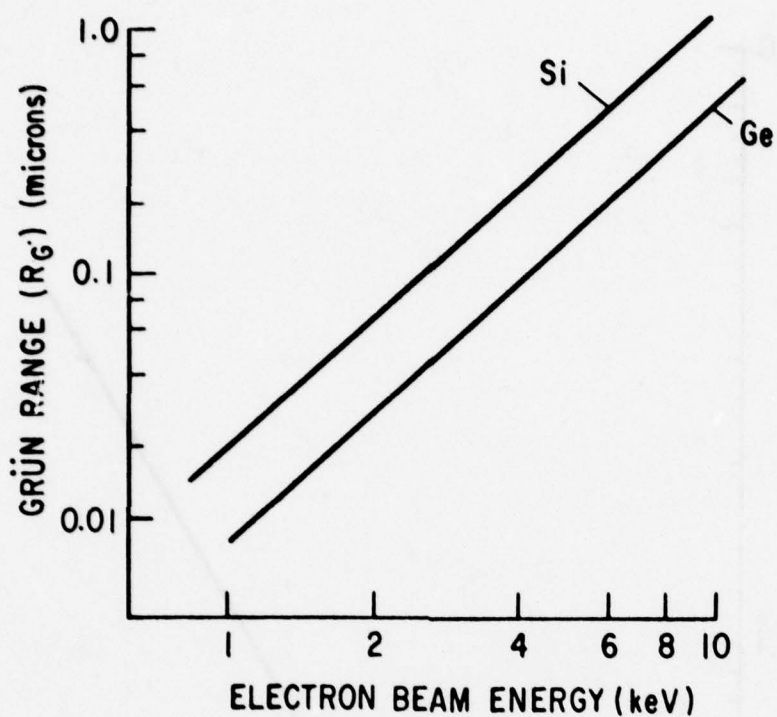


Figure 5a. Grün Range for Silicon and Germanium

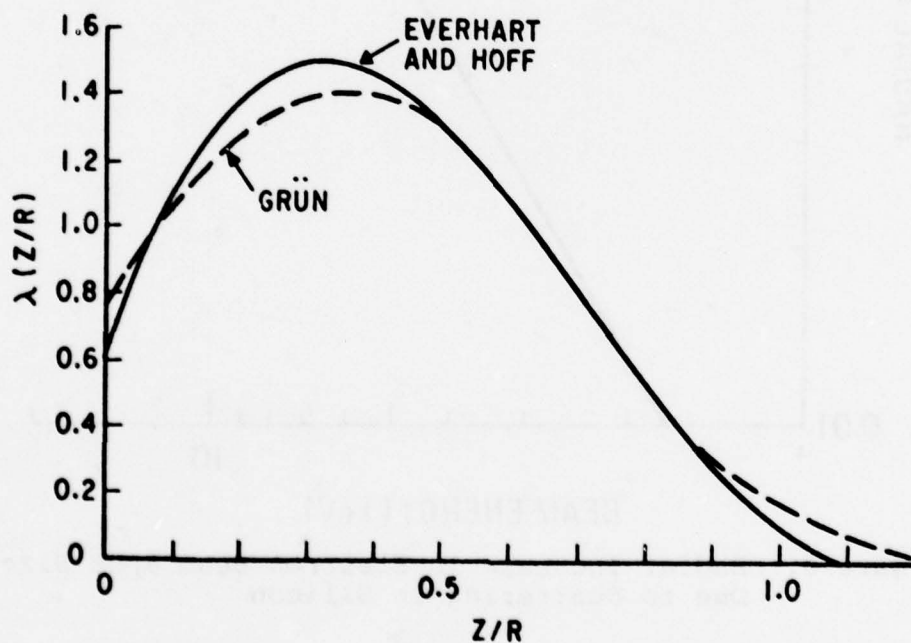


Figure 5b. Grün Energy Loss Function

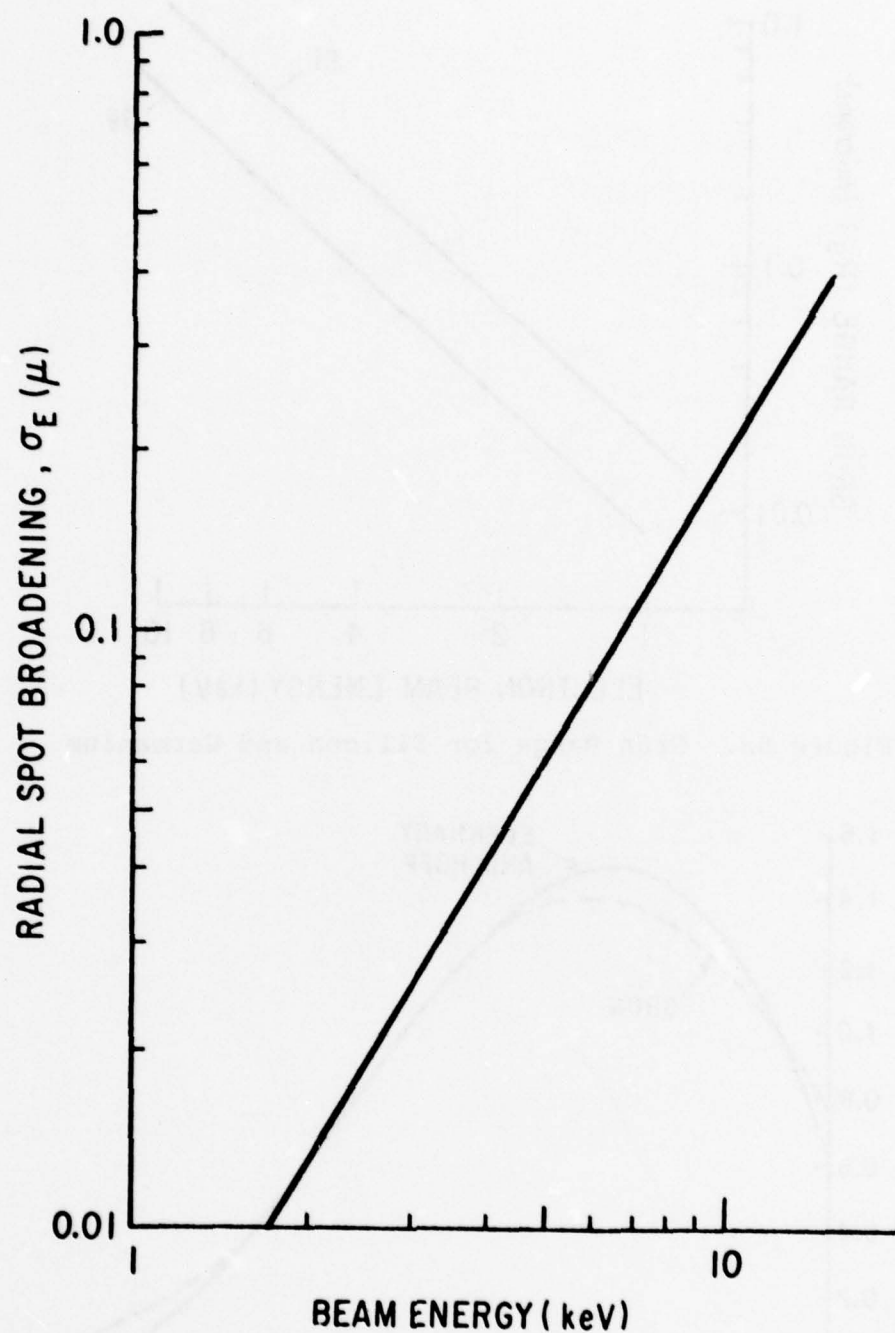
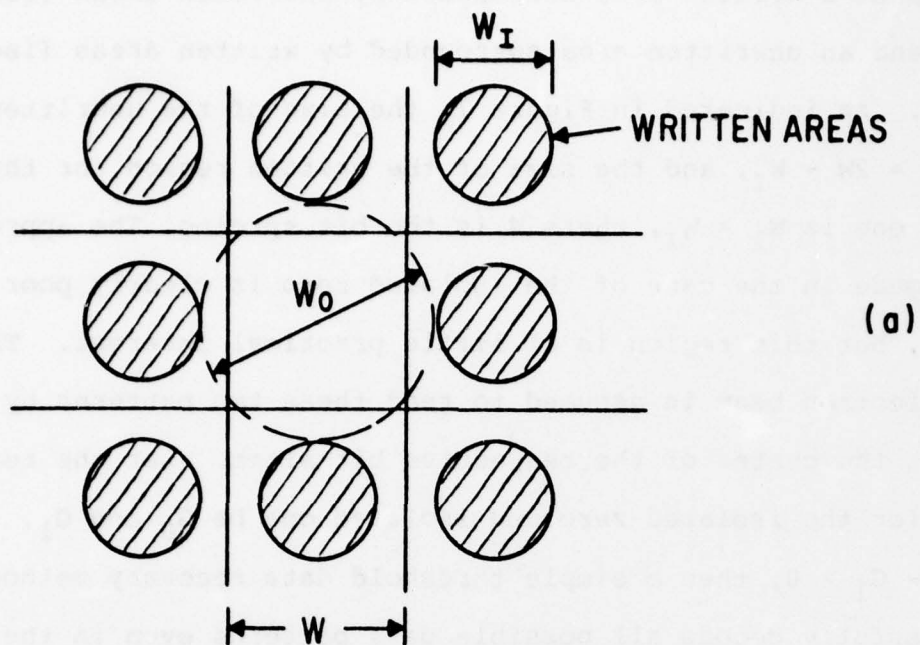
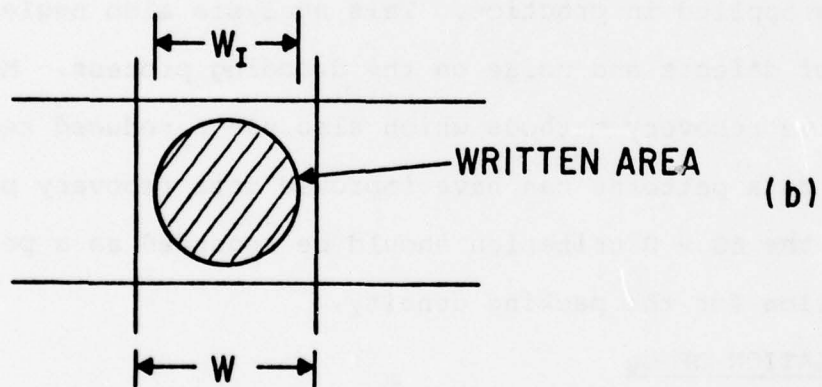


Figure 6. Radial Increase in Electron Beam Spot Size Due to Scattering in Silicon



(a)



(b)

Figure 7. Worst Case Bit Patterns

- (a) Isolated Zero
- (b) Isolated One

represent a written area surrounded by unwritten areas (isolated one) and an unwritten area surrounded by written areas (isolated zero). As indicated in Figure 7, the size of the unwritten region is $W_0 = 2W - W_I$, and the size of the written region for the isolated one is $W_1 = W_I$, where W is the bit spacing. The approximation made in the case of the isolated zero is clearly poor if $W_I \ll W_1$, but this region is of little practical interest. The reading electron beam is assumed to read these two patterns by dwelling at the center of the respective bit sites. Let the readout gain for the isolated zero and isolated one be G_0 and G_1 . If $\Delta G = G_0 - G_1 > 0$, then a simple threshold data recovery method could successfully decode all possible data patterns even in the presence of cross talk between adjacent lines. It is important to recognize that the threshold detection method is crude and would not be applied in practice. This analysis also neglects the effect of defects and noise on the decoding process. More complex adaptive recovery methods which also use a reduced set of permissible data patterns can have improved data recovery properties. Hence the $\Delta G > 0$ criterion should be regarded as a pessimistic criterion for the packing density.

CALCULATION OF G_0

Figure 8 shows the results of the minority carrier diffusion equation solution described in the First Quarterly Report. The geometry of the calculation is appropriate for the isolated zero pattern (Figure 8a). The minority carrier generation is at a point source of depth D . The normalized readout gain (Figure 8b) will

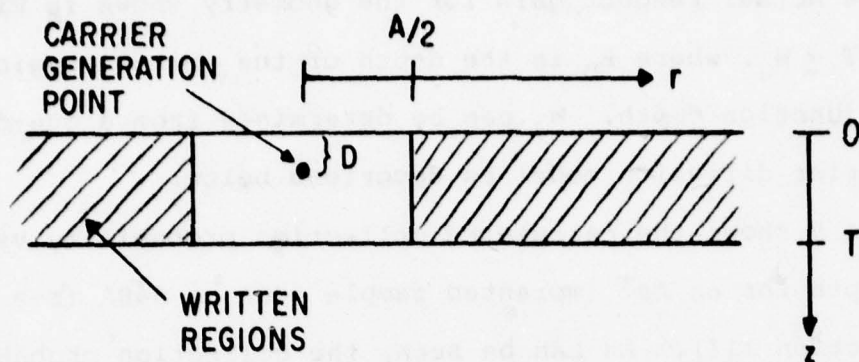


Figure 8a. Model Approximation to Isolated Zero

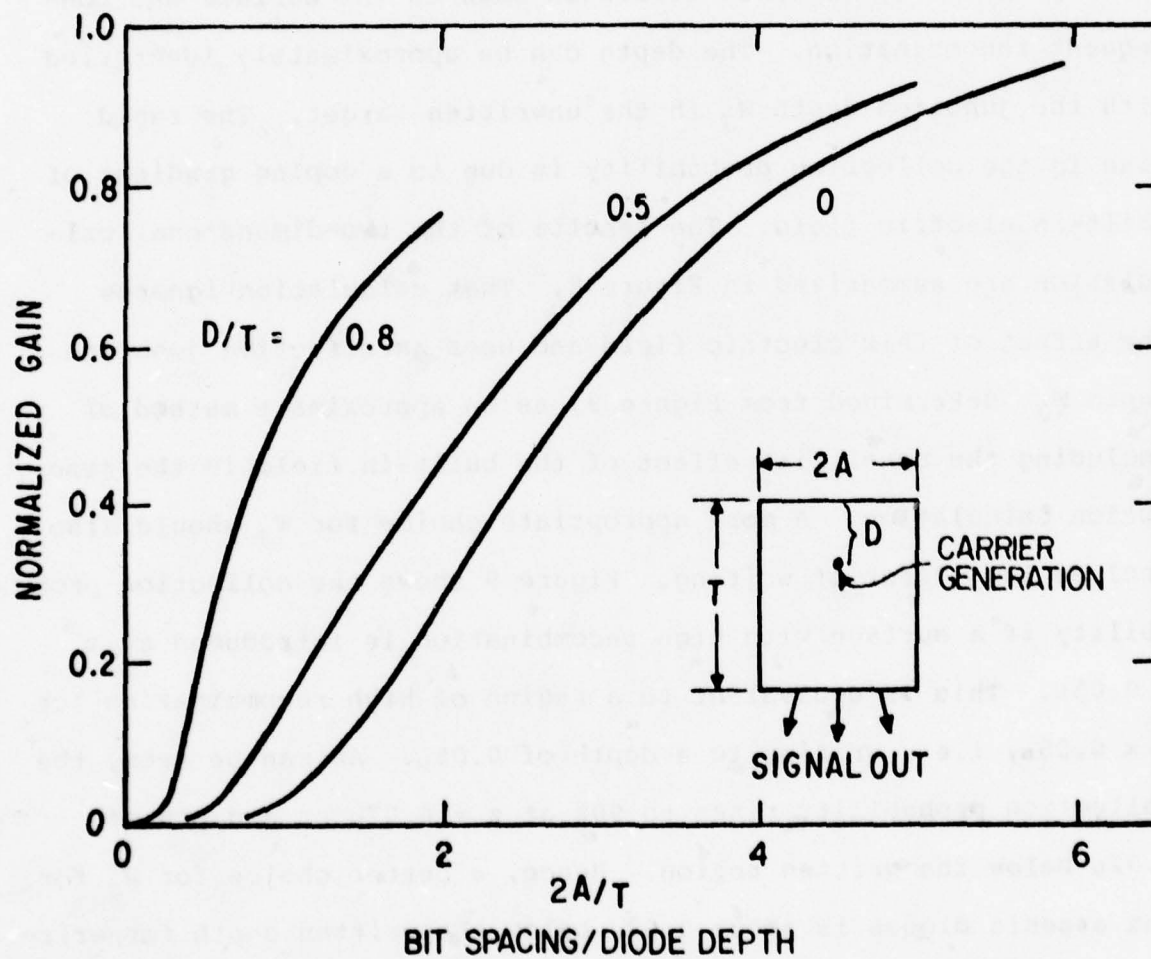


Figure 8b. Normalized Gain for the Geometry Shown in Figure 8a

bracket the actual readout gain for the geometry shown in Figure 2 if $R_D \leq T \leq W_J$, where R_D is the depth of the written regions and W_J is the junction depth. W_J can be determined from a one-dimensional carrier diffusion model as described below.

Figure 9 shows the calculated collection probability vs generation depth for an As^+ implanted sample such as A48A (see Figure 15, Section III). As can be seen, the collection probability rises to 90% at $z = 0.056\mu$. At this depth, the carriers have a small probability (10%) of diffusion back to the surface and consequent recombination. The depth can be approximately identified with the junction depth W_J in the unwritten target. The rapid rise in the collection probability is due to a doping gradient of built-in electric field. The results of the two-dimensional calculation are summarized in Figure 8. That calculation ignores the effect of this electric field and uses an effective junction depth W_J , determined from Figure 9, as an approximate method of including the beneficial effect of the built-in field in the resolution calculation. A more appropriate choice for W_J should also include the effect of writing. Figure 9 shows the collection probability if a surface with high recombination is introduced at $z = 0.05\mu$. This is equivalent to a region of high recombination for $z < 0.05\mu$, i.e., writing to a depth of 0.05μ . As can be seen, the collection probability rises to 90% at $z = 0.07\mu$ or a depth of 0.02μ below the written region. Hence, a better choice for W_J for the arsenic diodes is about 0.02μ below the written depth for writing depths of $\approx 0.05\mu$. For writing to a depth of 0.05μ , as in Table 1, $W_J = 0.07\mu$.

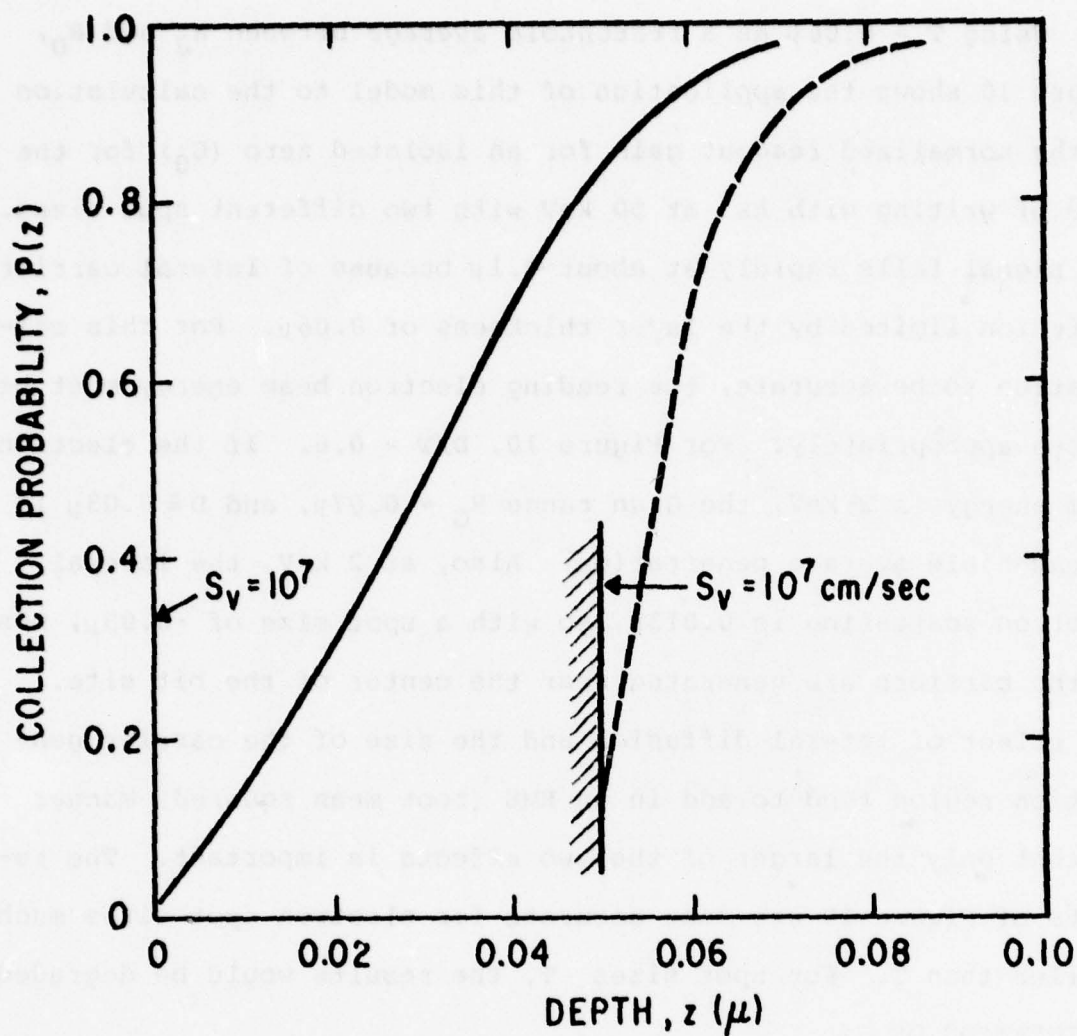


Figure 9. Calculated Collection Probability vs Depth for an As^+ Implanted Sample Profile Shown in Figure 15. (Solid curve unwritten and dotted curve simulating the effect of writing by introducing a high recombination surface at 0.05μ .)

Using $T = 0.06\mu$ as a reasonable average between W_J and R_D , Figure 10 shows the application of this model to the calculation of the normalized readout gain for an isolated zero (G_0) for the case of writing with As^+ at 50 keV with two different spot sizes. The signal falls rapidly at about 0.1μ because of lateral carrier diffusion limited by the layer thickness of 0.06μ . For this calculation to be accurate, the reading electron beam energy must be chosen appropriately. For Figure 10, $D/T = 0.6$. If the electron beam energy is 2 keV, the Grün range $R_G = 0.07\mu$, and $D \approx 0.03\mu$ is a reasonable average penetration. Also, at 2 keV, the lateral electron scattering is 0.013μ , so with a spot size of $\sim 0.05\mu$, most of the carriers are generated near the center of the bit site. The effect of lateral diffusion and the size of the carrier generation region tend to add in an RMS (root mean squared) manner so that only the larger of the two effects is important. The results of Figure 10 are most accurate for electron spot sizes much smaller than T . For spot sizes T , the results would be degraded.

CALCULATION OF G_1

The dotted lines in Figure 10 show the normalized readout gain calculated for an isolated one (G_1). For large bit sizes, this can be calculated from the one-dimensional model. For a 2 keV electron beam and heavy writing to a depth of 0.05μ , G_0 can be much less than 0.01 for large written areas. As the size of the written area is reduced and $d_1 \approx d_2$, carriers can begin to escape laterally as indicated in Figure 11. Hence, when $S_E + 2\sigma_E = W_1 = S_I + 2\sigma_I$, G_1 will begin to depart significantly from its minimum value. This is indicated in Figure 9 for an electron spot

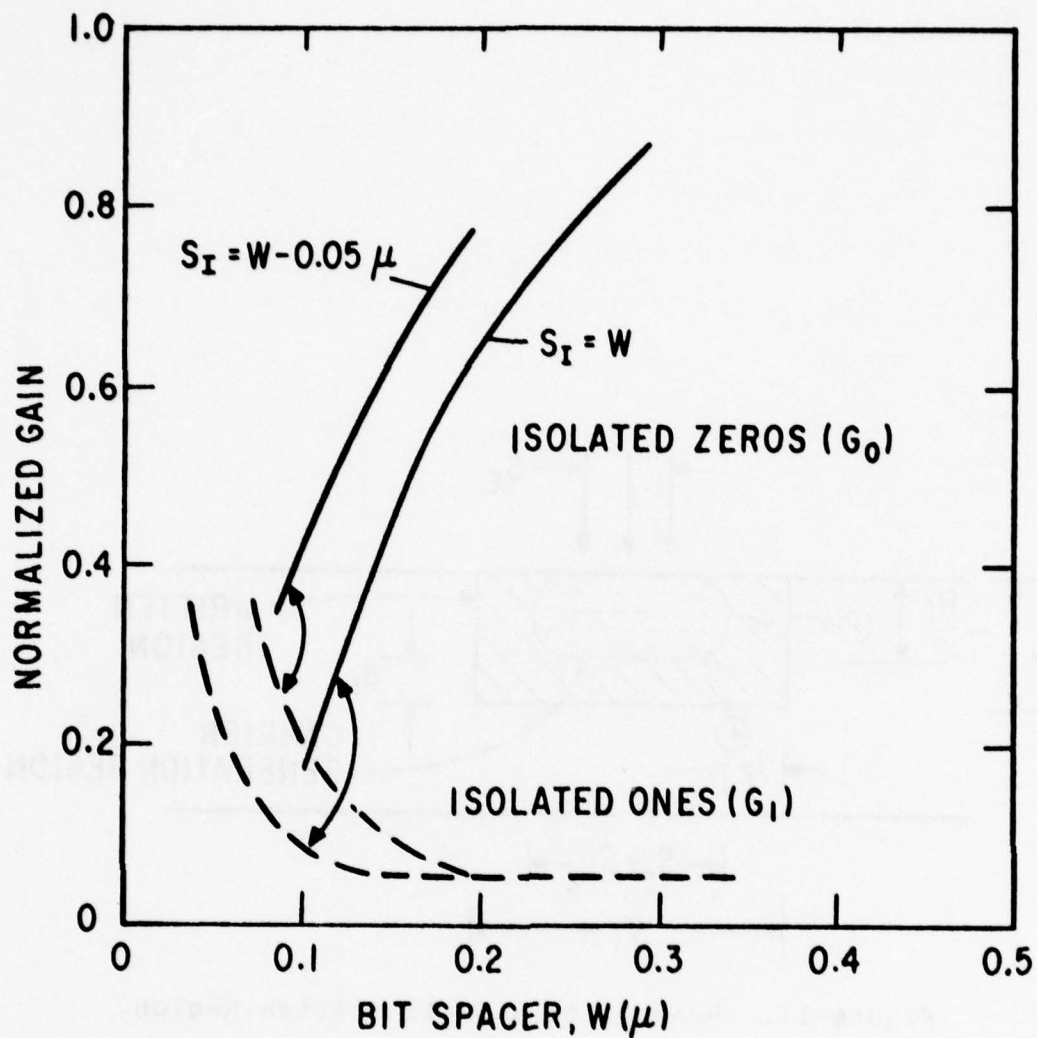


Figure 10. Isolated Zero and One Readout Gain vs Bit Spacing for Ar^+ Writing at 50 keV with an As Planar Diode Such as A48A (Figure 15)

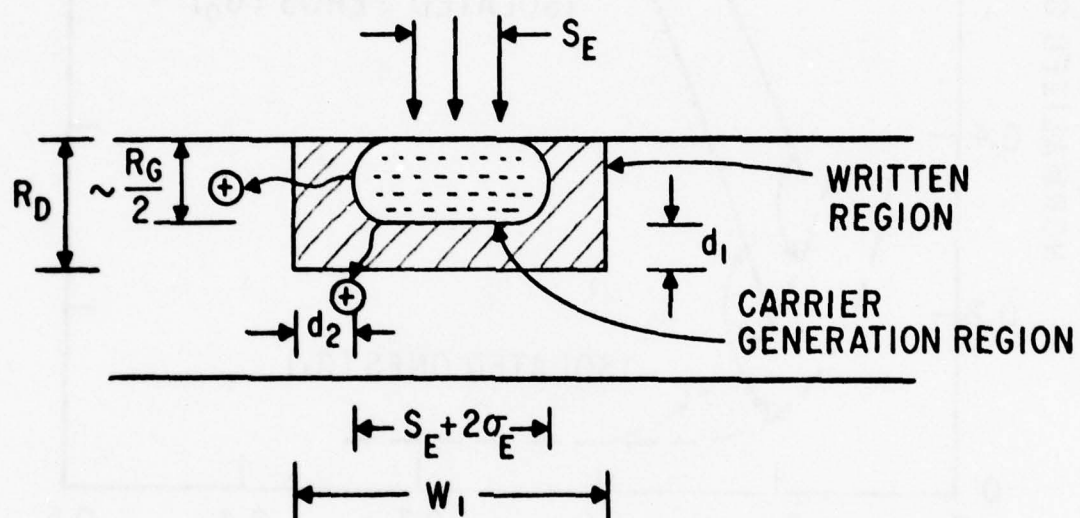


Figure 11. Readout of a Small Written Region

size $S_E = 0.05\mu$. The important concept is that resolution behavior of the isolated one should be much better than the zero, because lateral diffusion effects are minimized by the high recombination in the isolated one or written region. All gains in Figure 9 are normalized to the maximum gain for a large unwritten area. For the As^+ implanted diodes such as A48A, this gain is 250 at 2 keV. (See Figure 17, Section III.)

The effects of ion species and spot size on resolution are shown in Figure 12. The calculated isolated zero gain is plotted vs spot size for the four intermediate inert gas ions. Essentially the same assumptions were used as in Figure 9, and the bit spacing was 0.1μ . Note the relatively poor performance of Ne^+ because of its much larger lateral scattering. At larger bit spacing, the advantage of the heavier gas ions would be less pronounced.

From these results, the present target design based on As^+ implantation through oxides and low temperature annealing should enable marginal operation at 0.1μ bit spacing. Writing ions heavier than neon are preferable for 0.1μ bit spacing, but ions as light as neon are suitable for bit spacings in the 0.2μ region. Improvements in target performance could be achieved by a reduction in ion scattering or a reduction in lateral carrier diffusion during reading. Ion scatter can be reduced by the use of heavier ions such as krypton or xenon or lower ion energies. Lower ion energies will require reduced electron beam energies for effective readout. In the case of the arsenic diodes, removal of the flat-top part of the profile could also be beneficial, especially if coupled with reduced writing ion penetration. The flat-topped

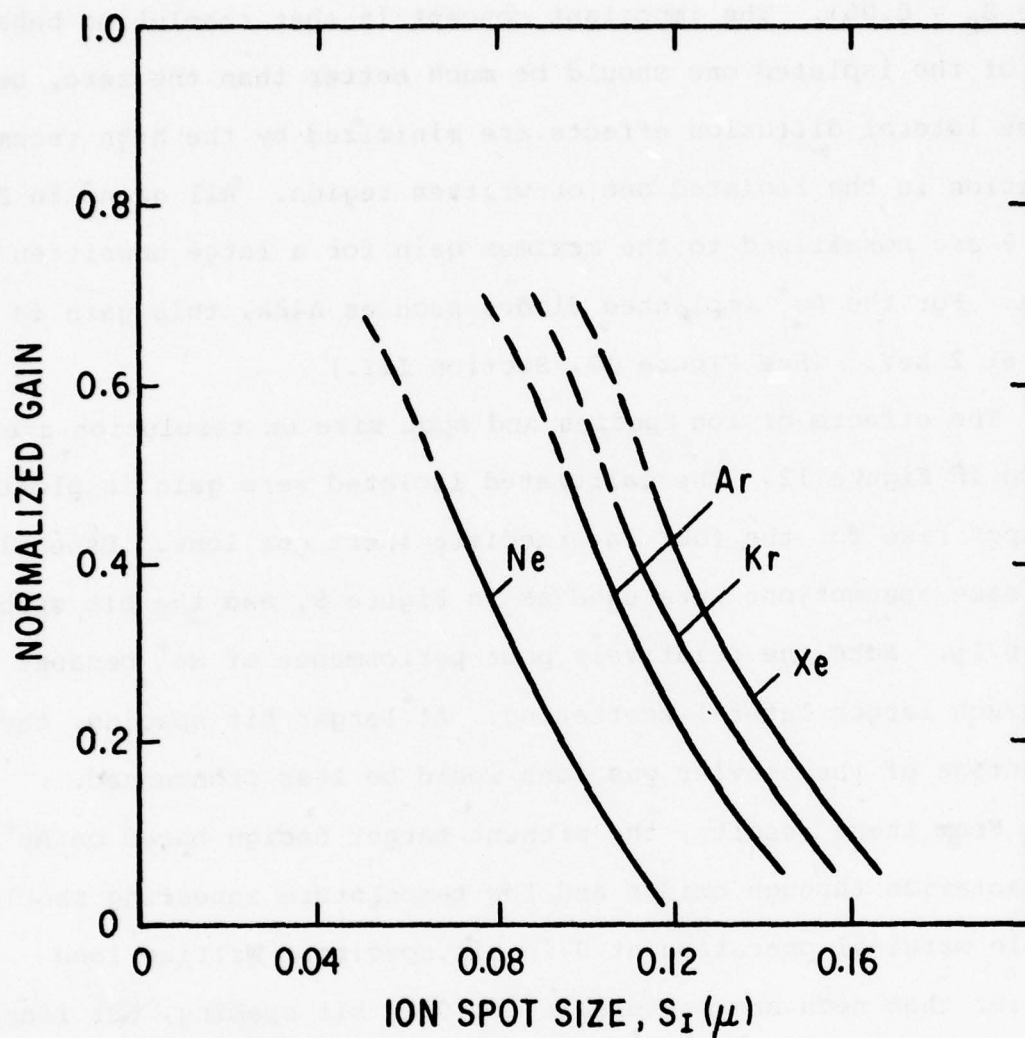


Figure 12. Effect of Ion Species on Isolated Zero Gain for an Ion Spot Size $S_E = 0.1 \mu$ and a Bit Spacing $W = 0.1 \mu$. (Essentially same assumptions as for Figure 8.)

part of the profile permits more lateral carrier diffusion than would a profile with a steep doping gradient extending to the surface because of the absence of the built-in electric field. As can be seen in Figure 9, the collection probability does not reach 90% until $z = 0.056 \mu$, so that T in Figure 8 must always be greater than 0.056μ independent of the writing depth. However, if 0.05μ of silicon were removed, then the collection probability would follow the dotted curve and, with a shallow writing depth $R_0 \sim 0.02 \mu$, then T in Figure 8 should satisfy $0.02 \mu \leq T \leq 0.04 \mu$ or $T \sim 0.03 \mu$. This would result in an approximate factor of 2 improvement in packing density. An important effort during Phase II will be an experimental study of the effect of reduced writing depths and controlled silicon removal on the packing density.

EFFECT OF THE MODE BOUNDARY CONDITION ON PACKING DENSITY

In all of the planar diode models discussed, the boundary condition at the diode depletion region has been taken as:

$$\delta p = 0 \quad (1)$$

where δp is the density of excess minority carriers. A more general boundary condition would be:

$$J_p = q S_D \delta p \quad (2)$$

where S_D is the so-called collection velocity of the diode. Equation (2) is essentially the same as the definition of the surface recombination velocity boundary condition used at the oxide interface. It can be argued that the maximum collection velocity is $1/2 V_{th}$, where V_{th} is the thermal velocity for the minority carriers:

$$V_{th} = (8k_B T / \pi m^*)^{1/2} \quad (3)$$

(See [1].)

For holes in silicon, $V_{th} = 1.5 \times 10^7$ cm/sec, and for electrons, $V_{th} = 1.25 \times 10^7$ cm/sec. The calculation in [1] is based on a field-free region of the semiconductor with a perfectly collecting boundary (i.e., a boundary which does not reflect any carriers). Electric fields in the boundary region may result in a larger or smaller S_D depending upon the field direction. According to a calculation by Card [3], ohmic contacts in silicon can have collection velocities as high as 10^9 cm/sec.

Solutions to the diffusion equation have the property that carriers will not be collected with high efficiency by the diode boundary unless

$$S_D T/D \gg 1 \quad (4)$$

where T is the n -layer thickness as defined in Figure 8a. Another way of looking at this is that the carriers diffuse laterally a distance ℓ along the diode boundary before being collected by the diode. The distance ℓ is given by

$$S_D \ell/D \approx 1 \quad (5)$$

Equations (4) and (5) are essentially equivalent, since for good resolution, $W \sim 3T$ and $\ell \ll W$, where W is the bit spacing. Hence the requirement on S_D is:

$$S_D \geq 10D/W \quad (6)$$

For 0.1μ bit spacing, $S_D \geq 10^7$ cm/sec, which is within the range discussed previously.

The above discussion has treated an idealized semiconductor without defects. During readout there will be an excess of holes in the n -region, and these will tend to increase the positive charge density in any slow traps in the n -region near the junction.

These charged traps will produce a repulsive field towards the surface, thereby reducing the collection efficiency of the diode. This could have severe effects on the packing density.

One way to experimentally test the hypothesis that the collection velocity at the diode boundary does not satisfy Eq. (4) is to measure the readout gain of large written target areas as a function of diode bias and beam current. If S_D is a range such that $S_D T/D \leq 1$, then changes in S_D may affect the readout gain. The dependence will be strongest in the written target areas because carriers not collected by the diode can be collected by the written region. This is shown schematically in Figure 13, where the random walk motion of the carrier path is suppressed for clarity. Figure 13a is for large bits. Note that the gain is not reduced in the unwritten areas (where the recombination at the top surface is low) because the carrier is ultimately collected by the diode. Figure 13b shows the effect for small bit spacings. Here readout of an unwritten area is degraded because some carriers that would be collected by the diode (if the collection velocity were high) are reflected and collected by an adjacent written area.

Figure 14 shows the collection efficiency of target AR1-17(1) written with 60 keV As^+ at $2.10^{12} \text{ cm}^{-2}$. This is a target fabricated by As^+ implantation through an 800 Å thick oxide. A target from this same processed lot had the worst resolution of any target so far studied. Figure 14a shows the dependence on diode bias and beam current at 2.15 keV for the written area and Figure 14b for the unwritten area. Note that, as predicted, there is almost no effect for the unwritten area. The small dependence on beam

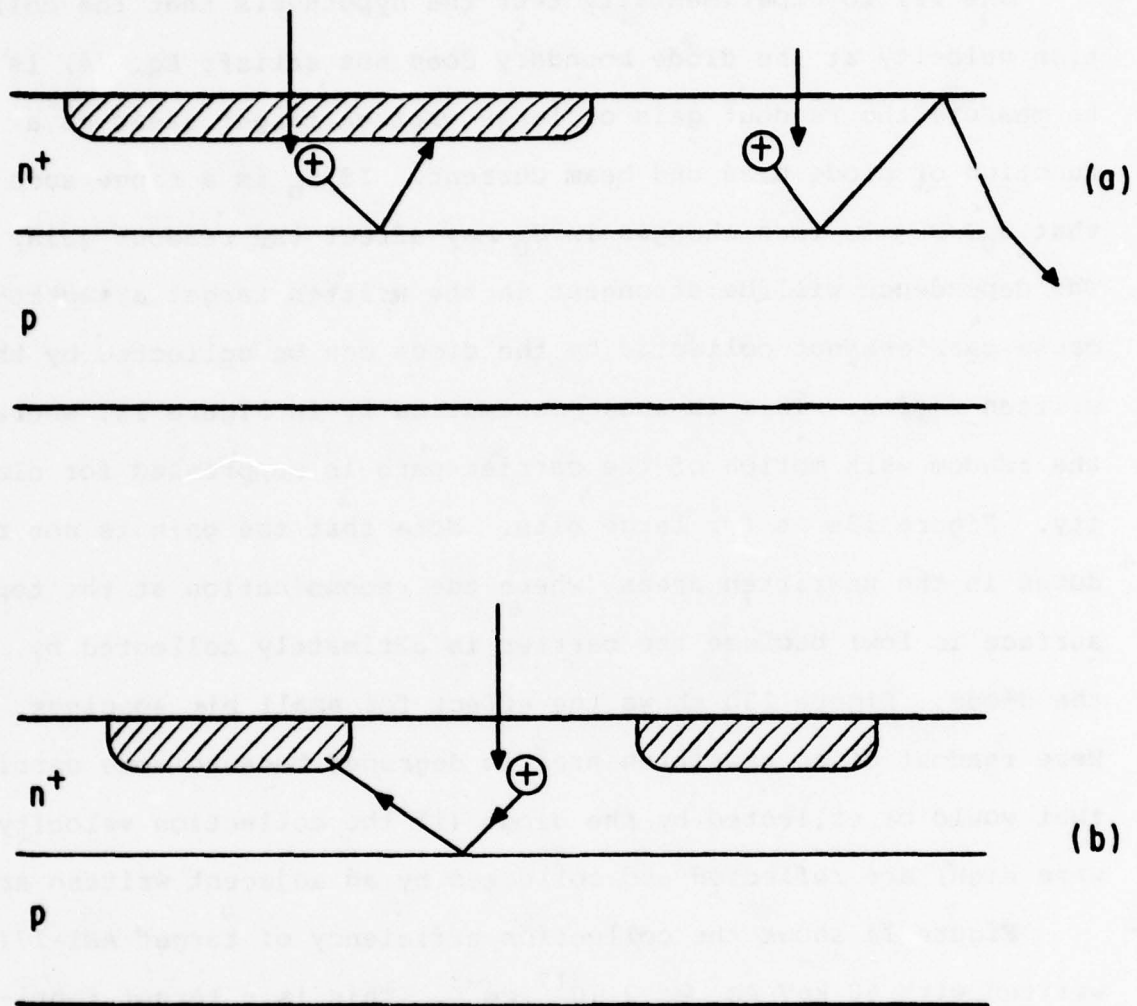


Figure 13. Effect of a Weak Diode Boundary Condition on Readout of Large Bits (a) and Small Bits (b)

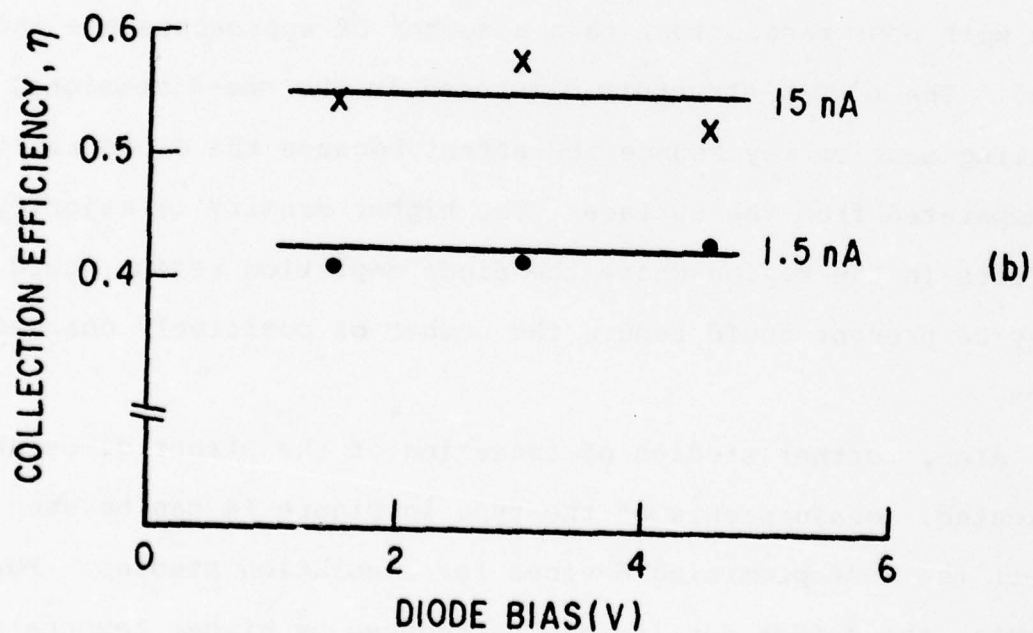
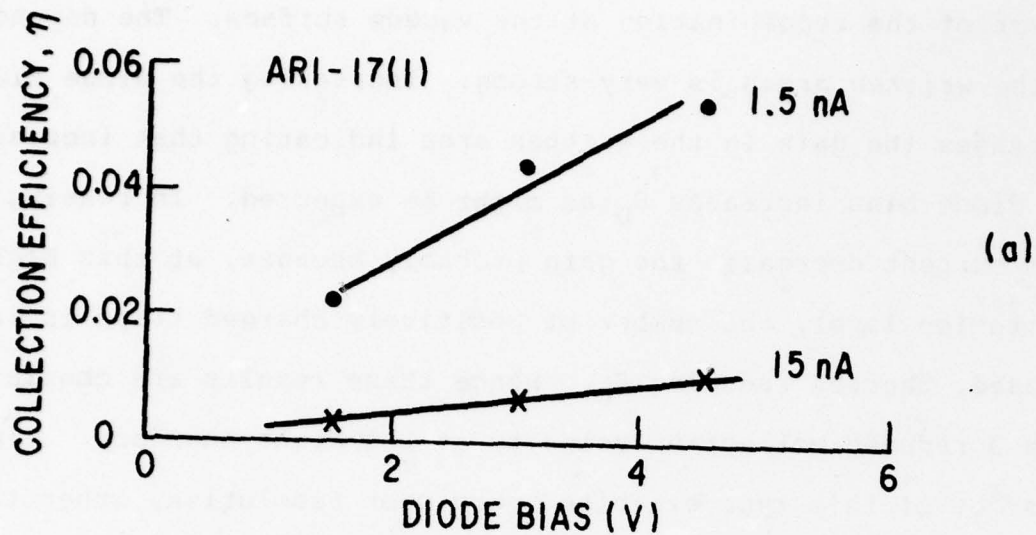


Figure 14. Effect of Beam Current and Diode Bias on the Collection Efficiency of Target ARI-17(1). Electron Beam Energy 2.15 keV. (a) Area Written with 60 keV As^+ to $2 \times 10^{12} \text{ cm}^{-2}$ and (b) Unwritten

current may have been due to measurement errors or a saturation effect of the recombination at the vacuum surface. The dependence in the written areas is very strong. Increasing the diode bias increases the gain in the written area indicating that increasing the diode bias increases S_D as might be expected. Increasing the beam current decreases the gain probably because, at this higher excitation level, the number of positively charged traps is increased, thereby reducing S_D . Hence these results are consistent with a reduced collection velocity at the diode boundary. Since a target of this type exhibited very poor resolution, other targets might be expected to exhibit the effect shown in Figure 14a to a much lesser degree.

If the behavior observed in Figure 14 can be shown to correlate with poor resolution, then a number of approaches are indicated. The n^+-n-p structure discussed in the one-dimensional modeling section may reduce the effect because the diode region is separated from the surface. The higher density of majority carriers in the region where the diode depletion region would normally be present could reduce the number of positively charged traps.

Also, further studies of annealing of the planar diode are indicated. Measurements of the type in Figure 14 can be used to detect the most promising devices for resolution studies. For example, the defect density can be reduced by higher temperature annealing or driving the implanted layer amorphous by silicon or inert gas implant and then regrowing it at low temperatures ($\approx 600^\circ\text{C}$). Knock-on oxygen atoms due to implantation through the

oxide layer may be contributing to the defect density. Since a lighter ion like boron does not knock in the oxygen atoms as deeply, boron diodes could be better. This may explain why the boron diodes generally gave better resolution. If oxygen knock-ons prove to be a problem, it may be necessary to adjust the doping profile by implantation into bare silicon and controlled removal of silicon by silicon etch or anodic oxidation.

SECTION III

THEORETICAL STUDIES - PLANAR DIODE ONE-DIMENSIONAL MODEL

During the fourth quarter, the one-dimensional model developed during the first part of the contract was applied to additional anodic oxide profile data and to a study of a new planar diode structure (n^+ -n-p).

n^+ p-ARSENIC PLANAR DIODES

Figure 15 shows the carrier density profile for sample A48A measured by anodic oxidation and four-point probe. This technique was described in the first two quarterly reports. For reference, the raw conductance data for the same sample is shown in Figure 16. Sample A48A was prepared by a 100 keV As^+ implantation through 800 Å of thermal SiO_2 into silicon and annealed at 800°C for 1 hour in argon. This is compared to an earlier measurement on sample A22A which was prepared by the same implantation and similar annealing conditions (770°C), except that the implantation was into bare silicon. The profile has been intentionally displaced 0.08μ to allow for the stopping power of the oxide layer. As can be seen, the effect of the oxide during implant is more complicated than simply stripping 0.08μ of silicon from the A22A profile. This simple assumption was based on the experimental data of Schwettmann [4] and was used in previously reported work. The reduced tailing of the profile at large depths may be due to the amorphous character of the oxide layer which prevents channeling effects. The shape of the profile near the surface is not understood but may be related to defects related to knock-on oxygen from the oxide layer or out-diffusion of arsenic.

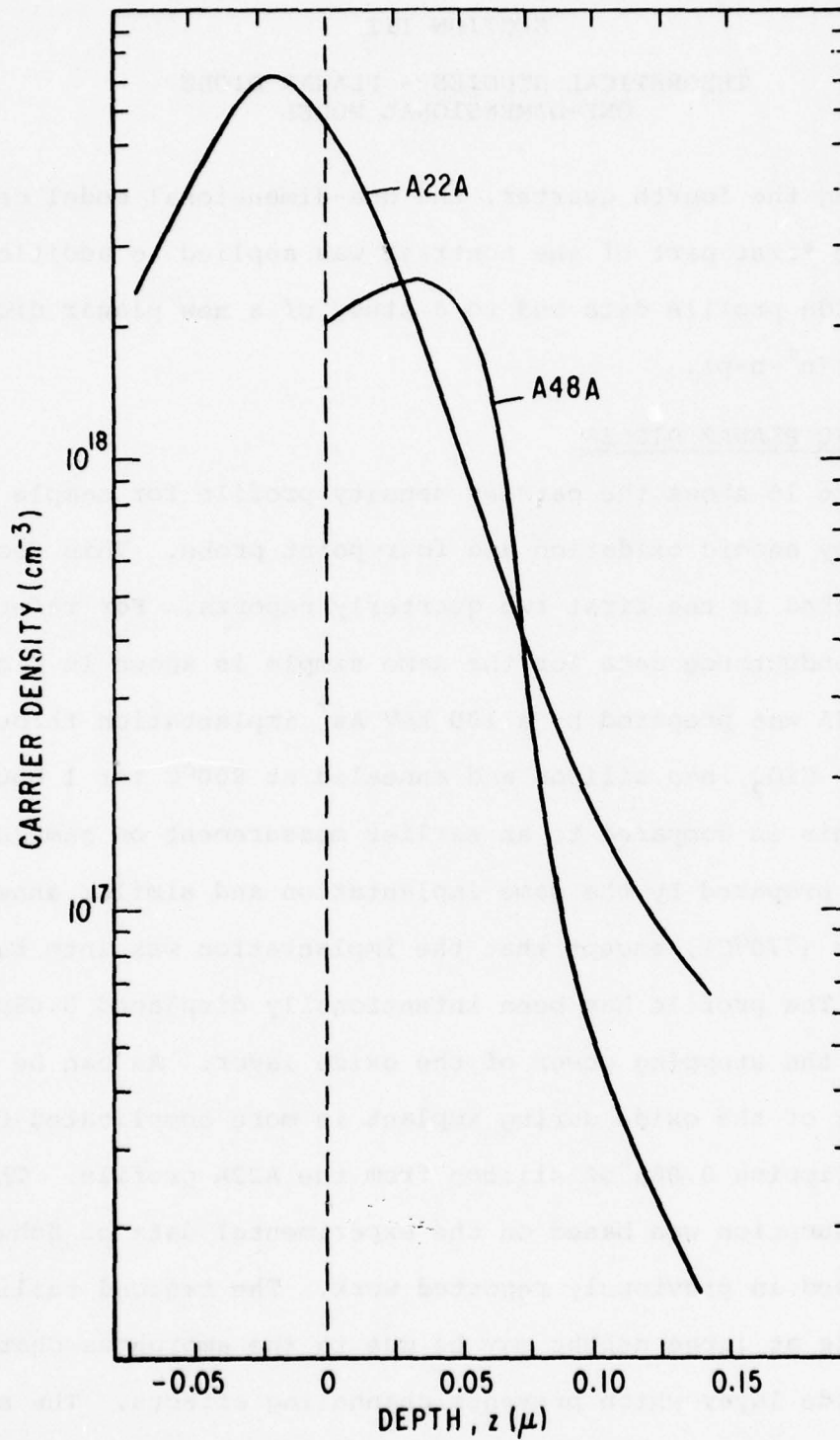


Figure 15. Carrier Density vs Depth for Samples A48A and A22A

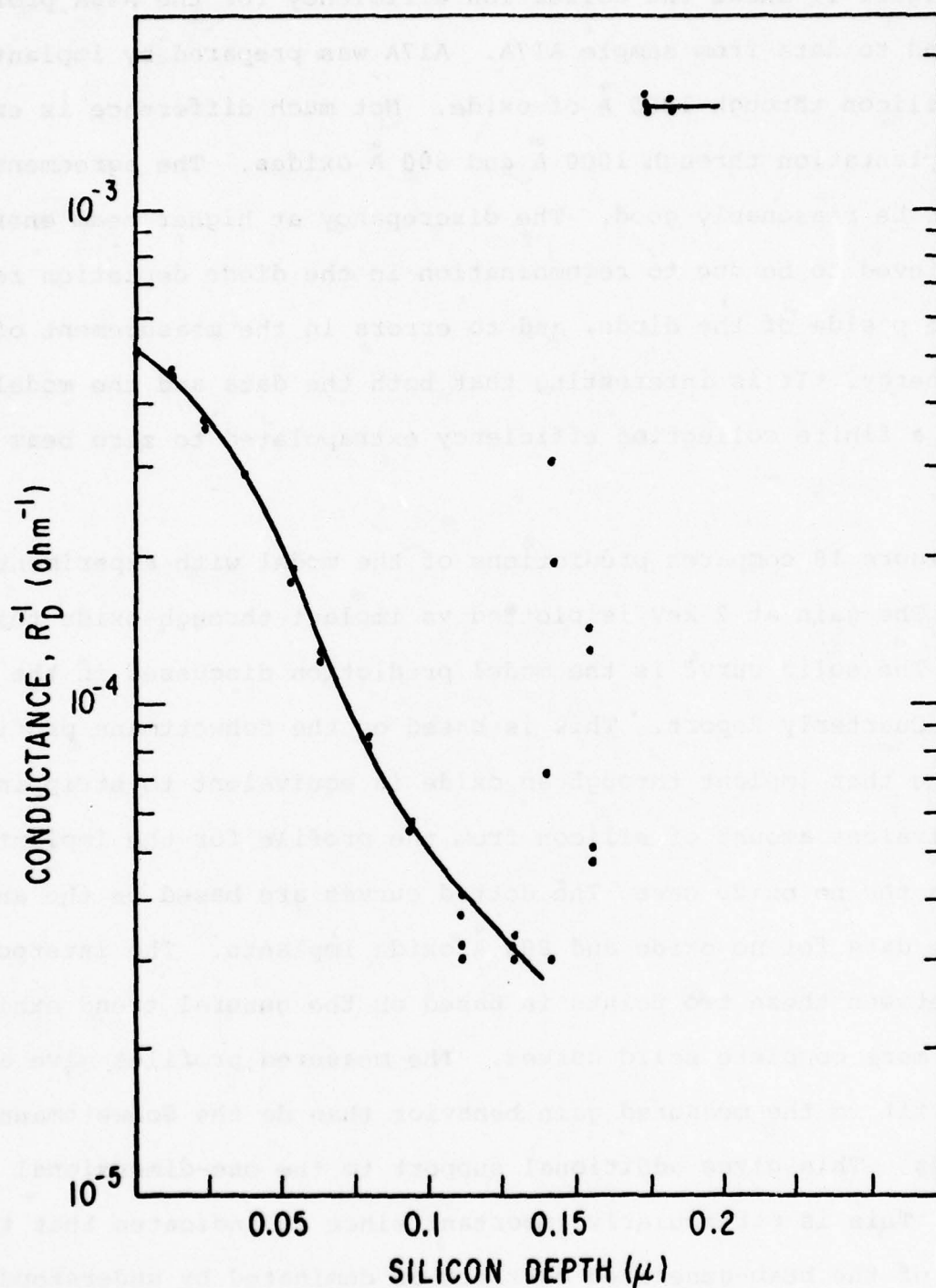


Figure 16. Measured Surface Conductance vs Silicon Thickness Removed for Sample A48A Fabricated by a 100 keV As^+ Implantation Through 800 Å of SiO_2

Figure 17 shows the collection efficiency for the A48A profile compared to data from sample A17A. A17A was prepared by implantation into silicon through 1000 Å of oxide. Not much difference is expected for implantation through 1000 Å and 800 Å oxides. The agreement is seen to be reasonably good. The discrepancy at higher beam energies is believed to be due to recombination in the diode depletion region and the p side of the diode, and to errors in the measurement of the beam energy. It is interesting that both the data and the model indicate a finite collection efficiency extrapolated to zero beam energy.

Figure 18 compares predictions of the model with experimental data. The gain at 2 keV is plotted vs implant-through-oxide thickness. The solid curve is the model prediction discussed in the Second Quarterly Report. This is based on the Schwettmann profile[4] assuming that implant through an oxide is equivalent to stripping an equivalent amount of silicon from the profile for the implant through the no oxide case. The dotted curves are based on the anodic profile data for no oxide and 800 Å oxide implants. The interpolation between these two points is based on the general trend exhibited by the more complete solid curves. The measured profiles give a better fit to the measured gain behavior than do the Schwettmann profiles. This gives additional support to the one-dimensional model. This is particularly important since it indicates that the motion of the beam-generated carriers is dominated by understood effects, i.e., carrier drift, diffusion in the presence of doping gradients, and surface recombination.

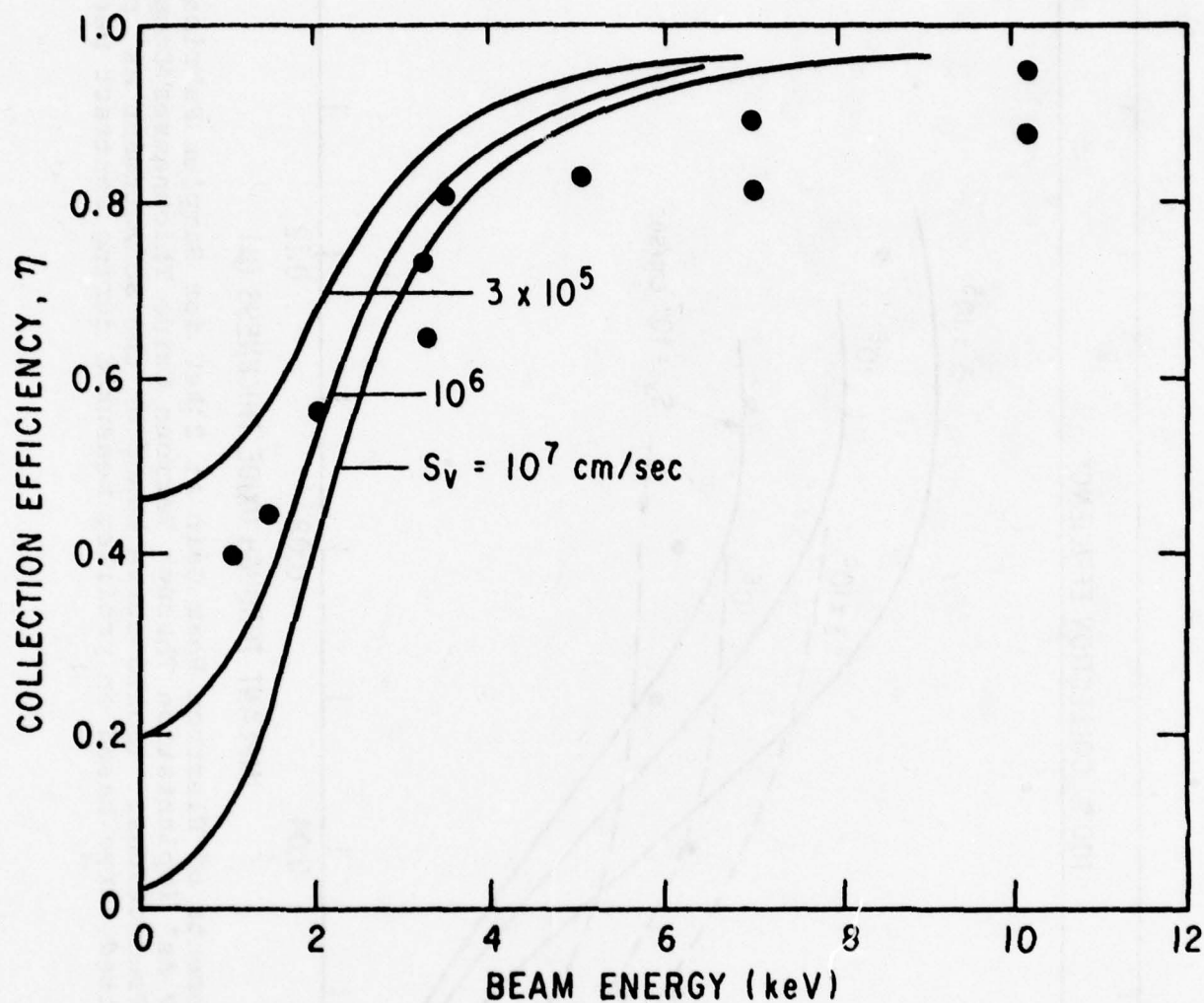


Figure 17. A Model Calculation of Collection Probability vs Beam Energy Based on the Doping Profile of Sample A48A (Figure 15). (Experimental points (●) from sample A17A fabricated by a 100 keV As^+ implantation through 1000 Å of SiO_2 .)

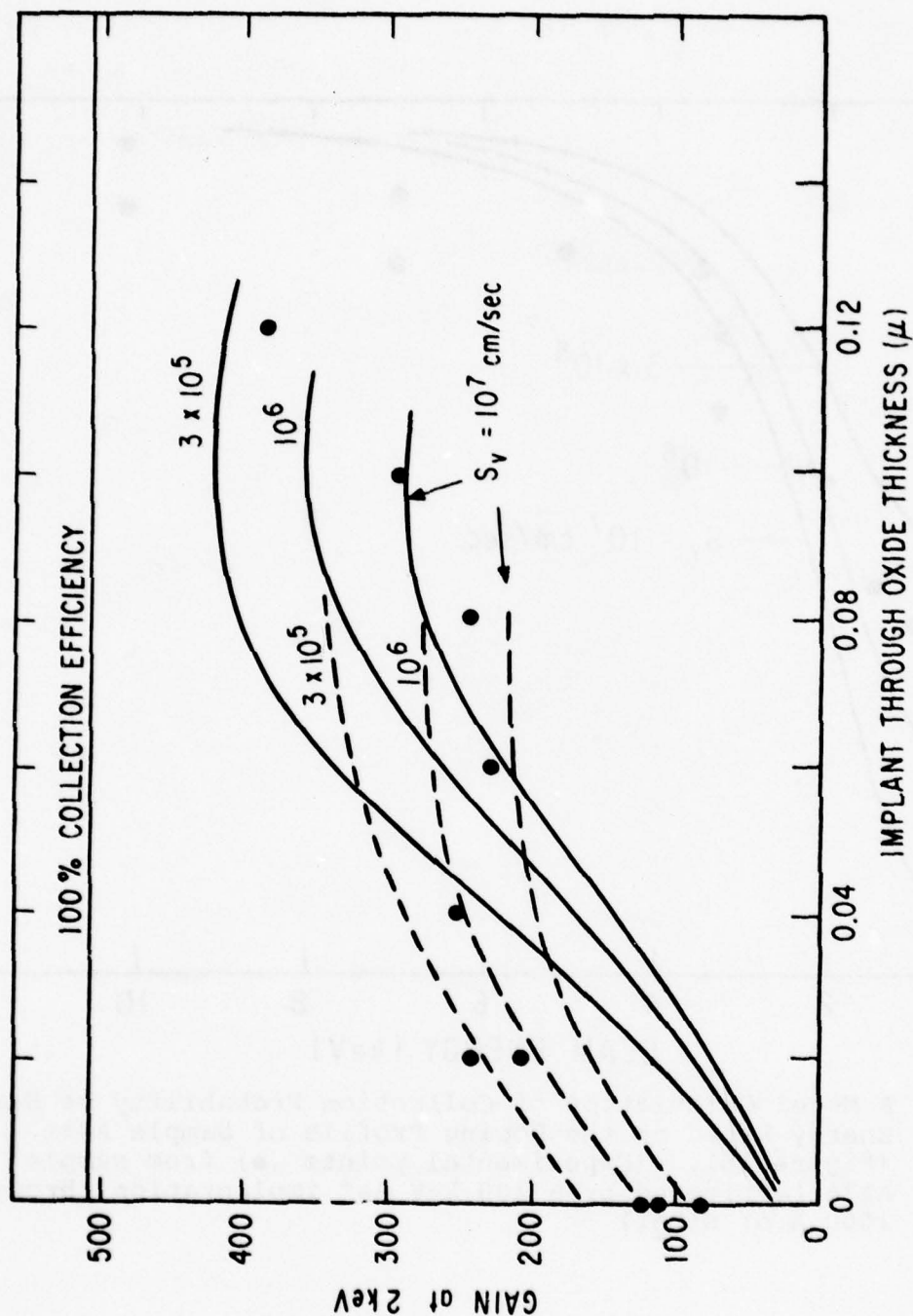


Figure 18. Measurements of Electron Beam Gain at 2 keV for Samples Fabricated by a 100 keV As^+ Implantation Through Various Oxide Thicknesses Compared to Model Predictions. (Solid curve based on the Schwettmann As^+ profile and dotted curve based on profiles measured during contract period.)

Figure 19 shows the collection probability from the model based on the doping profile from Figure 15 for sample A48A. Note that the collection probability is near 1 for depths greater than 0.05μ . Thus, when the minority carriers reach a depth $\gtrsim 0.05\mu$, they cannot return and sample the surface. The importance of this result is discussed further in Section II, "Bit Packing Density."

n^+-n-p As^+ DIODES

A new type of planar diode structure, the n^+-n-p , is discussed in this section. The type of doping profile contemplated is the solid curve shown in Figure 20. This profile consists of an As^+ implantation through 800 \AA of oxide such as sample A48A in Figure 15 superimposed on a uniformly doped np diode. For reference, the A48A type of n^+p doping profile is shown as the dotted curve. Such a profile can be achieved by implantation into a previously formed np diode. The curve labeled $\tau_p = \infty$ in Figure 21 shows the calculated collection probability for this profile for a surface recombination velocity $S_v = 10^7 \text{ cm/sec}$. On the scale of the figure, this is identical to the collection probability for the same profile without the n-region (the dotted profile in Figure 20). Similar agreement is obtained for other values of S_v . The n^+-n-p diodes should therefore behave almost exactly like the n^+p diode in the unwritten state.

Figure 22 shows the measured collection efficiency for such a diode [105-7(1)] compared to the model predictions assuming the profile in Figure 20. The preparation of this diode is discussed in more detail in Section IV, "Experimental Studies -- Planar Diode." The gain differences between these data and the data for a typical

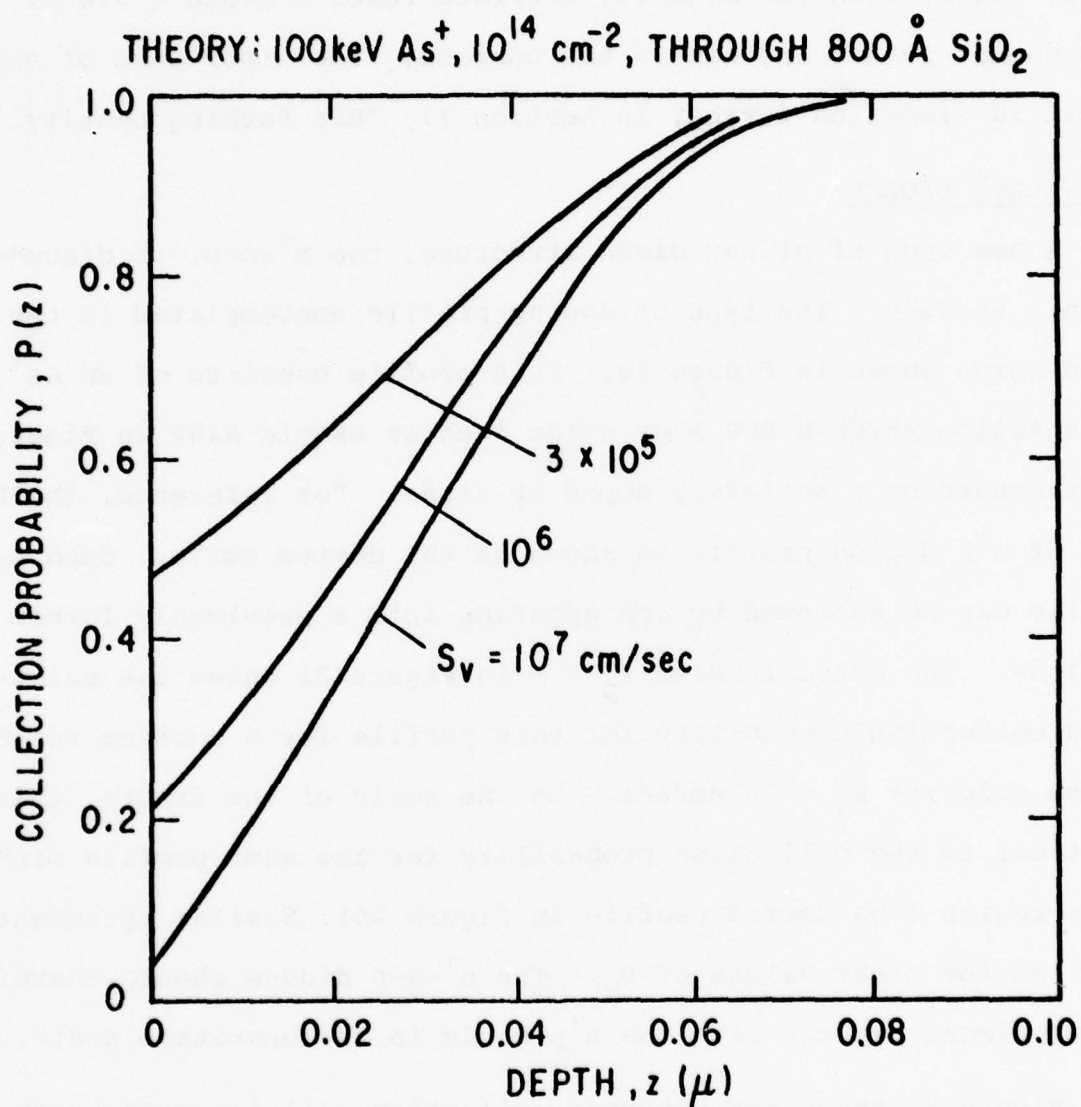


Figure 19. Model Calculation Based on the Profile of Figure 15 for Sample A48A for the Collection Probability $P(z)$ vs Depth

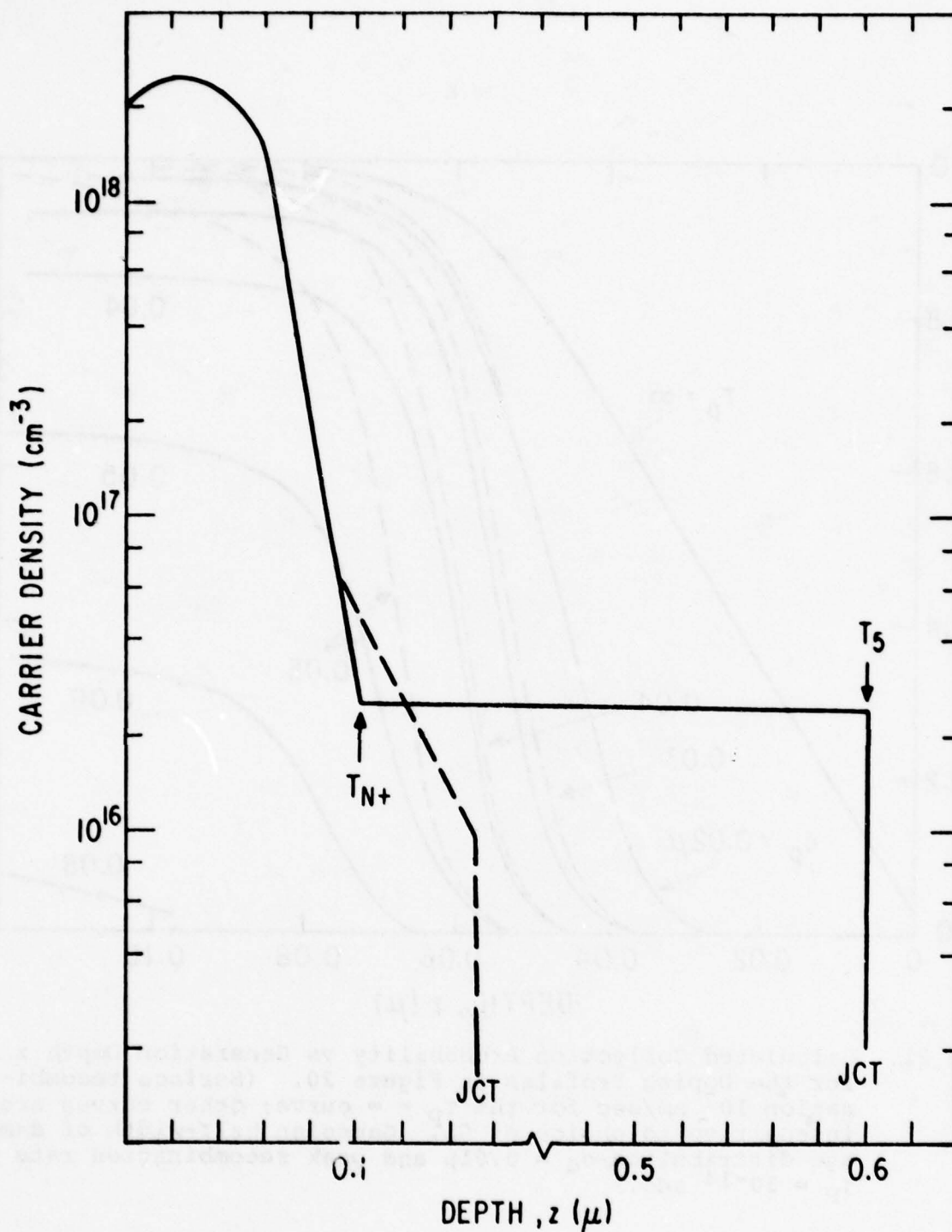


Figure 20. Doping Profiles for Typical Planar Diodes -- n⁺p (dotted) and n⁺-n-p(solid). (Dotted profile is based on Figure 15 and solid profile based on expected profile for samples of the type 105-7(1) described in Section IV.)

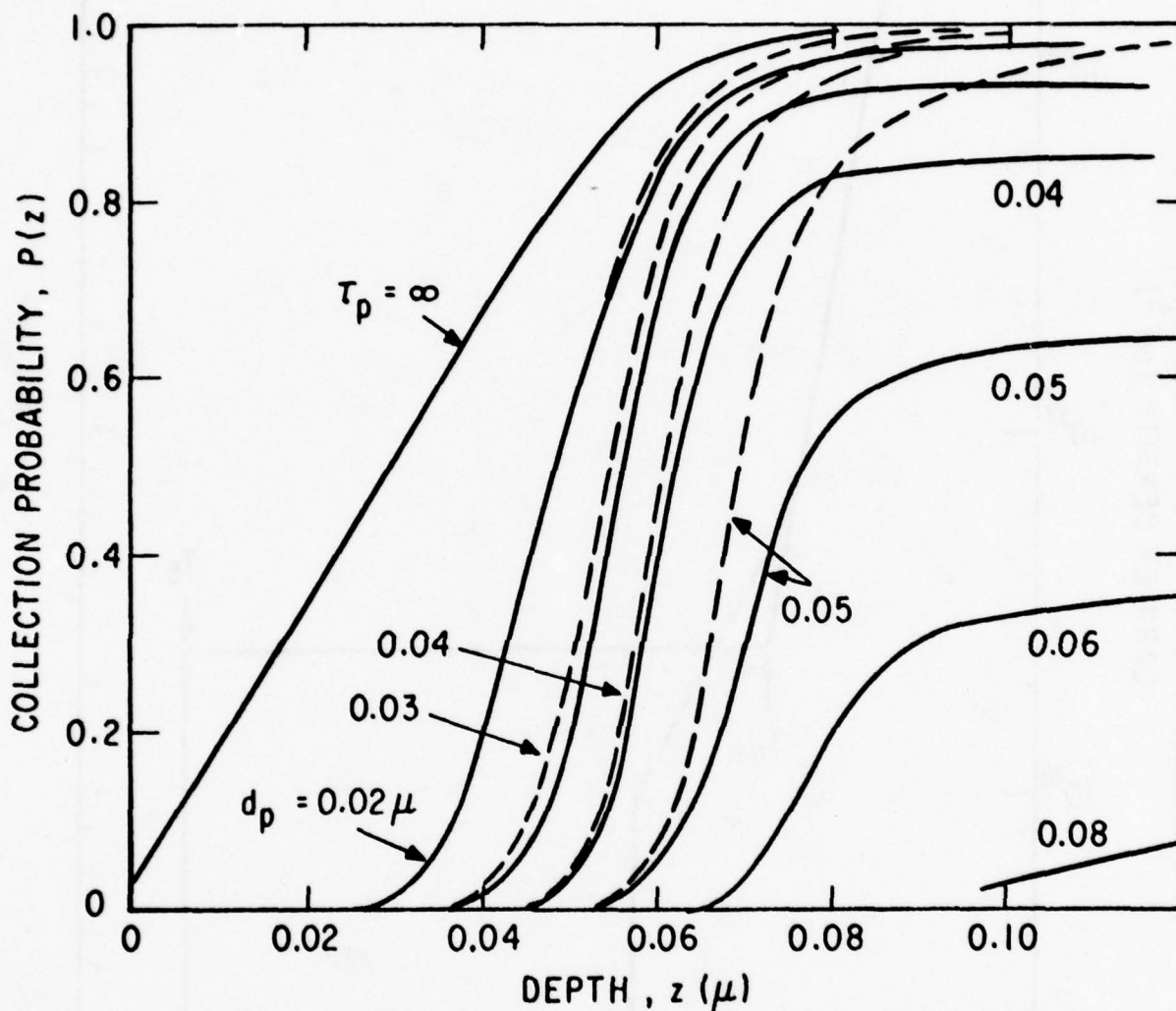


Figure 21. Calculated Collection Probability vs Generation Depth z for the Doping Profiles in Figure 20. (Surface recombination 10^7 cm/sec for the $\tau_p = \infty$ curve; other curves are insensitive to choice of S_v . Gaussian half-width of damage distribution $\sigma_d = 0.01\mu$ and peak recombination rate $\tau_p = 10^{-14}$ sec.)

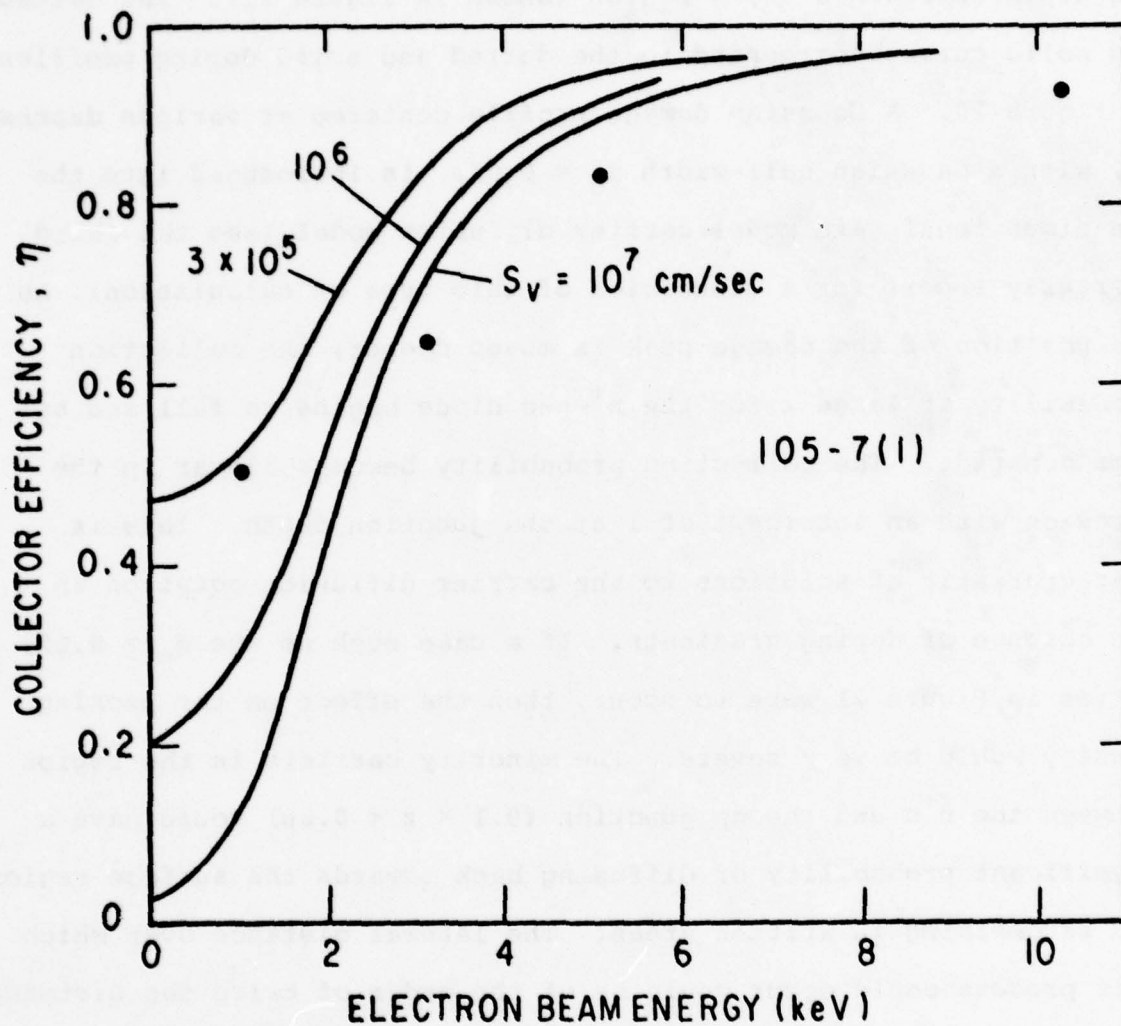


Figure 22. Measured Collection Efficiency for n^+ - n - p Planar Diode 105-7(1) Compared to Prediction of the One-Dimensional Gain Model Assuming the Solid Profile in Figure 20

n^+p diode of a similar type shown in Figure 17 are very small within experimental error and sample-to-sample variations.

In the written state, large differences can occur if the writing depth approaches the n-region (shown in Figure 21). The dotted and solid curves correspond to the dotted and solid doping profiles in Figure 20. A Gaussian damage profile centered at various depths, d_p , with a Gaussian half-width $\sigma_d = 0.01\mu$, is introduced into the one-dimensional gain model carrier diffusion model (see the Third Quarterly Report for a discussion of this type of calculation). As the position of the damage peak is moved deeper, the collection probability at large z for the n^+n -p diode begins to fall and become constant. The collection probability becomes linear in the n-region with an intercept of 1 at the junction depth. This is characteristic of solutions to the carrier diffusion equation in the absence of doping gradients. If a case such as the $d_p \geq 0.05\mu$ curves in Figure 21 were to occur, then the effect on the packing density would be very severe. The minority carriers in the region between the n^+n and the np junction ($0.1 < z < 0.6\mu$) would have a significant probability of diffusing back towards the surface region and recombining in written areas. The lateral distance over which this process could occur would be of the order of twice the distance between the n^+n and np junction or $\sim 1\mu$ in this case. Hence the readout would have very severe pattern sensitivity, i.e., a large number of written areas in the adjacent regions would significantly reduce the readout signal from the interrogated bit.

The general behavior of the written n^+n -p diodes can be expressed as follows: let R_D be the maximum depth of writing

($R_D \approx d_p + \sigma_d$ in the example of Figure 21) and T_{N+} be defined as in Figure 20. Then no differences will be observed in the readout behavior of the written planar diode if $R_D + \delta < T_{N+}$, where δ is a distance parameter which depends primarily on the slope of the doping profile in the region $z \gtrsim R_D$. For the specific example of Figures 20 and 21, $\delta \approx 0.05\mu$ and $T_{N+} = 0.1\mu$, so that the maximum useful writing depth $R_D \approx 0.05\mu$.

The one-dimensional gain model can be used to predict the maximum writing depth for the diodes of this type. In addition, the writing conditions can be determined experimentally. Figure 23a shows the calculated efficiency (gain normalized to number of generated carriers) for the n^+ -n-p planar diode described by Figure 20. Note the rapid degradation of the efficiency curve for peak damage depths of $\sim 0.05\mu$ which corresponds to a maximum writing depth of $\sim 0.06\mu$. This behavior is shown somewhat more explicitly in Figure 23b, where the efficiency at 10 keV is plotted vs peak damage depth. Note the rapid change in slope around 0.08μ . This corresponds to the region where the maximum writing depth R_D approaches the n^+ -n junction. At this point, the gain and resolution enhancing benefits of the doping profile are lost.

The preceding discussion leads to a simple criterion for recombination probability. If a region of high recombination (either a surface with high recombination or a region of high bulk recombination due to damage writing, for example) is separated from an excess minority carrier by a thickness of semiconductor z_0 which has a built-in electric field E , then the minority carrier will have a very small probability of recombining in the high recombination

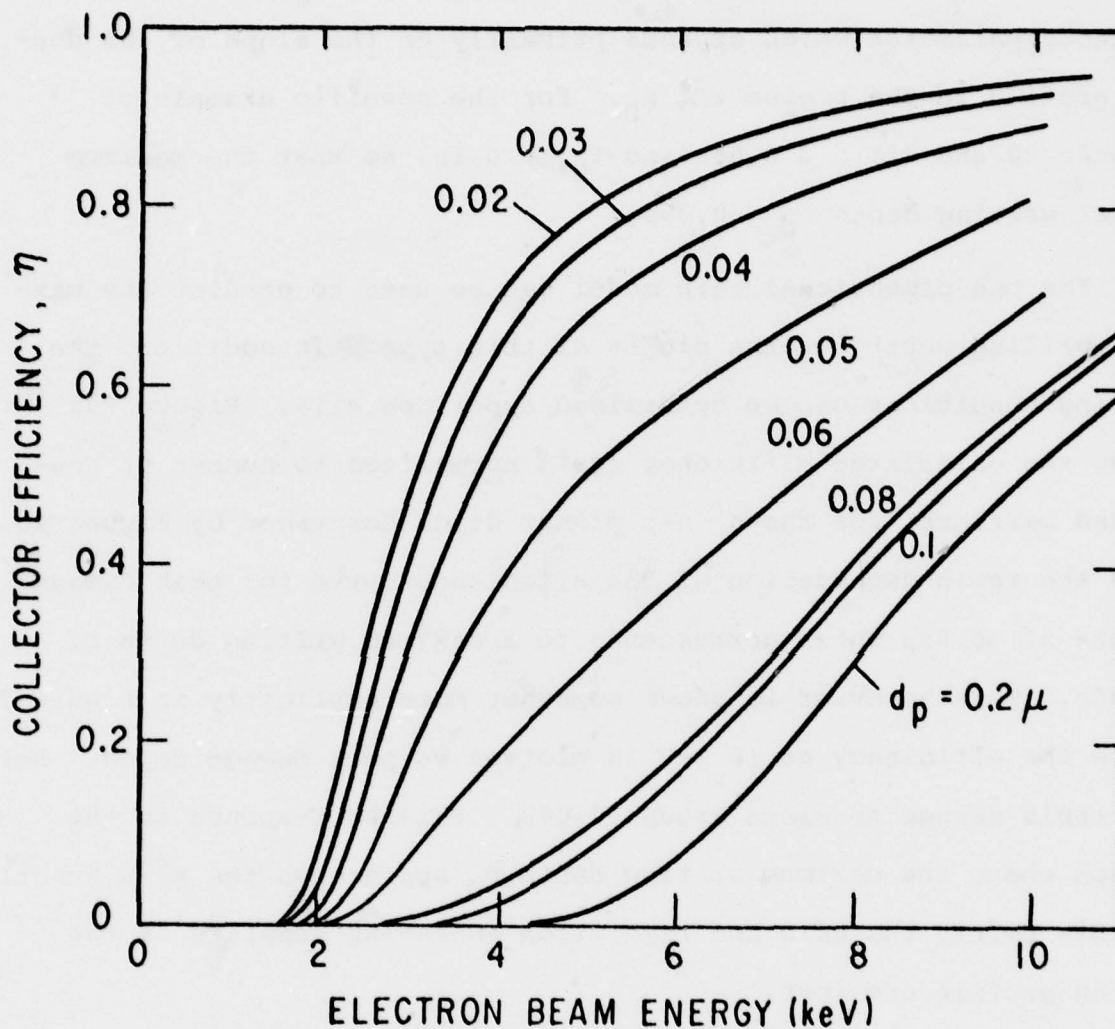


Figure 23a. Collection Efficiency vs Beam Energy Based on Collection Probability Curves of Figure 21 for a n^+-n-p Planar Diode. (Peak recombination $\tau_p = 10^{-14}$ sec and Gaussian half-width of damage $\sigma_p = 0.01\mu$. Damage peak depth d_p is the parameter which labels the curves.)

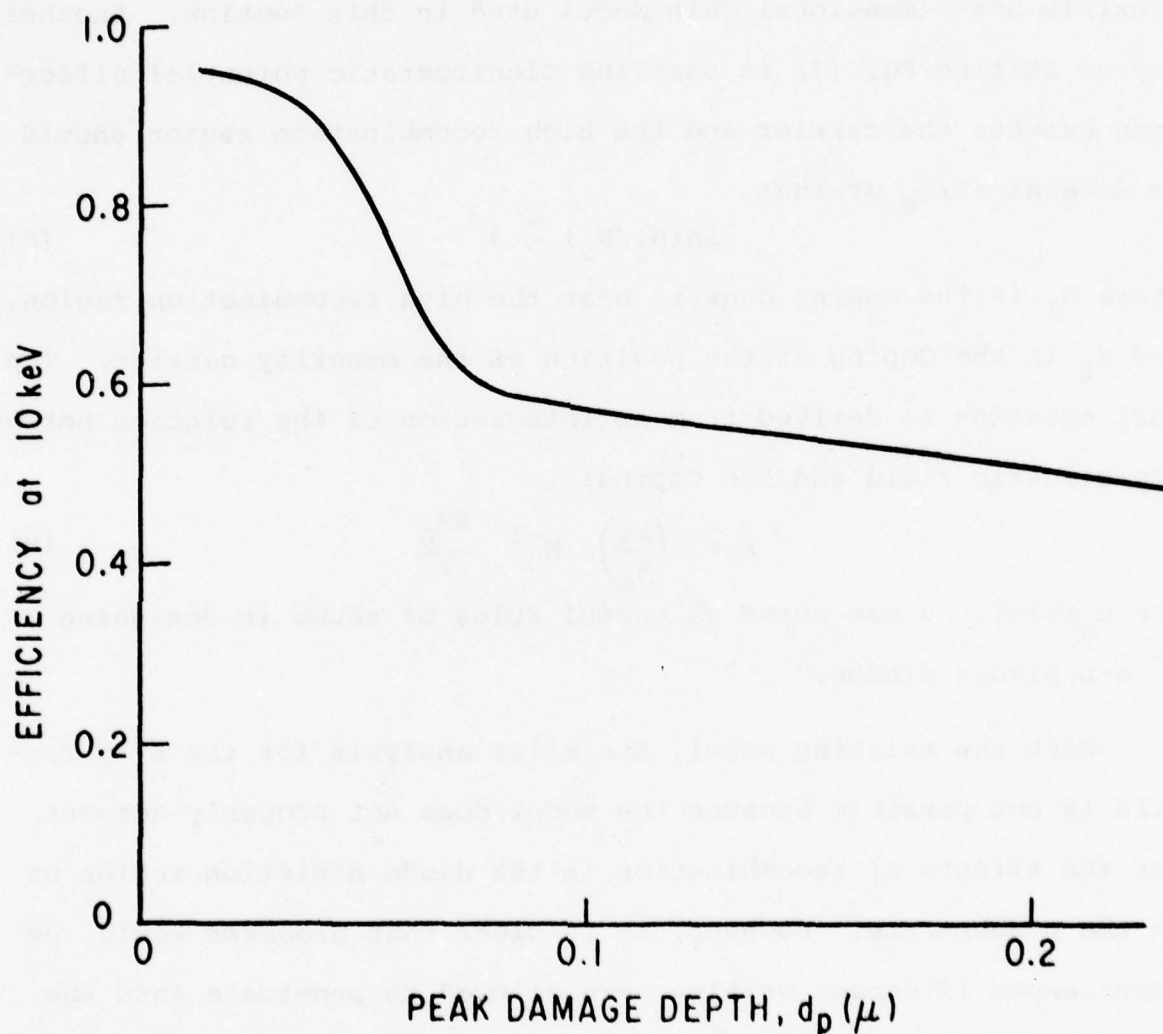


Figure 23b. Collection Efficiency at 10 keV from Figure 23a vs Peak Damage Depth d_p

region if

$$z_0(q_e/kT)E \gtrsim 3 \quad (7)$$

This relation can be derived from Eq. (25) of the First Quarterly Report or from a systematic evaluation of the behavior of the more flexible one-dimensional gain model used in this section. Another way of stating Eq. (7) is that the electrostatic potential difference between the carrier and the high recombination region should be several kT/q_e or that

$$\ln(N_1/N_2) \gtrsim 3 \quad (8)$$

where N_1 is the doping density near the high recombination region, and N_2 is the doping at the position of the minority carrier. The last equation is derived from an integration of the relation between the electric field and the doping:

$$E = -\left(\frac{kT}{q_e}\right) N_D^{-1} \frac{\partial N_D}{\partial z} \quad (9)$$

These relations can serve as useful rules of thumb in designing n^+ -n-p planar diodes.

With the existing model, a similar analysis for the n^+ -p profile is not possible because the model does not properly account for the effects of recombination in the diode depletion region or in the p-substrate. However, it is clear that problems would be experienced if damage writing were allowed to penetrate into the depletion region of either the n^+ -p or the n^+ -n-p diodes. Damage in either of these regions would cause increased diode leakage and reduced signal. Hence, in either case, the writing depth must be carefully controlled. One advantage of the n^+ -n-p diode is the clear signature that a plot such as Figure 23b gives for the determination of the maximum permissible writing depth.

The type of analysis described above may be applied to the writing experiments on the n^+ -n-p planar diodes during Phase II. Both n^+ and p, n^+ -n-p and p^+ -p-n diodes will be studied.

Considering their additional complexity, it is natural to ask why such double profile structures might be desirable. There are two presently identified reasons, both related to defect generation by ion implantation. The As^+ or other implantation used to form the n^+ -region generates a high defect density in the implanted region. The implantation is a high fluence implant, and the anneal temperature must be kept low to minimize spreading of the doping profile. For both reasons, the defect density in the depletion region of the diode can be high. One effect of these defects is to increase the leakage current and reduce the breakdown voltage of the diode. Since good quality diodes are necessary to optimize the signal to noise of the readout signal, this is undesirable.

The second reason relates to a possible problem with the diode boundary condition discussed at the end of the resolution studies section. This problem may again be related to defects in or near the diode depletion region. Hence, for both reasons, it would be desirable to separate the diode depletion region from the surface of the device. This is accomplished by the n^+ -n-p or the complementary p^+ -p-n structure. Because of the apparently beneficial effect on diode quality, these structures are likely to become the standard type of planar diode. They will be the subject of study during the first part of Phase II.

SECTION IV

EXPERIMENTAL STUDIES - PLANAR DIODE

During the fourth quarter, work continued on the refinement of the planar diode substrate structure for the determination of optimum writing parameters.

GERMANIUM PLANAR DIODES

Germanium diodes have been investigated as potential substrates for the alloy junction writing device. These studies were motivated by the low thermal diffusivity of germanium (1/3 that of silicon), which would make it more desirable from a heat transfer point of view, since the heat flow from the writing region would be reduced. Recent modeling studies, however, have indicated that the thermal conductance of the top metal film is more important than the substrate properties in determining heat flow.

In an attempt to produce a germanium structure such as that already developed in silicon, a number of experiments were performed. The germanium structure should:

- Have a very thin highly doped top layer
- Preferably be n^+ on p for the alloy junction device
- Have high gain at low electron beam reading voltages.

However, the lack of a highly developed planar technology, such as that for silicon, makes this material considerably more difficult to work with for device purposes.

Polished wafers of p-type $\langle 100 \rangle$ Ga-doped 1-3 ohm-cm germanium were implanted with arsenic and phosphorus to produce an n^+p planar collection diode substrate for writing as indicated in Table 2.

TABLE 2

GERMANIUM SAMPLES FOR PLANAR DIODE (n^+p) STUDIES

Sample	Ion	Energy (keV)	Fluence (ions/cm ²)
Ge-1	P ⁺	50	10 ¹³
Ge-2	P ⁺	50	10 ¹³
Ge-3	P ⁺	195	10 ¹³
Ge-4	P ⁺	195	10 ¹³
Ge-5	As ⁺	50	10 ¹³
Ge-6	As ⁺	50	10 ¹³
Ge-7	As ⁺	150	10 ¹³
Ge-8	As ⁺	150	10 ¹³

Note: The starting material was 1-3 ohm-cm p-type Ga-doped <100> germanium.

Samples Ge-1, Ge-3, Ge-5, and Ge-7 were then annealed 1 hour in an argon ambient at 500°C to remove radiation damage and activate the implanted dopants. Similarly, samples Ge-2, Ge-4, Ge-6 and Ge-8 were annealed 1 hour in an argon ambient at 700°C. Mesa structures were then etched and the diodes tested. The results were unsatisfactory. The backs of wafers Ge-1 and Ge-2 were sputtered with 500 Å of nickel to help getter possible heavy metal impurities that might result in an undesired conversion of the material to p-type. These structures were then annealed for 1 hour in an argon ambient, Ge-1 at 600°C, and Ge-2 at 700°C. The results were still very poor. Identical unimplanted germanium was annealed in the set of furnace tubes, totally dedicated to the germanium work. No indication of possible furnace contamination was evident. A better test would involve n-type wafers to see if they convert to p-type during bake.

Another group of wafers was prepared, again using arsenic and phosphorus as the implanted dopants, into 1-3 ohm-cm p-type <100> germanium. A number of different parameter variations were used, such as ion fluence, thickness of oxides for through-oxide implants, resist masking to protect target edges during implantation, gettering metals on the back, and anneal temperatures. These data are summarized in Table 3. The desired diode quality or gain characteristics were not apparent.

TABLE 3

GERMANIUM SAMPLES FOR PLANAR DIODE (n^+p) STUDIES

Sample	Surface	Ion	Energy (keV)	Fluence (ions/cm ²)
Ge-10	-	As ⁺	100	10 ¹³
Ge-11	800 Å SiO ₂	As ⁺	100	10 ¹³
Ge-12	resist mask	As ⁺	100	10 ¹³
Ge-13	-	As ⁺	100	10 ¹⁵
Ge-14	-	As ⁺	100	10 ¹⁵
Ge-15	-	As ⁺	100	10 ¹⁵
Ge-16	-	As ⁺	100	10 ¹⁴
Ge-17	800 Å SiO ₂	P ⁺	100	10 ¹⁴
Ge-18	resist mask	As ⁺	100	10 ¹⁴
Ge-19	200 Å SiO ₂	P ⁺	100	10 ¹⁴
Ge-20	1400 Å SiO ₂	P ⁺	100	10 ¹⁴
Ge-21	-	P ⁺	100	10 ¹⁴
Ge-22	-	As ⁺	100	10 ¹³
Ge-23	800 Å SiO ₂	As ⁺	100	10 ¹⁴

Note: Starting material was 1-3 ohm-cm p-type <100> germanium.

Ge-16, Ge-17, Ge-18, and Ge-23 were also sputter-coated on the back with 1000 Å of indium and then getter annealed for 4 hours in Linde nitrogen. However, this did not improve their character. Gettering with 2500 Å of nickel sputtered on the back of Ge-21, with a subsequent 1 hour anneal at 500°C, produced similar results. Thermal conversion was also attempted in which a higher temperature anneal is followed by a lower temperature anneal. This was intended to tie up heavy metals such as copper, which could cause undesirable p-type conversion, in precipitate form. The attempt was, however, also unsuccessful.

Another set of experiments, aimed at producing germanium planar collection devices, was carried out using a different set of starting material. These wafers were p-type <111> 1.8-2.5 ohm-cm germanium. Samples Ge-24, Ge-25, Ge-26, Ge-27, and Ge-28 were implanted with 100 keV As⁺ to a fluence of 10¹⁴ ions/cm². Again the results were unsatisfactory.

The lack of success in producing usable n⁺p planar collection diodes on germanium substrates may be attributed to a number of factors. Producing the n-type conversion is difficult since the material tends to become p-type in the presence of contamination, metallic impurities, surface damage, or radiation damage. Contamination problems alone could account for the poor quality. Predominantly, however, it is probably a problem of radiation damage. To produce the very thin n⁺-layer analogous to that produced in silicon for beam writing and reading purposes, ion implantation is the desired technique. Diffusions produce surface damage and penetrate too deeply for the high gain at low electron

beam voltages required for high bit densities. Thick n-type layers were produced on p-type germanium wafers by antimony and bismuth diffusions. The phosphorus diffusions into p-type germanium produced negative results. Implantation, however, produces more radiation induced defects (which are inherently p-type in germanium) than can be compensated by the doping impurity being introduced by the implantation process. Even annealing does not necessarily remove sufficient p-type damage centers to allow the phosphorus or arsenic electrical activity to predominate and produce an n-type layer. The resulting layer is less p-type than the substrate, but sufficient conversion is not present to form the high quality diode desired.

Another set of experiments was designed which was intended to allow the tendency toward p-type behavior in damaged layers to be an asset to the process. Samples of 1 ohm-cm n-type <111> germanium, Ge-30, Ge-31, Ge-32, Ge-33, and Ge-34, were implanted with 50 keV B⁺ to fluences of 10¹⁴ ions/cm² to produce p⁺ layers on n substrates. After a 1 hour anneal in N₂ at 600°C, structures were formed which measured p-type on n-type. Since other doping alloy junction systems such as antimony in another carrier metal might allow the formation of n-type eutectic alloyed regions rather than p-type, this polarity structure does not preclude its use for alloy junction writing.

SILICON DIODES

The fourth quarter planar diode work continued to center on the refinement of the silicon planar collection diode structure

to optimize the gain at low reading electron beam voltages and improve the diode characteristics. Both n^+p and p^+n devices were processed and studied, and variations of parameters for each were pursued.

The standard starting material for the n^+p structure is 10-20 ohm-cm $\langle 111 \rangle$ silicon. An 800 Å SiO_2 layer was formed on the surface, and 100 keV arsenic was implanted through this oxide at a fluence of 10^{14} ions/cm² at room temperature, 7° off the $\langle 111 \rangle$ crystalline axis. After implant, the wafers were annealed at 900°C for 1 hour in an argon ambient. The oxide was then stripped and the targets scribed and prepared for writing experiments.

Variation of the As^+ fluence for formation of the n^+ -layer is of interest in selecting the optimum doping profile for the writing process. Towards this end, the targets listed below were prepared to examine comparatively the effect of background doping on the writing mechanism.

<u>10^{12} ions/cm²</u>	<u>10^{13} ions/cm²</u>	<u>10^{15} ions/cm²</u>
A89	A87	A86
A90	A88	A91

In another experiment, the possibility of using an n^+-n-p structure was investigated. Experimental planar diode target numbers 105-7, 105-10 and 104-12, which had been prepared for another purpose, were used. These planar diodes had p^+ channel stoppers and diffused n^+ contacts. The diode area had been implanted with 80 keV phosphorous at 10^{12} ions/cm² through 1000 Å

of thermal SiO_2 . This implanted phosphorous was diffused to a depth of $\sim 1\mu$ by the growth of a 2800 Å dry thermal oxide for 4 hours at 1100°C. This oxide was then stripped and an 800 Å SiO_2 film was sputter deposited. Then the diode was implanted a second time with 100 keV arsenic to a fluence of 2×10^{14} ions/ cm^2 . The targets were annealed at 900°C for 1 hour in argon and the SiO_2 film stripped. This should result in the doping profile indicated in Figure 20. Such a structure was expected to provide a high quality diode characteristic while simultaneously providing a high collection velocity of carriers at the junction, since any defects associated with the second As^+ implant would be well separated from the junction. This was the case, as indicated by Figure 22, for sample 105-7(1). Since this double implant technique resulted in exceptionally high quality planar diodes, further production of this n^+p structure as well as p^+n devices is anticipated for the next quarter.

In addition to this work, the first complete processed lot of archival targets for the Archival Memory Program was produced at General Electric's Integrated Circuit Center in Syracuse. The processing steps for this lot are enumerated in Table 4. A diagram indicating a cross section for this device is shown in Figure 24. which follows. This first batch of targets did not prove totally satisfactory for high resolution ion writing.

Another set of experiments pursued with the n^+p structures, during the fourth quarter, involved removing layers of precise thickness from the top surface of the planar diode. This was done to (1) remove a "dead" or damaged layer which might reduce the gain of the structure at low electron beam reading voltages and

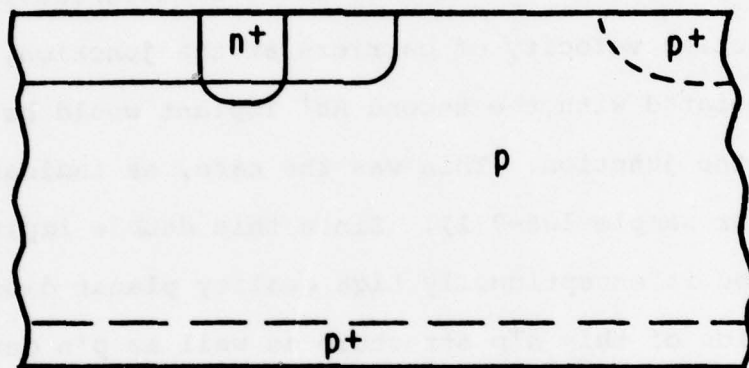


Figure 24. Cross Section of a Planar Diode Substrate Processed in Lot AR-1

TABLE 4

PROCESSING STEPS FOR THE AR-1 LOT OF ARCHIVAL TARGETS

Starting material, 400 ohm-cm <111> Monex silicon

1. Branson clean
2. Oxidize 6000 Å SiO₂ at 1050°C
3. Photomask with p⁺ Mask #1B; double mask and expose
4. Spin, prebake, and expose resist on backside
5. Postcure resist 30 min at 140°C
6. Etch oxide in buffered HF
7. Strip clean of resist using H₂SO₄ + 50/50 H₂SO₄/H₂O₂; rinse
8. Branson clean
9. Boron predep 1 hour at 1025°C, in N₂, with BN
10. Strip glass with 50/50 HF/H₂O for 30 sec; Nitric boil for 10 min; then Branson clean
11. Oxidize 15 min in dry O₂, plus 45 min at 1100°C, steam (oxidized hydrogen) for 4500 Å
12. Photomask with n⁺ Mask #2B, double mask and expose
13. Etch oxide with buffered HF (82424) and remove oxide from backside
14. Strip resist with H₂SO₄ + 50/50 H₂SO₄ and rinse
15. Branson clean
16. Phosphorus predep at 860°C, 10 min N₂/O₂, 10 min POCl₃ + N₂O₂, 5 min O₂
17. Oxidize 4000 Å SiO₂ at 970°C, 2 hours in steam
18. Photomask with diode Mask #3B, double mask and expose
19. Etch oxide with buffered HF etchant 82424
20. Strip resist with H₂SO₄ + 50/50 H₂SO₄/H₂O₂ for 5 min; rinse; dry

TABLE 4 (Cont'd)

21. Branson clean
22. Oxidize 1000 Å SiO₂ 17 min in dry O₂ at 1150°C
23. Ion implant 100 keV singly ionized arsenic to fluence of 2×10^{14} ions/cm²
24. Dip etch wafers with etchant 82424 for 1 min (to remove approximately 500 Å oxide)
25. Anneal 1 hour at 900°C in argon ambient
26. Etch oxide approximately 1 min in buffered HF etchant 82424 until clean in implanted area
27. Branson clean
28. Electron beam deposit 1000 Å chromium on front
29. Electron beam deposit 2000 Å aluminum on backside
30. Photomask with Mask #6B, double mask and expose
31. Spin resist on backside at 3500 RPM for 20 sec; pre-bake 15 min at 120°C; expose backside
32. Postcure resist 30 min at 140°C
33. Etch chromium at 35°C for 45 to 60 sec with chromium etchant
34. Strip resist with Micro Strip A-20

(2) to cut off the profile of the implanted ions at a point such that the slope of the dopant profile dropped off sharply immediately from the surface rather than being relatively flat, as indicated by anodic oxidation profile measurements, before going into the steep gradient region. This concept is illustrated in Figure 23b.

Four techniques were used for this surface removal: polysilicon etch, hot KOH, hot HNO_3 , and anodic oxidation.

The polysilicon etch (100 HNO_3 , 40 acetic, 2HF), though very effective for layer removal, was difficult to control. Very good results were obtained for some samples. However, the etchant acted so quickly (2300 Å/min) that it tended to etch through the junction in a few seconds, particularly if the etch was fresh. The goal was to remove only 500 Å. Four point probe measurements after etch were compared to the measured doping profile to determine the thickness removed. Pitting and staining were also problems with this etch. Very thorough cleaning, such as boiling in three solvents (trichloroethylene, acetone, and ethyl), resulted in less staining. Gain measurements indicated good uniformity for unstained samples.

Samples such as A48B, which had been implanted with 10^{14} ions/cm² of 100 keV arsenic and annealed 1 hour at 900°C in argon, displayed collection efficiencies, η , on the order of 0.47 at 2 keV following a 3 second etch. Selected optimum targets of this type were used for the high resolution writing studies. Because of subsequent problems with the electron beam lithography and ion writing the storage density of these targets has not been evaluated.

Hot (55°C) KOH-isopropyl alcohol was also employed for layer removal on these targets, again with mixed results. However, considerable variation in the amount of material removed was observed for the same etch time. This lack of controllability is seen in the data shown in Table 5, where the wide variation in etch rate is indicated.

TABLE 5

SILICON MATERIAL REMOVED AS A RESULT OF TIMED ETCHES

<u>Sample</u>	<u>Time (sec)</u>	<u>Si Removed (Å)</u>
Al00D	30	175
	30	250
Al00C	60	250
Al00B	120	1250
Al02A	60	>1500

Another method of layer removal, a hot (77°C) nitric acid boil, was used in an attempt to etch off a precise amount of the silicon substrate material by forming a layer of oxide on the surface. The layer could then be removed by etching with BHF. This is a fairly lengthy procedure for the removal of any substantial thickness of material, since the reaction in which the oxide is formed at the surface exhibited a saturation point at which typically 8 Å of silicon were consumed and 20 Å of SiO₂ formed. Therefore layer removal was a step and repeat operation: hot nitric acid, BHF, and then repeat. Although tedious, considerably more control was a feature of this technique and with it, efficiencies at 2 keV on the order of 0.5 demonstrated with sample Al01B.

Anodic oxidation of the silicon was also undertaken for layer removal and thinning of the top layer. Sample Al04D was stripped of 350 Å of silicon by anodic oxidation and awaits SEM (scanning electron microscope) examination.

SECTION V

ION WRITING EXPERIMENTS

Two types of silicon substrates were used for the high resolution writing experiments during this quarter: samples whose identification numbers are prefixed by the letter "A", indicating an n^+p planar diode structure formed by a 100 keV As^+ implantation through 800 Å SiO_2 , and those prefixed with the letter "B", indicating a p^+n device, formed by a 50 keV B^+ implantation through 2600 Å SiO_2 , both annealed 1 hour in argon at 900°C. Some of these samples had the thinned top layers described in Section IV.

Since a finely focused 0.1 μ ion writing beam was not yet available during this experimentation period, electron beam lithography was used to prepare high resolution patterns to aperture a flood ion beam at the surface. This simulated small area implantations and provided a means for testing of device feasibility for very small size bit sites.

The first step in preparing the substrates for writing experiments was a thorough cleaning procedure. Completed planar diode structures were cleaned in a three step boiling solvent sequence, trichloroethylene, ethyl alcohol, and acetone, followed by a distilled water rinse. This cleaning promoted better adhesion of the masking material.

Masks were formed in two ways: using a thick patterned resist or using chrome patterned by means of a resist. Most samples were masked with chrome for implantation. For this technique, layers of 500 or 1000 Å of chrome were sputtered on the cleaned planar

substrate. Then a positive resist layer of polymethyl methacrylate was spun on at 2000 rpm for 1 minute (from a 5% solution of elvacite 2051 in toluene). This resulted in a resist layer thickness of 0.1 μ . A gel permeation chromatograph of the material (Figure 25) indicates that the average molecular weight for this material is 760,000, with very few molecules lighter than 20,000. Following a 15 minute prebake at 170°C to drive off the solvent, the targets were ready for the writing of patterns with the scanning electron microscope-video pattern generator.

A schematic for the system used with the Coates and Welter field emission scanning electron microscope to expose patterns in the polymethyl methacrylate (PMM) is shown in Figure 26. A closed circuit television camera was focused on a back-illuminated glass panel on which the desired pattern had been photographically reproduced. The resulting video signal was fed through a comparator to the microscope beam blanking unit and the pattern was exposed in the resist. Typical patterns are shown in Figure 27. The patterns were designed to explore the limits of resolution and other characteristics of the target. The lithography patterns included such features as checkerboards, isolated written areas, isolated unwritten areas, and bars of various sizes. Because of electron back scattering, very small scale patterns, such as checkerboards, are difficult to produce.

The energy of the exposing electron beam was normally 16 keV. Spot sizes $< 0.01 \mu$ were achieved at 16 keV. Exposures range from 10^{-5} to 5×10^{-4} coulombs/cm².

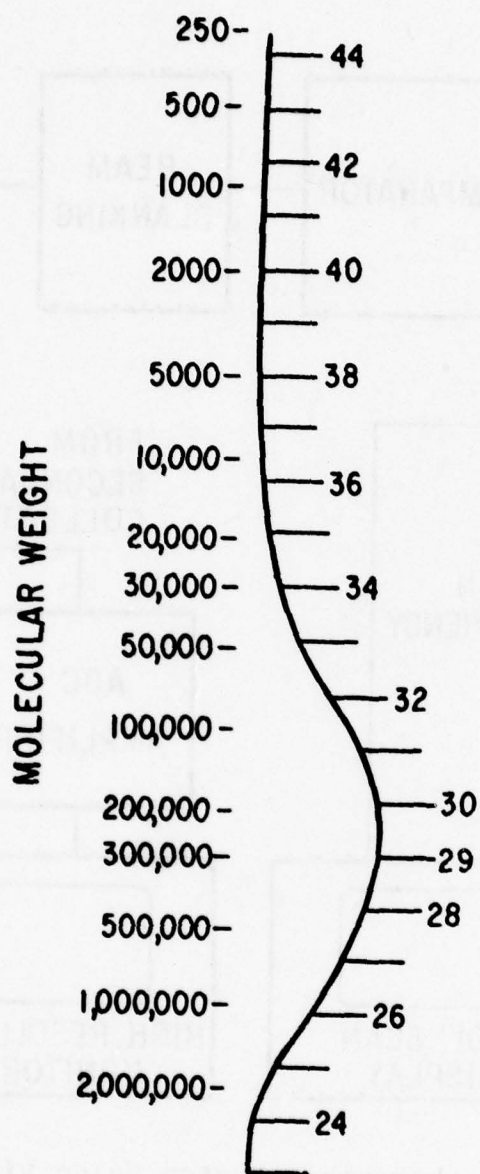


Figure 25. Gel Permeation Chromatograph of du Pont Elvacite 2041

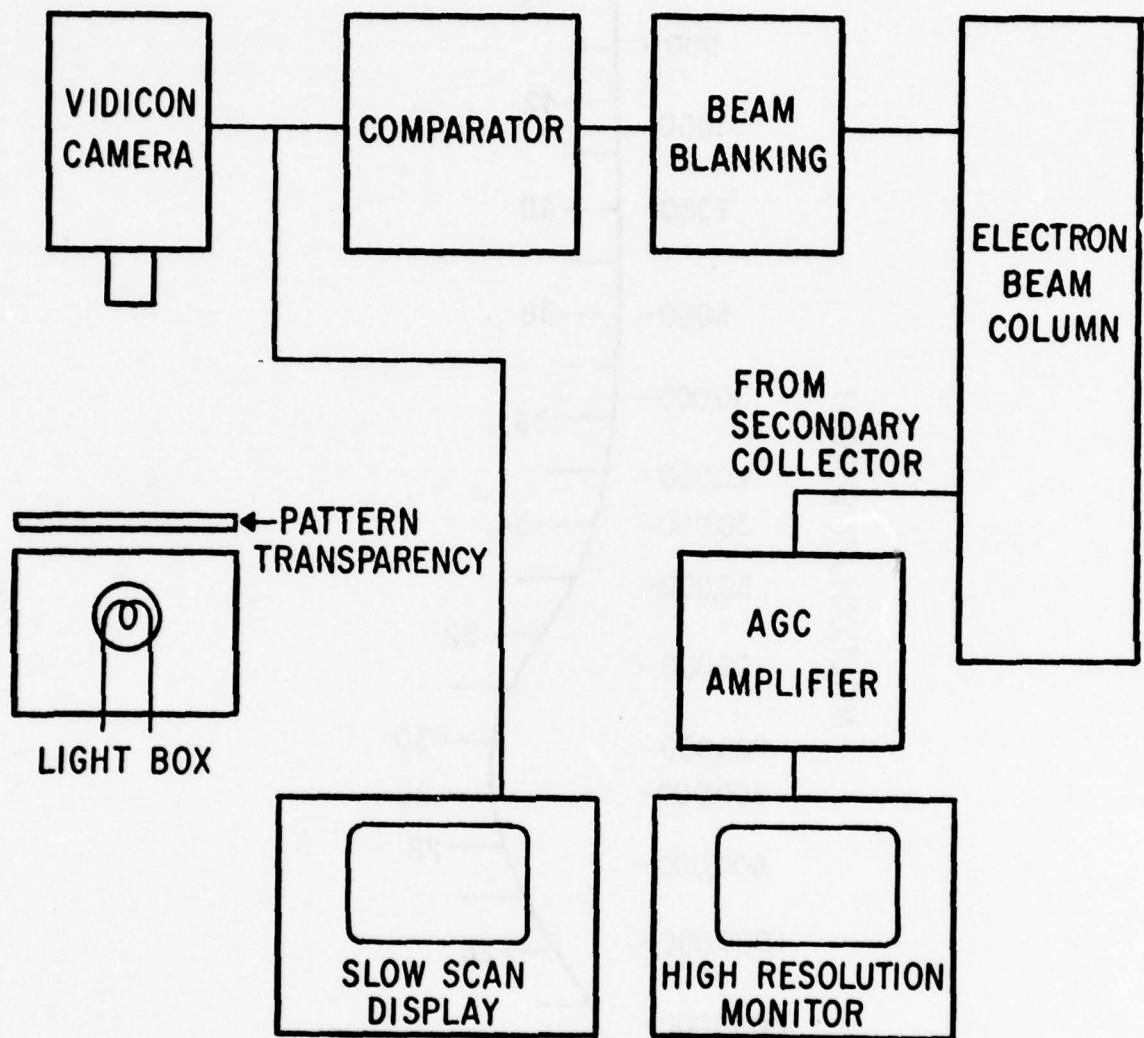


Figure 26. Electron Lithographic System Using Video Input to Scanning Electron Microscope

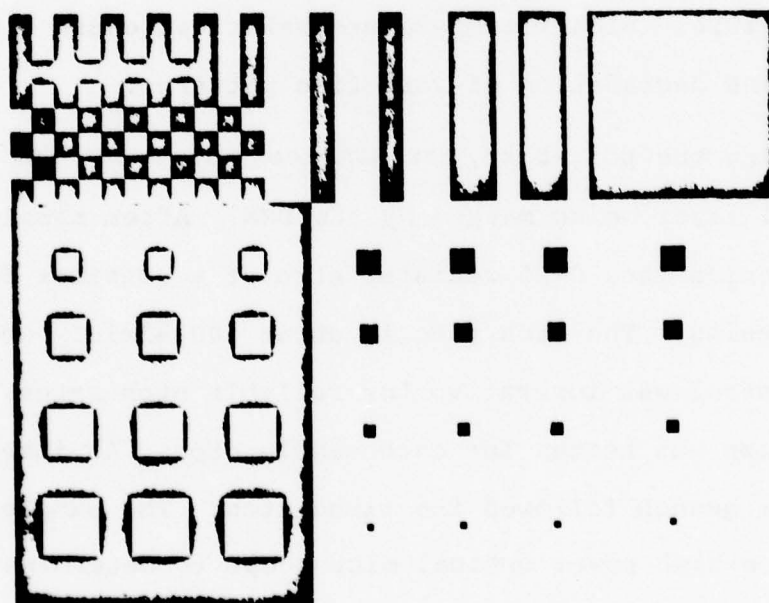
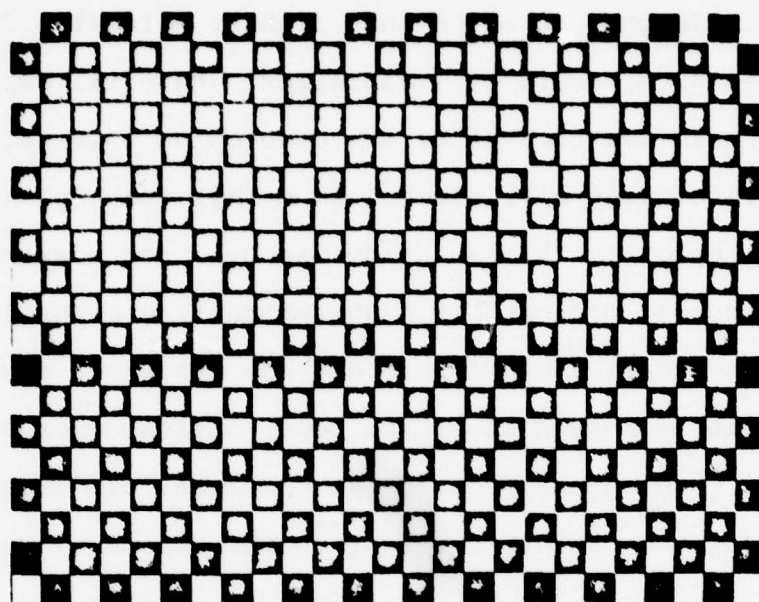


Figure 27. Resolution Patterns Used with Video Input to Scanning Electron Microscope

Developing of the exposed resist followed. PMM is a positive resist which undergoes scission into lighter molecules faster than polymerization as a result of irradiation. Material exposed to the electron beam was removed by the developing solvent. A three-to-one mixture of isopropyl alcohol to methyl isobutyl ketone was used for development. This solution was used for soaking the sample for 60 seconds, followed by a 30 second fine aerosol spray. The sample was then allowed to air dry, or was blown dry with nitrogen, and then examined in a high power optical microscope to make sure the development process was complete. In order to improve the adhesion of the patterned resist to the chrome, a post-bake at 120°C for 15 minutes followed. Preliminary experiments indicated that minimal spreading and improved adhesion result for bakes at this temperature. Higher temperature bakes can cause flowing of the resist and degradation of very fine patterns.

Following the post-bake, the samples were ready for wet etching of the metal layer being masked by the PMM. After sample cleaning, Film Electronics Inc. C-25 resistor etch at a constant 55°C was used for etching. The etch rate is about 500 Å/min. Good temperature control was imperative for reliable etch rates, and a fresh solution was heated for each sample etch. An immediate distilled water quench followed the timed etch. The samples were then examined in a high power optical microscope to determine the quality of the etch (whether undercutting or incomplete material removal had occurred). If the sample appeared satisfactory, the PMM resist was then stripped, using ethyl acetate, by means of a 5 minute soak followed by a 30 second fine aerosol spray and air drying.

In a few cases, implant masks were fabricated directly in the resist, using thicker $0.9\ \mu$ layers of PMM located directly on the planar diode surface. In this situation, the patterns were written directly in the resist, developed as described above, and then implanted.

After the high resolution chrome patterns were exposed to ion implantation, complete photomicrograph documentation of the chrome patterns was made using the high resolution Coates and Welter scanning electron microscope. Since the patterns were extremely small with respect to the relatively large area planar diode, mapping was later required in order to relocate the patterned areas on the target. From these micrographs the size of the ion beam written regions could be determined.

Table 6 lists the high resolution ion writing experiments of the fourth quarter and the associated implant parameters. Some sample numbers occur several times because the substrates were of superior quality and were reused. Only a fraction of the available active area of the planar diode was utilized during each writing exercise. Most of the writing experiments involved implantation of xenon because of its high writing efficiency, low lateral scattering, and the ease with which very shallow implantations could be achieved on available equipment.

DISCUSSION OF ION WRITING RESULTS

Figure 28 shows a typical electron beam readout as measured in the Coates and Welter field emission microscope. The top

TABLE 6

LISTING OF ION WRITING EXPERIMENTS ON SAMPLES
WITH HIGH RESOLUTION PATTERNS PRODUCED BY ELECTRON
BEAM LITHOGRAPHY (all but ASI samples had back contacts)

Sample	Fluence (ions/cm ²)	Energy (keV)	Ion	Diode Fluence (ions/cm ²)	Thinned Diode	Back Contact
A76E	10 ¹¹	40	Si	10 ¹⁴	no	yes
A51B	4 x 10 ¹¹	145	Xe	10 ¹⁵	no	no
B13A	10 ¹¹	40	Xe	10 ¹⁵	no	yes
	10 ¹²	145	Xe	10 ¹⁵	no	yes
B16A	10 ¹²	40	Xe	10 ¹⁵	no	yes
A51A	10 ¹¹	40	Xe	10 ¹⁵	no	no
	10 ¹¹	40	Xe	10 ¹⁵	no	no
A105A	Broken			10 ¹⁴	yes	yes
A105B	10 ¹¹	40	Xe	10 ¹⁴	yes	yes
A101B	10 ¹¹	40	Xe	10 ¹⁴	yes	yes
	4 x 10 ¹¹	145	Xe	10 ¹⁴	yes	yes
A76B	10 ¹¹	40	Xe	10 ¹⁴	no	yes
	4 x 10 ¹¹	145	Xe	10 ¹⁴	no	yes
A76D	5 x 10 ¹¹	40	Si	10 ¹⁴	no	yes
	10 ¹¹	40	Xe	10 ¹⁴	no	yes
A76C	10 ¹¹	40	Si	10 ¹⁴	no	yes
A73A	3 x 10 ¹¹	40	Si	10 ¹⁴	no	yes
AR1-17(1)	2 x 10 ¹²	60	Ar		no	yes
AR1-17(2)	10 ¹³	145	Xe		no	yes
B13D	10 ¹³	145	Xe	10 ¹⁵	no	yes
AR1-17(4)	10 ¹³	75	Xe		no	yes
A102C	10 ¹³	145	Xe	10 ¹⁴	yes	yes
B15D	10 ¹²	145	Xe	10 ¹⁵	no	yes

micrograph is a secondary image of the chromium pattern. The chromium film is the lighter shade (higher secondary emission). Beam energy and magnification and a 1 micron bar are indicated in the lower left-hand corner of the micrograph. The magnification applies only to the original 4 inch x 5 inch photograph.

Readout by secondary imaging of a hole in a metal film is shown in Figure 29. This is drawn to scale for a chromium thickness of 1000 Å and a hole size at the top of 0.2 μ. Since care

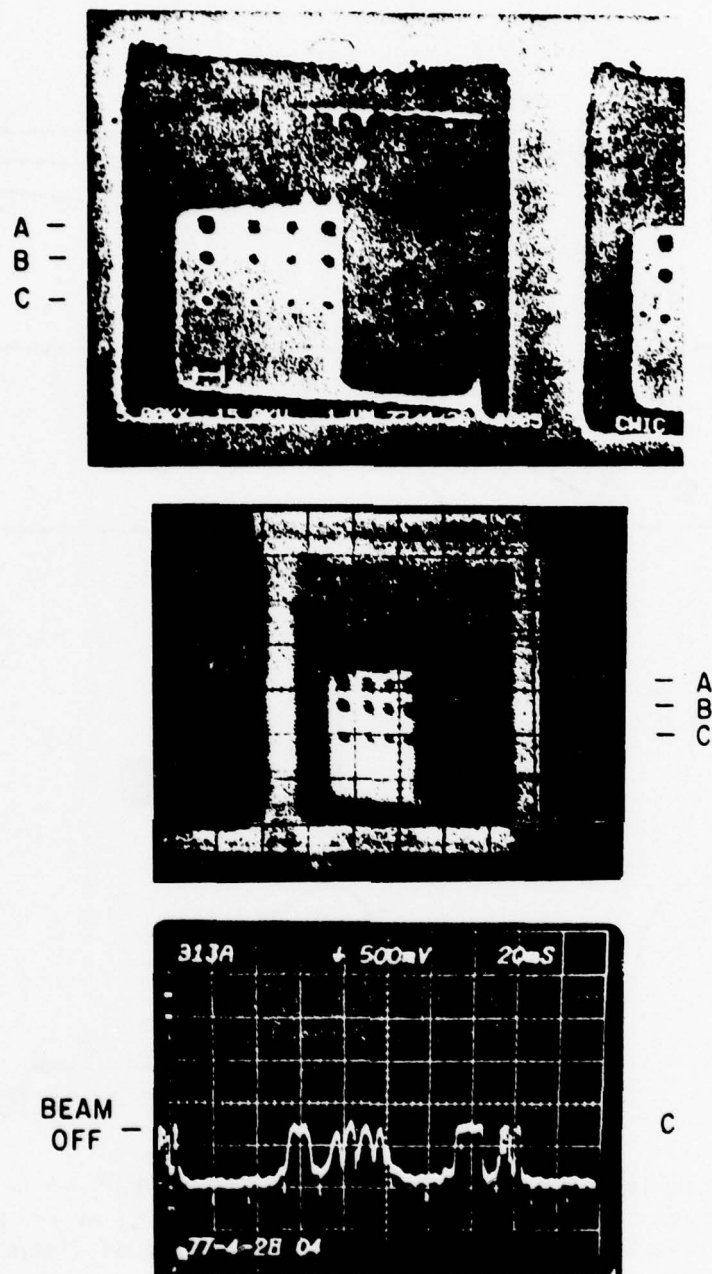


Figure 28. Electron Beam Readout of Written Patterns in Sample B13A. (Top photo is the secondary image of the chromium pattern after implant. Second photo is a diode signal modulated micrograph after stripping of chromium. Bottom photo is a scope trace from line C of the micrograph.)

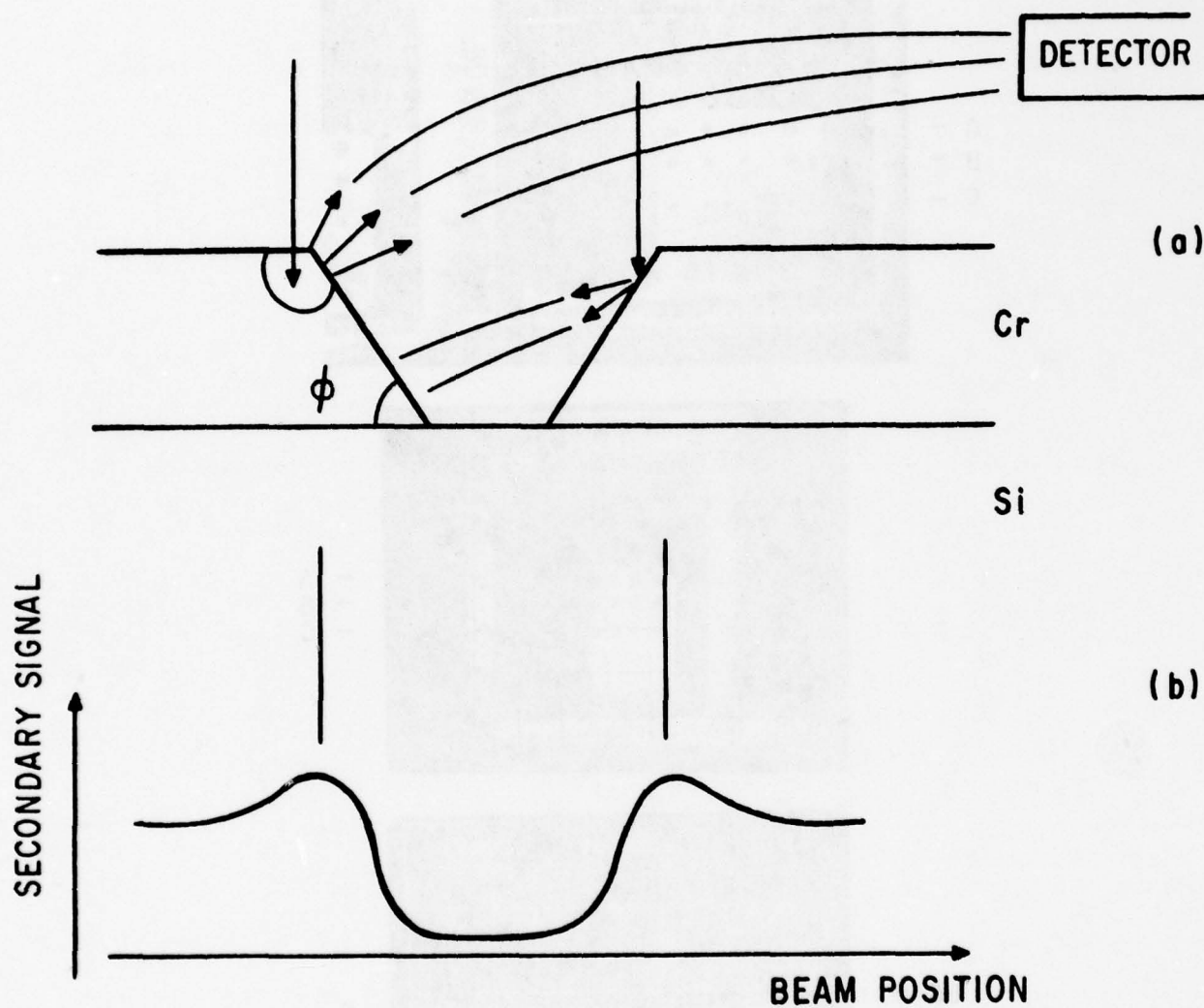


Figure 29. Secondary Imagery of an Etched 'Hole' in a Metal Film.
 (a) Secondary Generation as a Function of Beam Position
 (b) Secondary Signal as a Function of Beam Position

was taken not to overetch the films, there is probably considerable taper to the etched edges and little undercutting. On the left, the electron beam is shown incident just outside of the top edge. A large number of secondaries are generated by high energy electrons within the excitation volume in the chromium. For the 15 keV electrons used, the diameter of this excitation volume is about 0.5μ . Hence there will be a bright edge around the outside of the true hole. As the beam passes into the hole, shown on the left in the figure, a large number of secondaries will be generated, but these will tend to be directed toward the substrate and may not readily be collected by the detector. As the beam passes further down the sides of the hole, the collected secondary signal will drop. This is summarized in Figure 29, where a typical secondary signal is shown as the beam scans across the hole.

For the typical writing experiments discussed here, the writing ion energy was chosen so that the penetration in chromium was $\lesssim 200 \text{ \AA}$. Hence the hole diameter of interest is essentially the diameter of the bottom of the hole. There are two ways to estimate this from a micrograph such as that shown in Figure 28. (1) Measure the size of the inside diameter of the bright ring. This corresponds approximately with the beginning of the taper into the hole. Then subtract $2T \cot(\phi)$, where T is the film thickness and ϕ the taper of the etch. Since care was taken not to overetch, $\phi \sim 45^\circ$. (2) Measure the diameter of the dark center of the hole. Especially for small holes; (1) will be an upper limit estimate as discussed above. Methods (1) and (2) will be used to estimate upper and lower limits for the hole sizes from secondary images.

In Figure 28 the smallest hole is $0.1 \pm 0.05 \mu$ in line C. In the second photograph, a diode signal micrograph is shown after the chromium was stripped. The array of 12 holes of varying sizes is clearly seen. The third photograph is a scope trace across line C. The fine patterns near the center are the readout from the four holes including the hole (second from left) which is $0.1 \pm 0.05 \mu$. The high frequency downward spikes are system noise. This demonstrates that 0.1μ structures can be read out from such written diodes. Figure 30 shows additional data from the same sample. Note, in particular, the fine line structures in line A. These vary between 0.1 and 0.3μ in width and are also clearly distinguished. Lines C and D show readout from holes in the range 0.15 to 0.4μ .

Figure 31 shows a plot of the normalized readout gain from structures of various sizes for sample B13A. Figure 31(a) shows data from written and unwritten bars and Figure 31(b) shows data from written holes. The sizes in each case are taken as the upper limit by method (2) and thus are pessimistic. The gain is normalized to the maximum gain of the unwritten target. The electron beam voltage is 2 keV , and the unwritten target gain is 220. Note that the readout gain for the written holes begins to degrade significantly at about 0.3μ . Based on the resolution model, this would be expected to occur at 0.1μ . Some or all of this discrepancy can be explained by the pessimistic hole size estimates used in this plot. More careful definition of the chromium hole size will be necessary to resolve this fully. In this regard, thinner chromium films and improved etching techniques will be investigated.

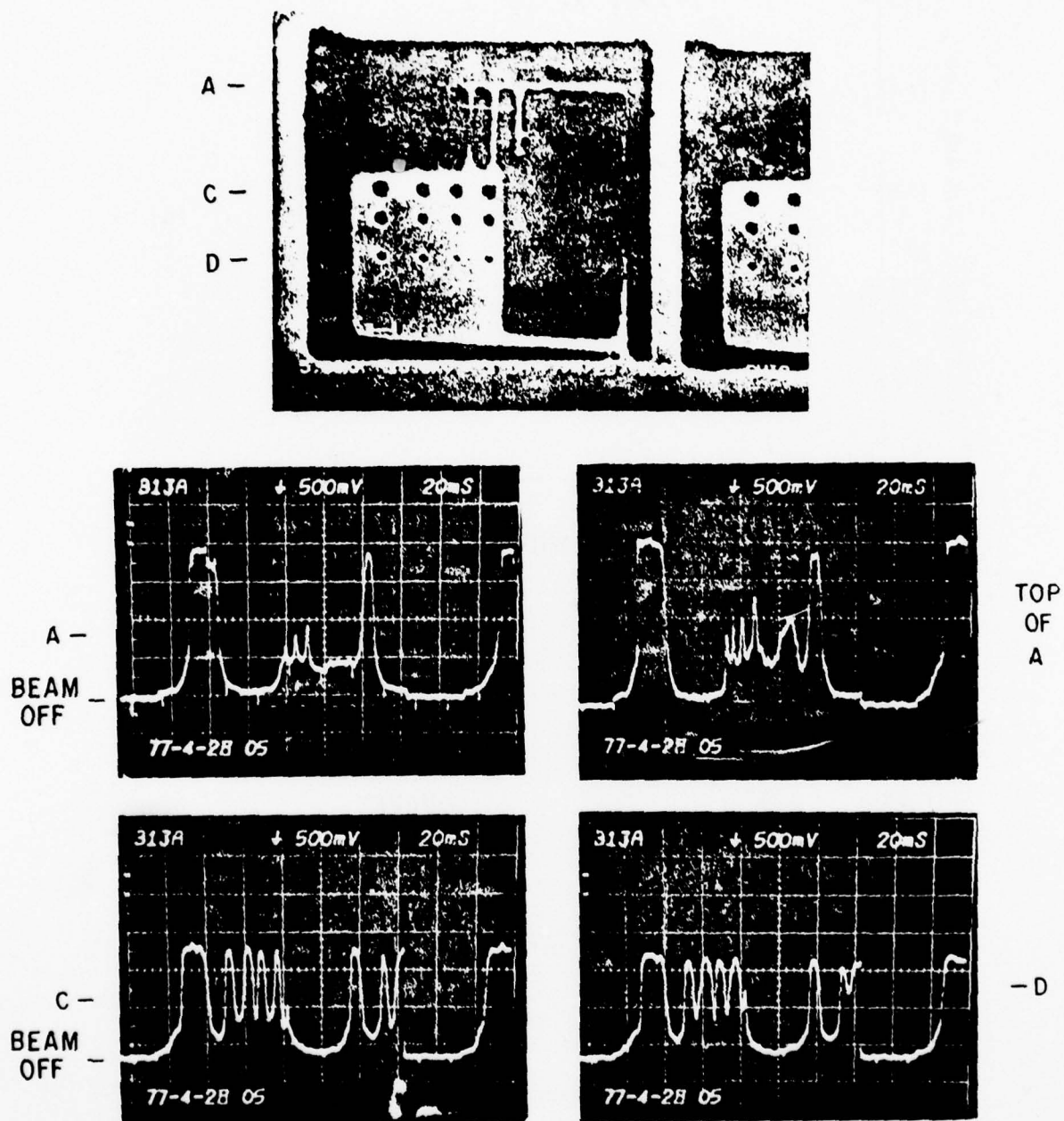


Figure 30. Electron Beam Readout of Written Patterns in Sample B13A

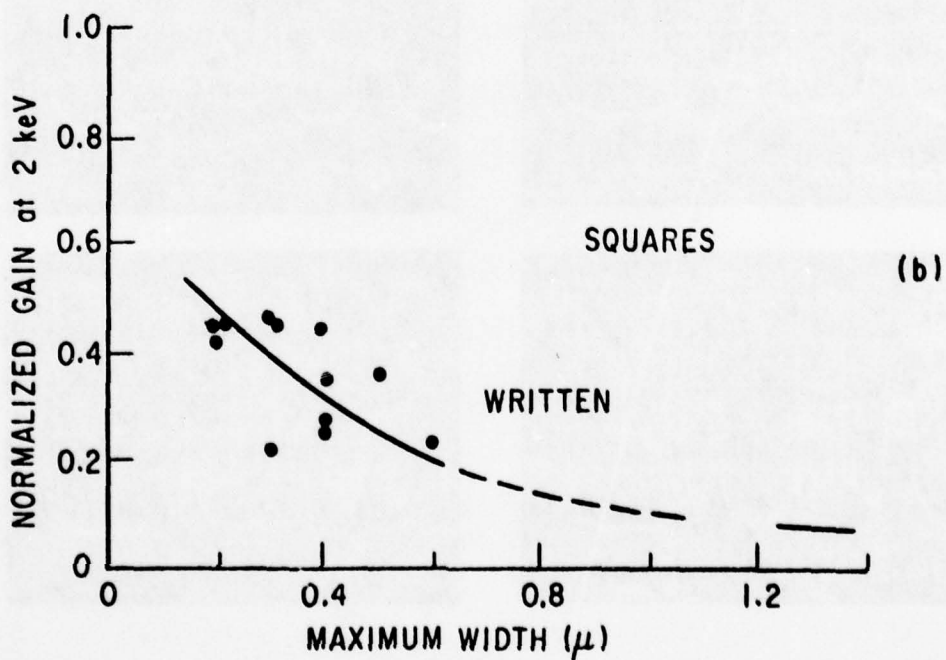
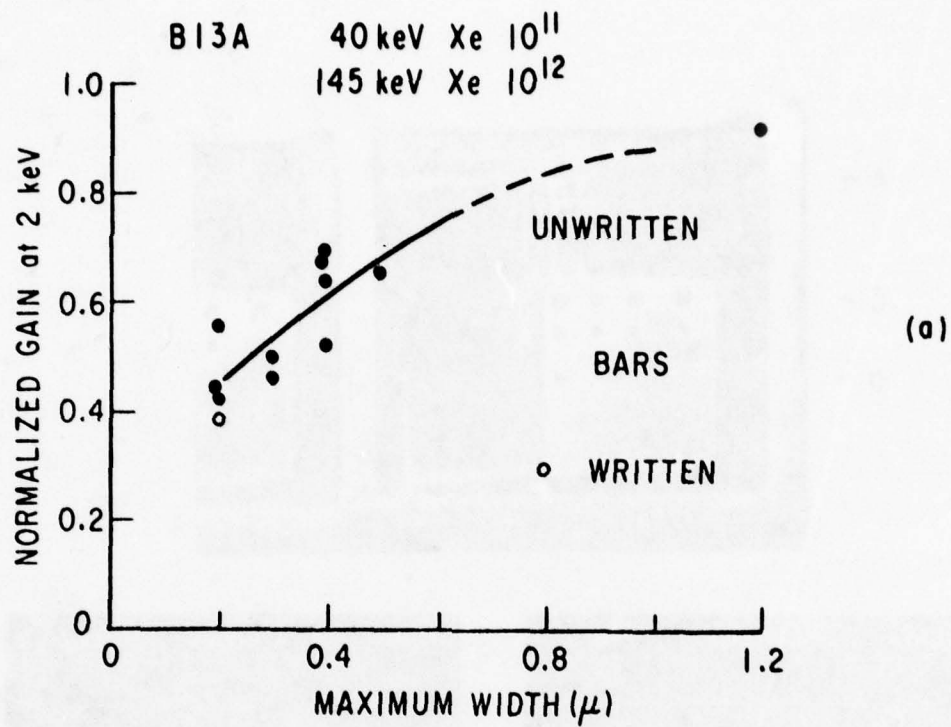


Figure 31. Normalized Gain Data from Sample B13A. (Beam energy is 2 keV.)

The gain for unwritten bars degrades gracefully starting at about 1μ . This again is not in agreement with the resolution model which predicts the onset of degradation of isolated unwritten areas at sizes of $\sim 0.3 \mu$. This could be related to problems with the diode boundary condition as discussed in the previous section. A similar problem will be seen on other samples.

Figure 32 shows typical results from sample B13D. This planar diode is identical to sample B13A and is, in fact, from the same processed wafer. The principal difference is in the writing conditions. Sample B13D was written at a higher fluence of Xe^+ . Again, structures, particularly holes $< 0.1 \mu$ in diameter, can be distinguished. Note the poor edge acuity achieved in the chromium etch for this sample. The actual opening in the small chromium holes is probably 0.05μ or less. These holes can be seen in the diode signal micrograph and in the scope traces for line B. Readout from the unwritten squares in lines C and D shows very clearly an interesting effect, which is defined as the disconnection effect. The peak readout signal level from these areas is much less than full gain, however, the shape of the waveform is squared off indicating that resolution degradation effects due to ion or electron scattering or lateral carrier diffusion are not the cause for the low gain. This effect can be seen clearly in the data plots in Figure 33.

Figure 33(a) shows the normalized readout gain at 2 keV for written and unwritten bars. These are similar to the results on sample B13A. Figure 33(b) shows the results for written and unwritten squares. The written square results are similar to those

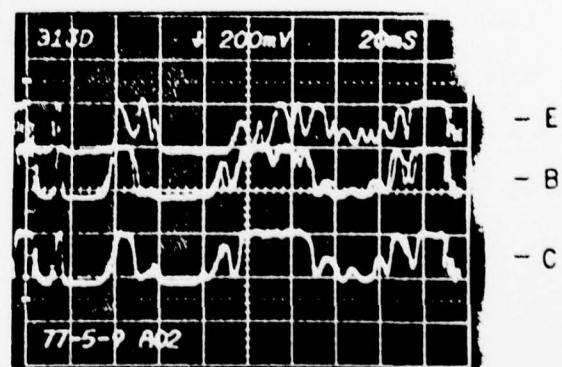
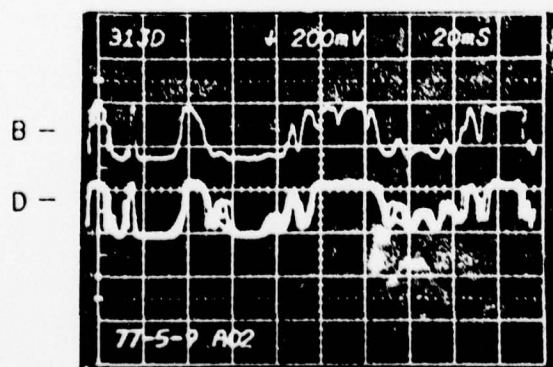
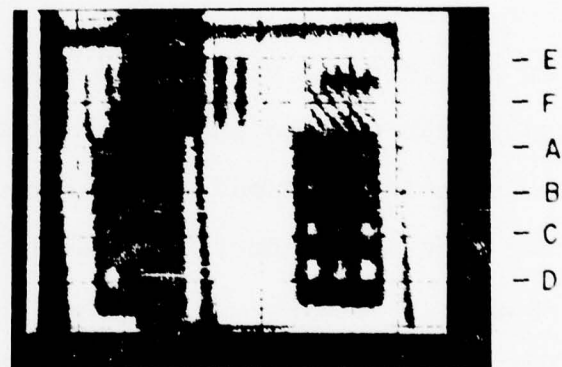
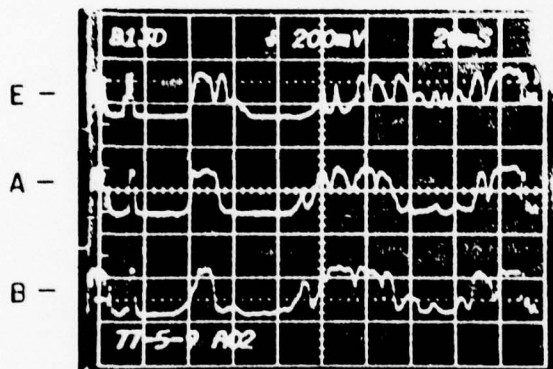
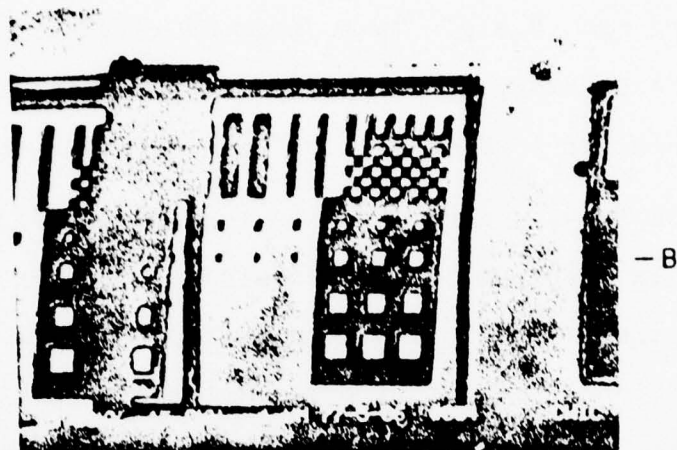


Figure 32. Electron Beam Readout of Written Patterns in Sample B13D

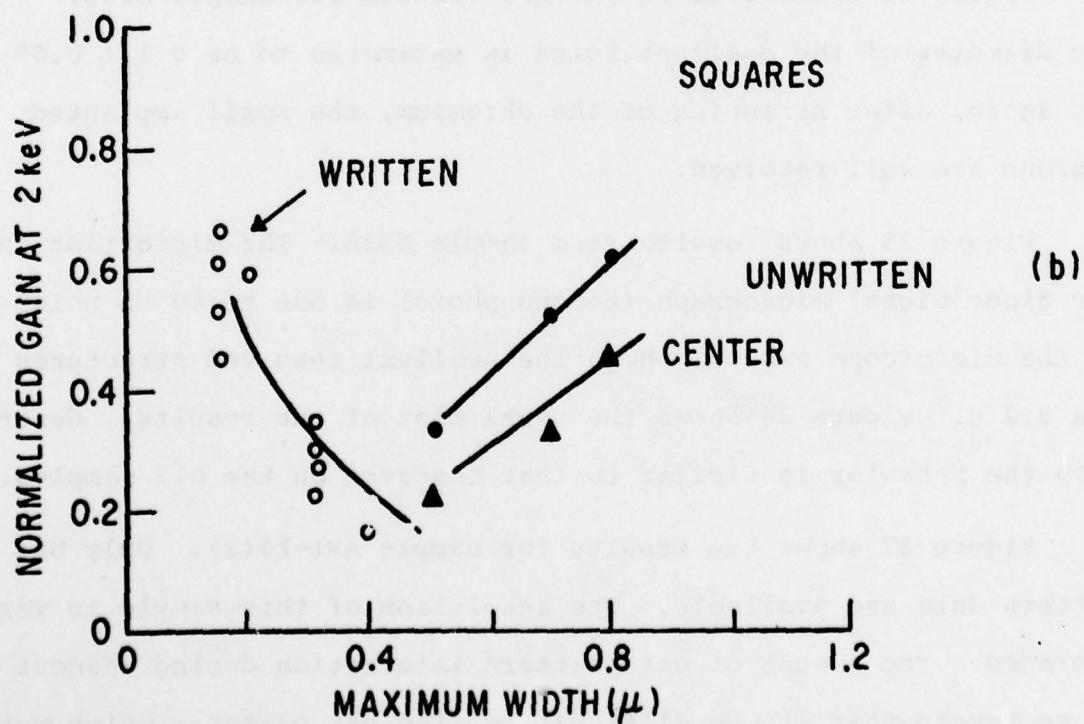
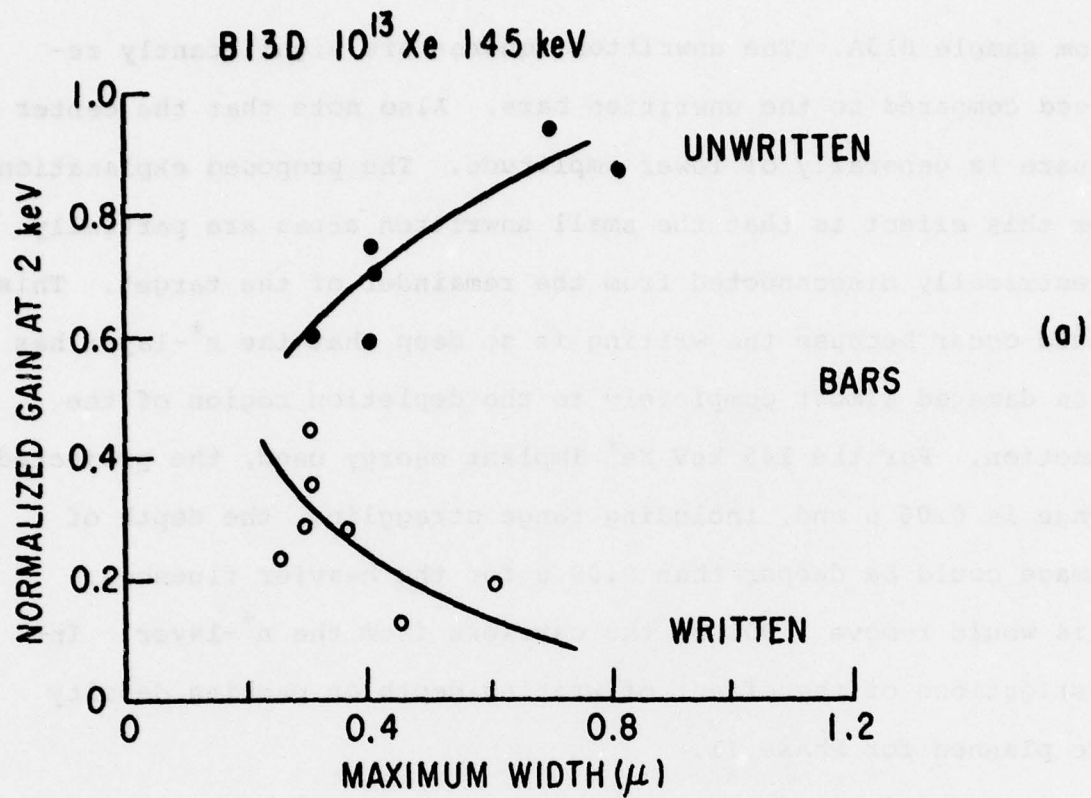


Figure 33. Normalized Gain Data from Sample B13D. (Beam energy is 2 keV.)

from sample B13A. The unwritten squares are significantly reduced compared to the unwritten bars. Also note that the center square is generally of lower amplitude. The proposed explanation for this effect is that the small unwritten areas are partially electrically disconnected from the remainder of the target. This could occur because the writing is so deep that the n^+ -layer has been damaged almost completely to the depletion region of the junction. For the 145 keV Xe^+ implant energy used, the projected range is 0.06μ and, including range straggling, the depth of damage could be deeper than 0.09μ for the heavier fluences. This would remove $> 90\%$ of the carriers from the n^+ -layer. Investigations of the effect of writing depth on packing density are planned for Phase II.

Figure 34 shows some additional results for sample B13D. The diameter of the smallest holes is estimated to be $0.1 \pm 0.05 \mu$ and again, after stripping of the chromium, the small implanted regions are well resolved.

Figure 35 shows results from sample A51B. The distortion in the diode signal micrograph (second photo) is due to 60 Hz noise in the microscope sweeps. Here the smallest resolved structures are 0.2μ . Figure 36 shows the usual plot of the results. Generally the behavior is similar to that observed on the B13 samples.

Figure 37 shows the results for sample AR1-17(1). Only bar pattern data are available. The resolution of this sample is very degraded. The amount of data pattern interaction during readout is so severe that it was difficult to find bar patterns which were long enough and widely enough spaced so that the readout signal

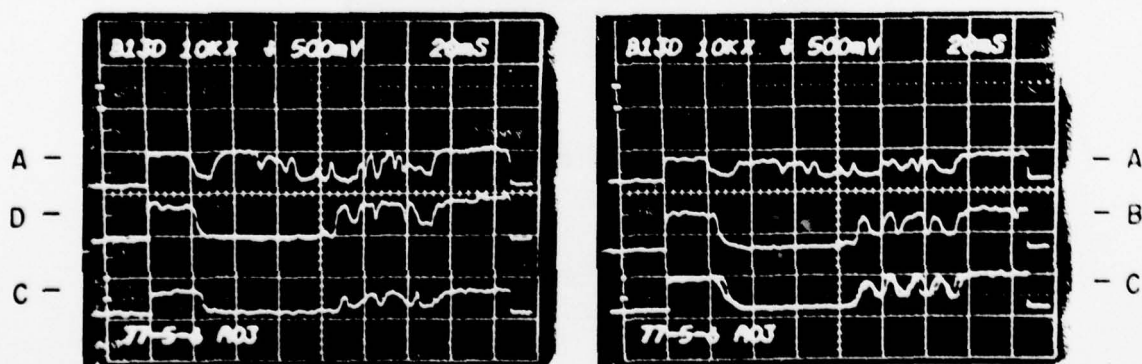
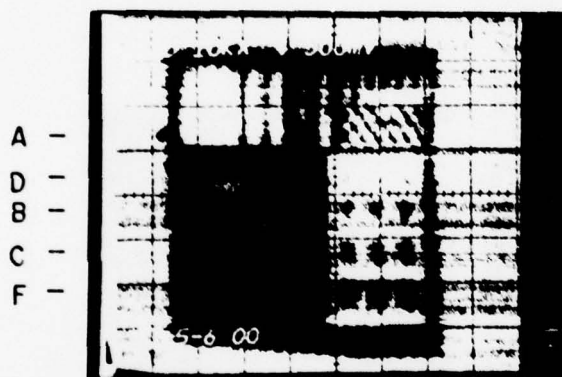
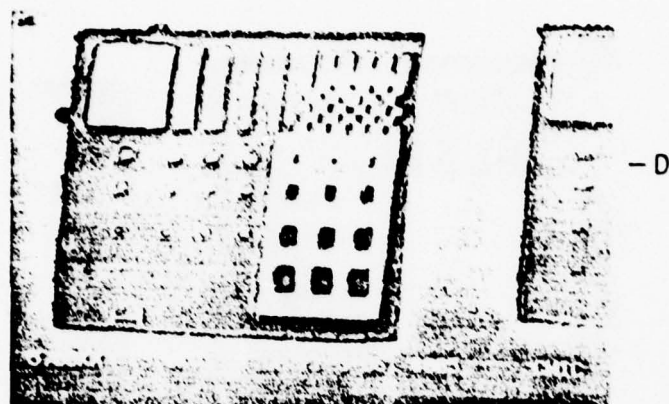


Figure 34. Electron Beam Readout of Written Patterns in Sample B13D

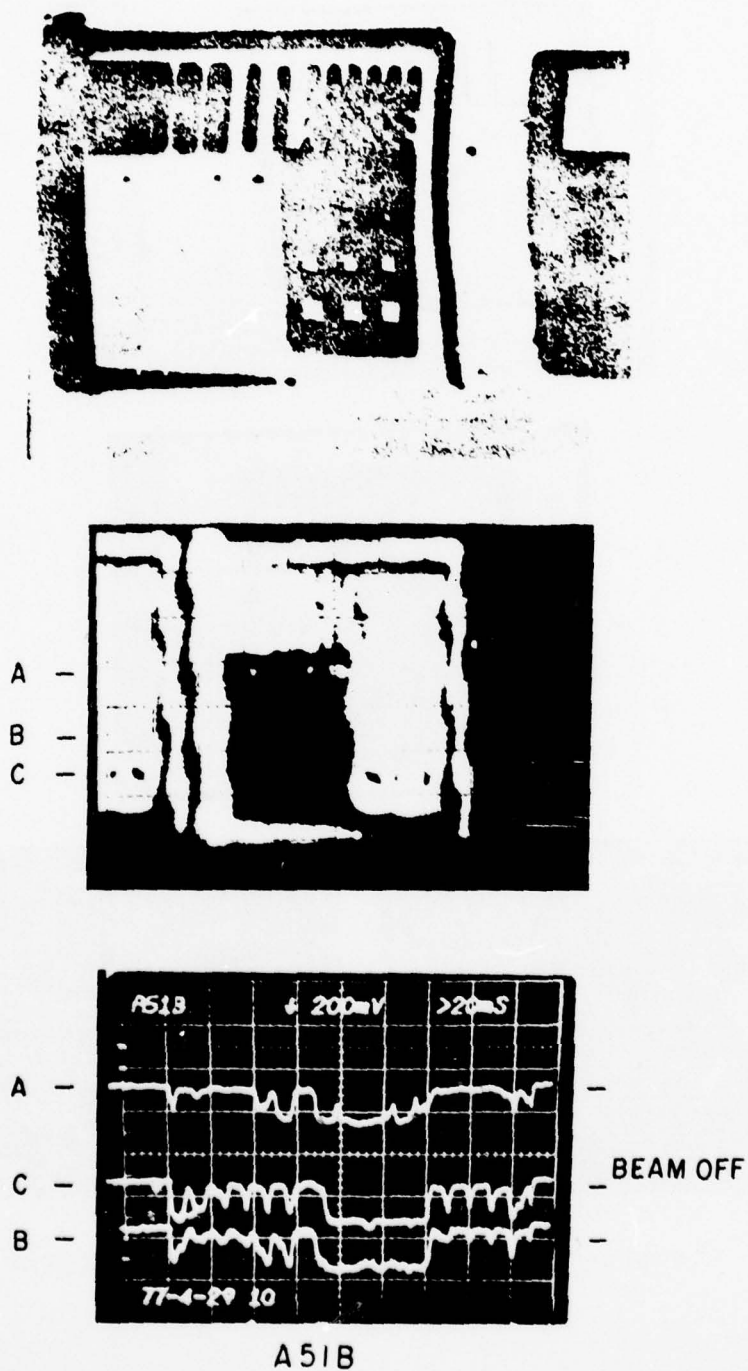


Figure 35. Electron Beam Readout of Written Patterns in Sample A51B

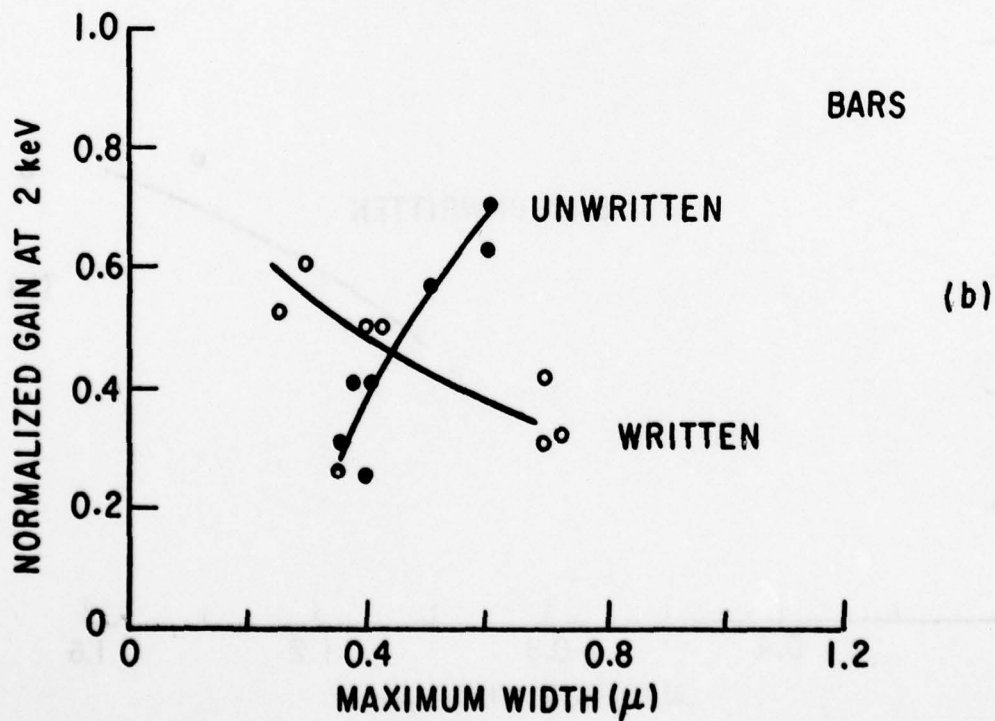
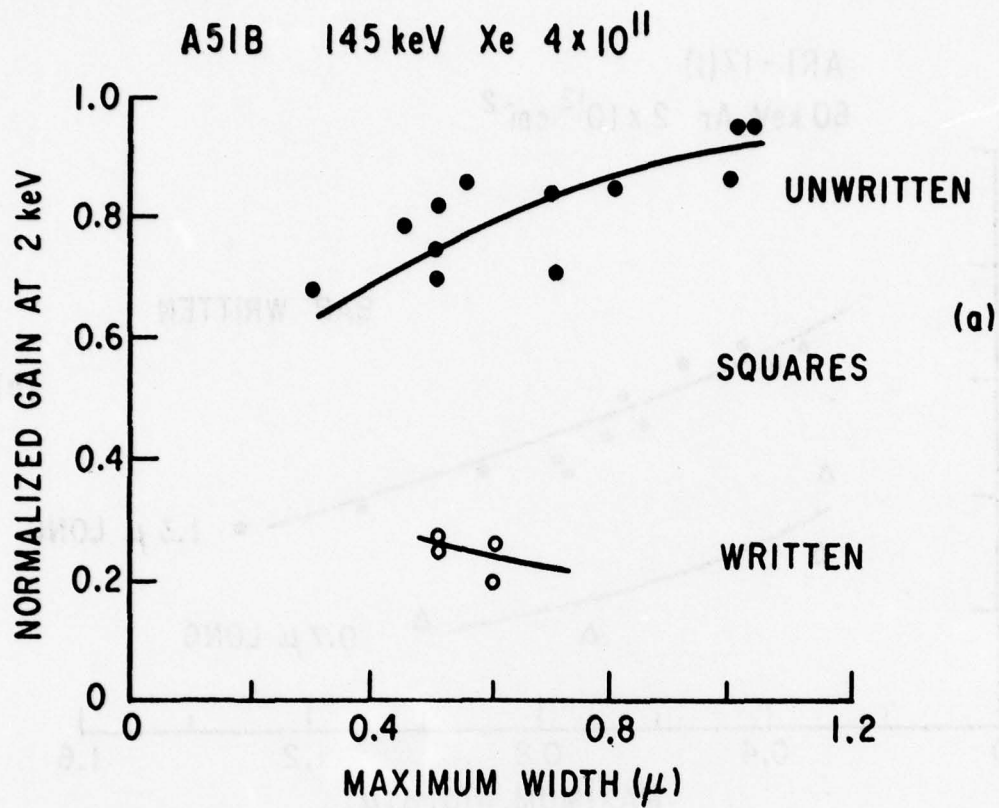


Figure 36. Normalized Gain Data from Sample A51B. (Beam energy is 2 keV.)

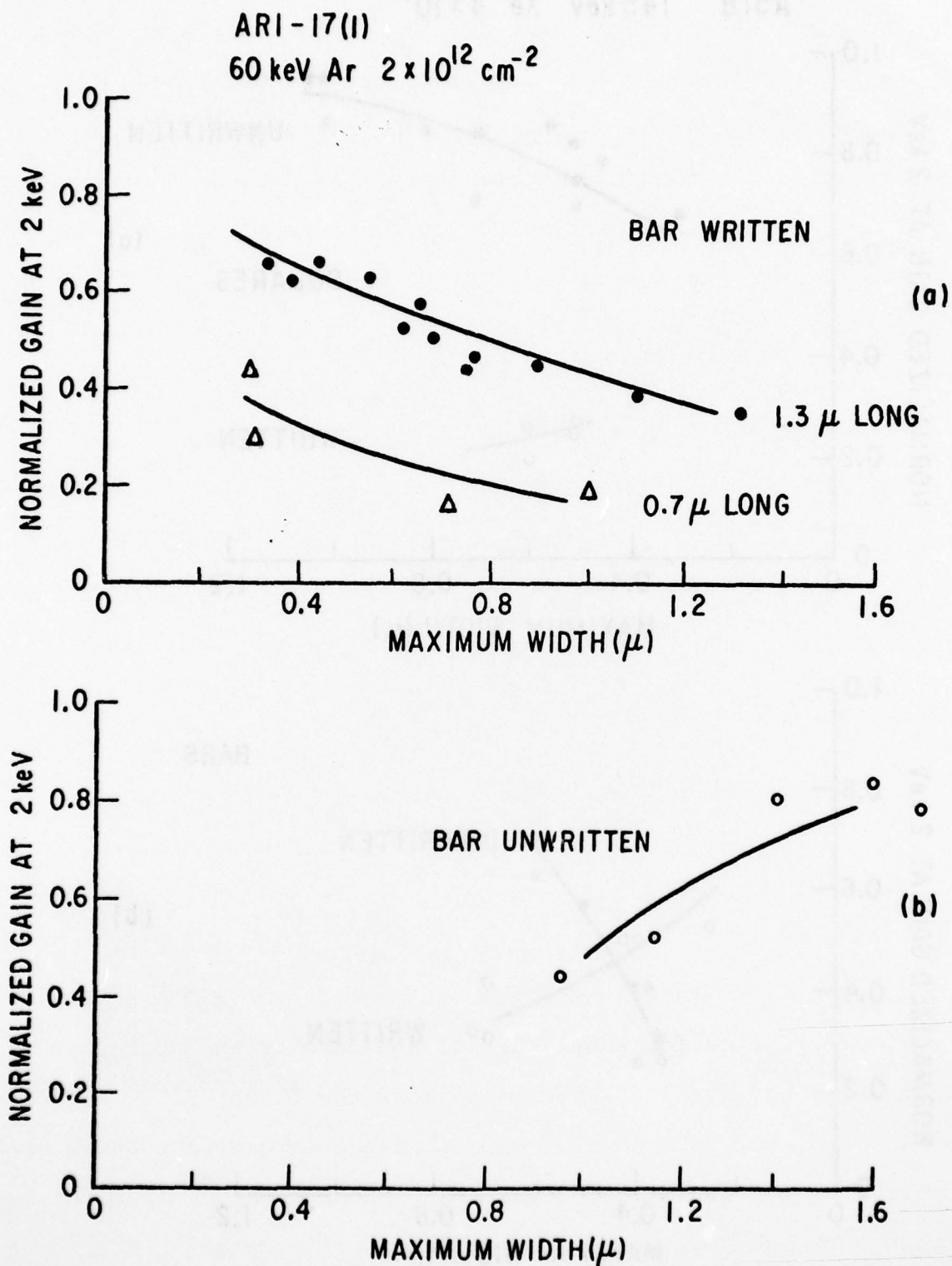


Figure 37. Normalized Gain Data from Sample ARI-17(1). (Electron beam energy is 2 keV.)

was characteristic of a truly isolated bar. For the written bars, two curves are shown. The top curve is for bars which are 1.3μ long, while the bottom set is for bars that are 0.7μ long and have large written areas on one end. The large written area depresses the signal from the written bars. As discussed at the end of Section II, this particular diode showed a very large dependence for written area gain on diode bias. It is possible that the behavior of sample ARL-17(1) is only a more extreme case of a general behavior for all of the targets. Possible remedies for this are discussed in Section II.

Results on the other samples are not reported for various reasons including poor chromium patterns, noisy diodes, and incorrect choice of writing conditions. In general the B^+ implanted planar diodes gave better performance than the As^+ implanted diodes. Two possible explanations for this are: (1) the writing process is different in p-type material. Since the dependence of the readout signal for large written areas on writing ion fluence and energy is generally the same for both the arsenic and boron samples, this is considered unlikely. However, further studies of the differences in writing behavior between As^+ and B^+ planar diodes, including the effect of As^+ and B^+ implant fluence (doping level), are planned for Phase II; (2) the density and character of the residual defects left after anneal of the planar diode are different. Since B^+ is a lighter ion, it tends to generate fewer and simpler defects than arsenic. Also any knock-on atoms from the oxide layer or contaminants during implant will penetrate less for B^+ than As^+ because the average energy transferred to knock-on atoms

is less for a lighter implanted ion. Hence there should be fewer defects in the diode depletion region for the B^+ samples. This could make an important difference in the diode boundary condition as discussed in the previous section.

SECTION VI

ALLOY JUNCTION WRITING EXPERIMENTS

Alloy junction writing experiments have been performed using a laser system and, most recently, using an electron beam system. During the first three quarters of the contract period, experimental measurements of the properties of laser-formed alloy junctions in Al-Si and Au-Si systems showed encouraging results. Recent laser studies, reported below, indicate that the In-Si system may also be used for alloy junction writing. This system is comparatively attractive because of its low eutectic temperature. Initial attempts were also made to form alloy junction diodes using the electron beam writing station. These studies are being continued in the present phase of the Program.

LASER WRITING

The laser writing approach was initiated to determine the feasibility of the alloy junction method before the electron beam writing equipment was available. The experiments were performed to answer two questions:

1. Can an alloy be formed using a very short pulse of heat?
2. Can alloy junction surface diodes be formed by raising the temperature of the metal semiconductor to just above the eutectic point?

As discussed in the prior quarterly reports, these questions were answered affirmatively by measuring the properties of laser-written Al-Si and Au-Si metal semiconductor systems.

During this quarter, laser writing experiments were performed using an In-Si metal semiconductor system. The same neodymium-YAG

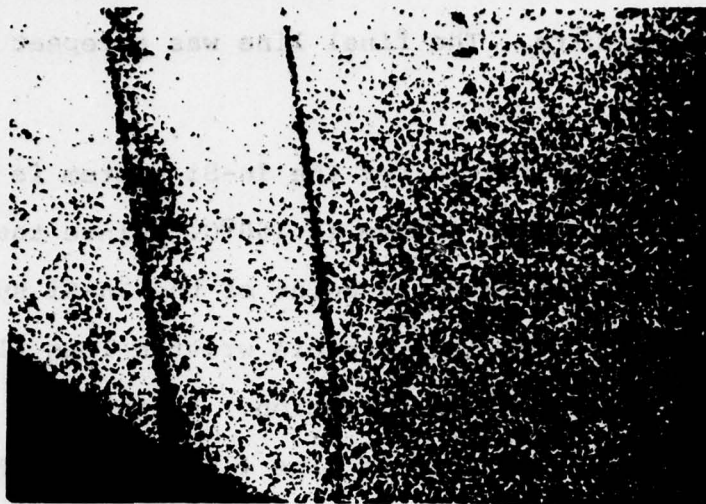
laser system (an Electroscientific Industries Model 25 laser trimmer) was employed. Based on prior analytical work, the In-Si system did not look attractive for alloy junction writing because of the low solubility of indium in silicon at the eutectic point. However, the low temperature of the eutectic point in this system would give it a competitive advantage. The target for the In-Si system was a BEAMOS (beam addressed metal oxide semiconductor)-type n/p diode with a 500 Å thick evaporated indium layer on the top surface. The laser system operating conditions were:

- 14 A lamp drive
- 50 mil aperture
- 2 kHz write rate
- 10% beam splitter
- reverse thick film optics.

As in previous experiments, the beam power was reduced in steps by the use of neutral-density (ND) glass filters from the initial conditions listed above. Figures 38a and 38b show lines of laser writing on an In-Si sample. Starting with the above-mentioned laser operating parameters, the lines correspond to:

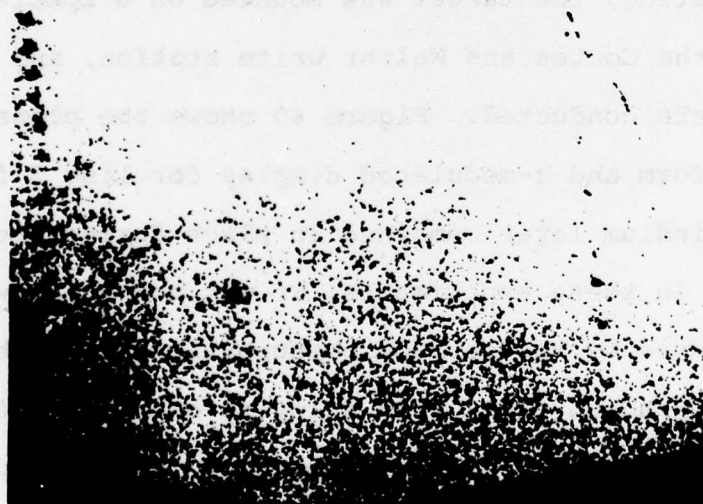
- line #1 - 0.2 ND filter
- line #2 - 0.3 ND filter
- line #3 - 0.4 ND filter
- line #4 - 0.5 ND filter
- line #5 - 0.6 ND filter
- line #6 - 0.2 ND filter

Line 4 was the lightest "visible" line to be written. Line 5 was



1 2 3

(a)



3 4 5 6

(b)

Figure 38. Laser Writing Patterns on In-Si Target (SEM).
 (Single pulse per spot. Laser - 14 A lamp,
 50 mil aperture, 2 kHz rep rate, 10% B.S.)

written with another step reduction of beam energy, but did not produce visible results. The final line was a repeat of the first recorded line.

The eutectic temperature for the In-Si system is 156°C and the melting temperature of indium is 160°C . Since the melting point of indium and the eutectic point of the In-Si system are only 4 degrees apart, the last visible written line (line 4) also corresponds to the last diode formation. An enlarged image of one of the laser written spots of line 4 is shown in Figure 39. Considerable "balling" of the indium film in the written area is noted. These lines were formed with a single 150 nsec pulse per spot.

After writing, the target was mounted on a special holder designed for the Coates and Welter write station, and reading experiments were conducted. Figure 40 shows the planar diode readout wave form and z-modulated display for line 3 formed "bit sites." The indium layer remained in place during these readout experiments. In these experiments, it was not clear whether the signal was caused by the surface perturbations from the laser heating of the indium film or if alloying had occurred. To characterize the writing method, the indium was etched from the target. Figure 41 shows a planar diode readout from the sample area; an 8 keV beam energy was used. A reduced gain in the laser written regions is still apparent. (The bright area at the right edge of the laser writing and the step in the current pulse indicates reduced gain due to beam penetration in the metal layer.) It was concluded that the written areas do behave as

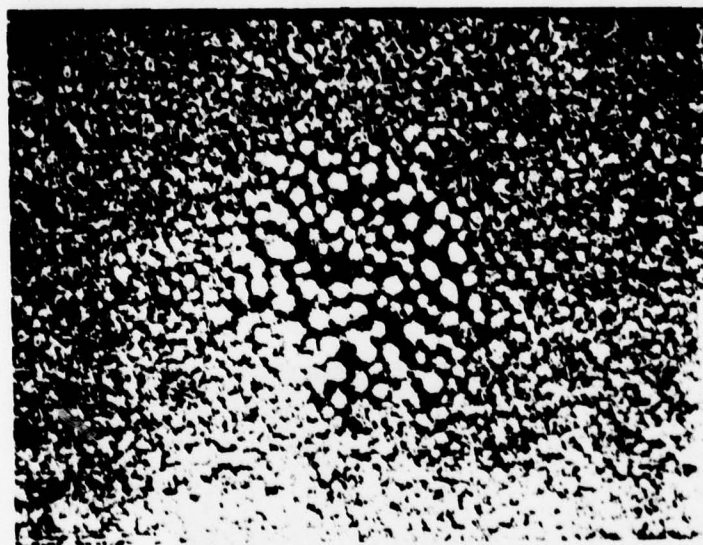


Figure 39. Close-up of Laser Irradiated
Spot from Line 4

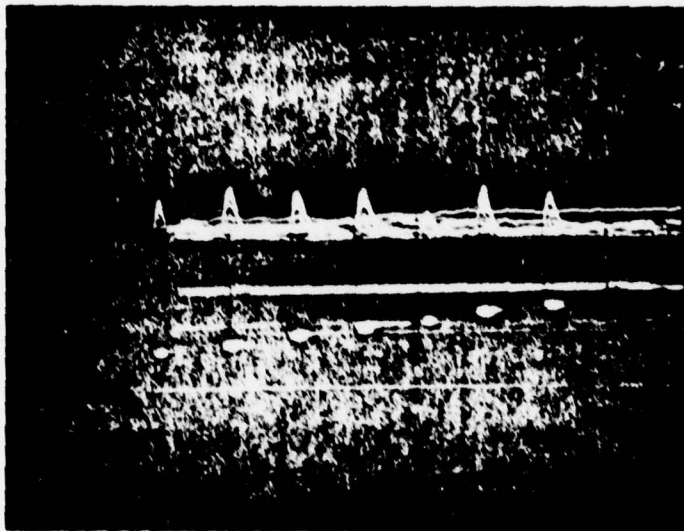


Figure 40. Planar Diode Current Signal and z Modulated Display from Readout of Line 3 Before Removal of the Indium Layer

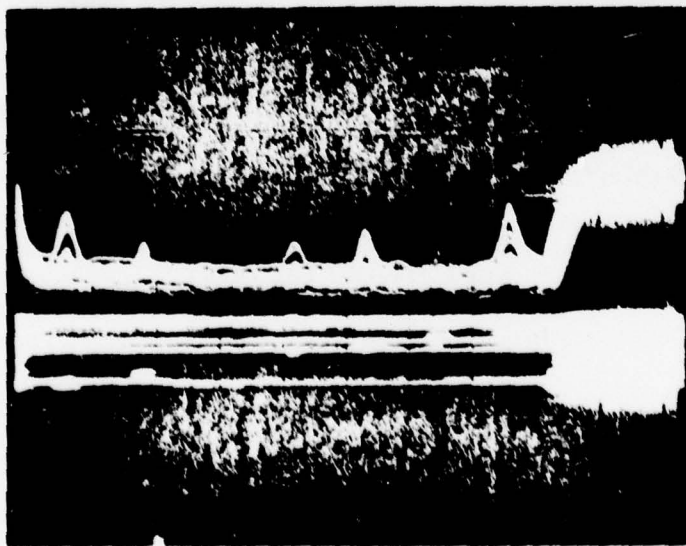


Figure 41. Planar Diode Current Signal and z Modulated Display from Readout of Line 3 After Indium Layer Was Removed

alloyed regions. This was a surprising result because the low solubility of the Si-In eutectic had appeared to be a substantial barrier to laser writing. Nevertheless, the In-Si system does appear promising for electron beam writing and, because of its low eutectic point, it does not require the high thermal bias of some other metal semiconductor systems.

ELECTRON WRITING

The electron beam write station had been made operational and slow scan electronics developed so that electron beam writing experiments could begin during the fourth quarter. Because of the success of laser writing using the In-Si system, this was the first metal-semiconductor system tried in the electron writing equipment. The same target configuration, that is, a BEAMOS-type n/p diode with a 500 Å thick evaporated indium film was used for the electron writing experiment. The stage holding the target and the target itself were thermally biased to approximately 150°C. Electron beam writing was attempted with a beam landing potential of 6000 V and a beam current of 150 nA. The spot size was estimated to be on the order of 1000 Å. Figure 42 shows a secondary electron image of the surface where electron beam writing was attempted; a line caused by the beam is visible. Figure 43 shows planar diode readout of this written line. Note that the writing from the planar diode signal appears spotty. As before, it was not known if these signals were caused by perturbations of the indium film or whether actual alloying had taken place. Thus, the indium metal was stripped from a portion of the written area and readout in the electron column was attempted. Unlike the laser

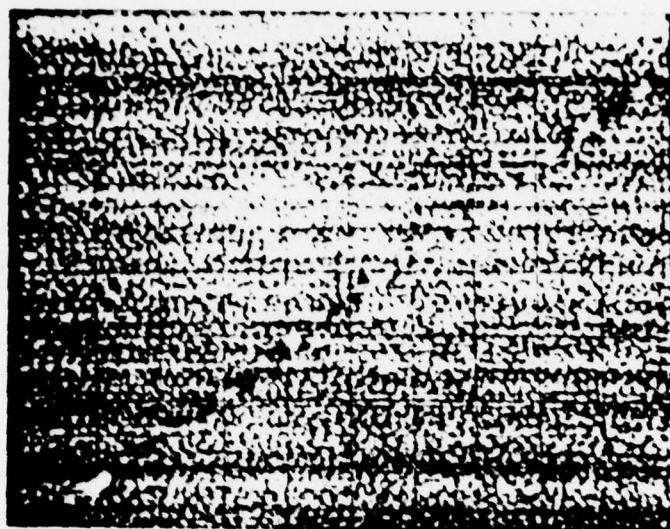


Figure 42. Secondary Emission Surface
Scan of Electron Beam Writing
Area (500 Å In on Si target)

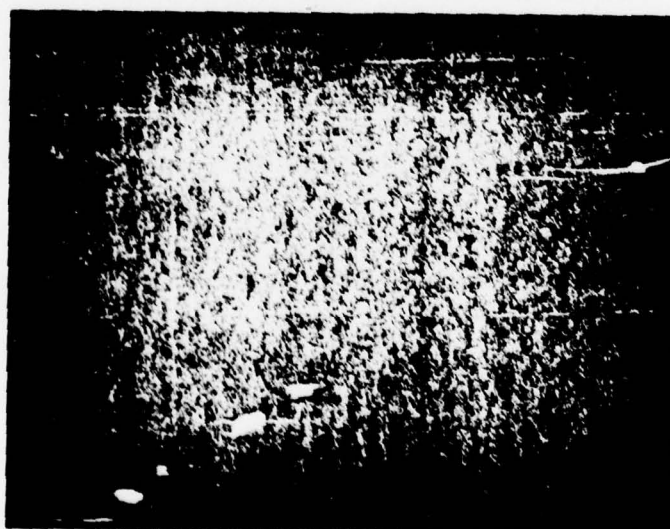


Figure 43. Planar Diode Current z Modulated
Display of Electron Beam Writing
Area (500 Å In on Si target)

writing discussed in the previous section, when the metal layer was stripped, the "writing" vanished. Therefore, it was concluded that the electron beam had melted the indium film but that alloying had not taken place.

Next, a Au-Si system was studied. A 500 Å evaporated gold film was deposited on a silicon planar n/p diode. The Au-Si system has a eutectic temperature of 370°C and the melting point of gold is 1063°C. Therefore, in the case of the Au-Si system, melting could not possibly be achieved with the power available from the electron beam system. The target was thermally biased to a temperature of 367°C, and two writing attempts were made. A 10 kV electron beam was used with currents of 140 nA and 200 nA, respectively. After the target was cooled to room temperature, it was read with an electron beam. The surface was heavily marked with pits of a characteristic triangular etch pit or stacking fault form. This phenomenon is known to occur in metal-Si semiconductor systems.

A secondary emission surface scan showing one of these etched pits in detail is shown in Figure 44. The planar diode readout signal obtained from the etch pit region is shown in Figure 45. At this point it was not known whether the electron beam had induced these pits or whether they occurred because of the thermal bias. Planar diode readout of a larger area of the target is shown in Figure 46. The white dots represent the readout signal from the etch pits on the target surface. The white lines superimposed on the figure are the writing raster for the electron writing. Since there is no correlation between the raster lines



Figure 44. Secondary Electron Surface Scan of Stacking Fault (500 Å evaporated Au on Si target)



Figure 45. Planar Diode Readout of Stacking Fault in Figure 44

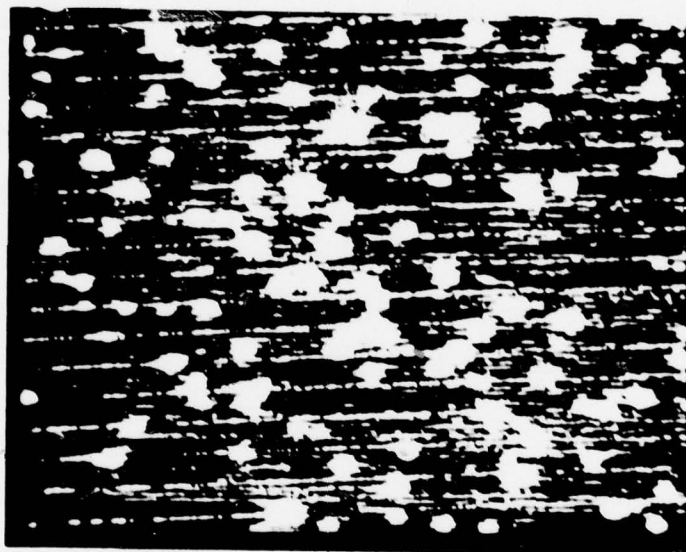


Figure 46. Planar Diode z Modulated Display of Writing Area on 500 Å Au on Si Showing Stacking Fault Readout with Writing Raster Superimposed

and the etch pit formation, the conclusion is that the etch pits were caused by excessively high thermal bias. Unfortunately, the expected temperature rise calculated using the simple hemisphere model was less than 10°C . Therefore thermal bias on the order of 365°C is required.

In an attempt to reduce the thermal conductivity of the metal film and therefore increase the achievable writing temperature with the electron beam, a 500 \AA sputtered gold on silicon target was tried next. Writing was attempted with a 160 nA beam current at 10 kV and 7.5 kV. The target was thermally biased to 360°C . However, in reaching this thermal bias, the temperature did rise for brief periods up to 365°C . Again, as shown in Figures 47 and 48, etch pits were formed and planar diode signals could be read from the etch pit formations.

From these observations of the formation of etch pits at thermal biases on the order of 360°C , it became obvious that, if a Au-Si target was to be used, thermal biases much less than this would have to be employed also. As an alternative, a target consisting of a co-sputtered SiO_2 and gold layer on a silicon target was made. This approach lowers the thermal conductivity of the film. The measured electrical conductivity is from 10 to 100 times smaller for the co-sputtered film than for an equivalent film of pure metal. Thus, a target was made with a SiO_2 -Au co-sputtered film, and writing was tried at bias temperatures of 245, 310, 320 and 340°C . Figure 49 shows secondary electron surface scans of the written area for each of these writing attempts. All writing was done at a 10.5 kV beam potential.



Figure 47. Etch Pit Formation on Sputtered Au-Si Target-Secondary Emission Surface Scan



Figure 48. Planar Diode Readout of Etch Pit on Sputtered Au-Si Target

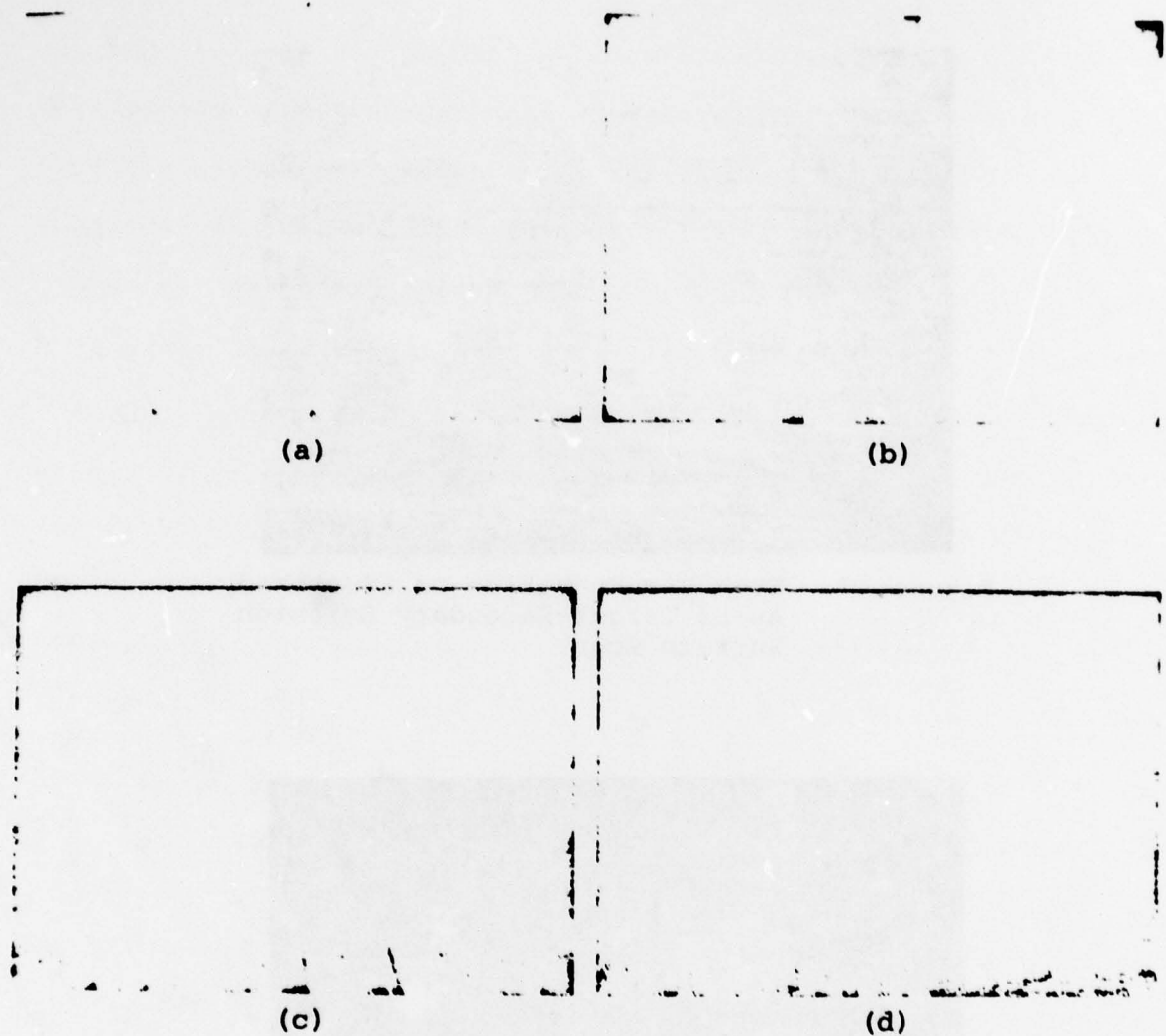


Figure 49. Electron Writing Attempts on $\text{SiO}_2\text{-Au-Si}$ Co-sputtered Target @ Thermal Bias: (a) 245°C , (b) 310°C , (c) 320°C , (d) 340°C

The trials at 245°C and 310°C used 180 nA and 170 nA beam currents, respectively. Faint contamination lines caused by the writing beam can be seen in almost all of these cases. As can be seen from the figure, a very small raster was written and then a larger, more coarse raster, was superimposed. Readout attempts from these areas produced no detectable planar diode signal. These rasters were written with a relatively low writing rate corresponding to about 1/100 second per raster line. Writing was done with a single-scan raster. As a next step, the raster was left on at a given location for 5 minutes. In this case, the same raster time was used. However, a beam current of 220 nA at 10 kV with a 340°C bias was used. Again, no detectable readout was achieved with this writing area.

As a final experiment, the beam was held stationary at a point on the target with 100 nA beam current at a landing potential of 10 kV and a bias temperature of 350°C. Contamination marks for this attempt showed a spot that was on the order of several microns, indicating that perhaps the surface had charged and the beam had wandered, thereby reducing the thermal effect in this period. As with the dynamic writing attempts, no readout was obtained from the stationary beam experiment.

SUMMARY

During this quarter, successful writing was achieved with the laser for an In-Si system. Several attempts were made at electron writing using the Coates and Welter write column for various target configurations consisting of In-Si, Au-Si and a

co-sputtered SiO_2 -Au-Si system. No detectable electron writing was achieved. Etch pit formation with straight gold systems indicates a potential problem with thermal bias. At this point, it is not fully understood why the electron writing attempts failed.

The electron alloy studies will continue in the next phase of this contract. An attempt will be made to closely correlate the electron writing attempts with the laser writing. Mathematical modeling of the writing process will be used to determine why the electron writing has not been successful. Also, various co-sputtered target materials and target materials consisting of ultrafine particles will be examined for potential use in lowering the thermal bias requirement for electron writing. It is hoped that through these techniques, electron writing will be successfully demonstrated during the early stages of the Phase II contract.

SECTION VII

WRITE OPTICS STUDY

INTRODUCTION

Analytical studies of the charged particle write optics began in the third quarter of this contract period. Specific optical information was gathered and specialized tools were developed and used for the detailed analysis of both the electron and ion write columns.

OPTICS STUDY - 3RD QUARTER

During the third quarter of this contract, pertinent data and tools for the detailed analysis of the write optics were gathered and developed. Performance data for electron sources and ion sources considered applicable to the archival writing columns are summarized in Tables 7 and 8. These data were collected from the literature [5], [6], [7], prior work at the General Electric Research and Development Center, personal contacts, and close association with the source development work at the Oregon Graduate Center.

Equations were developed for the maximum available beam current from spherical aberration limited optics for a resolvable object and an ideal nonresolvable point object. Conventional thermionic electron sources and duoplasmatron ion sources have an object size much greater than the final image size. The maximum current equation for a resolvable object is used for these sources and is given by:

TABLE 7
ELECTRON SOURCE PROPERTIES

Source	Cathode Loading (J_0 -A/cm ²)	Operating Temperature (°K)	Source Size (Å)	Energy Spread (eV)	Brightness at 4 kV (A/cm ² /str)	Angular Brightness (A/str)
Ba Dispenser	3	1353	$\sim 2 \times 10^5$	0.117	3.3×10^4	0.102
	5	1393	$\sim 2 \times 10^5$	0.121	5.3×10^4	0.167
	10	1453	$\sim 2 \times 10^5$	0.126	10 ⁵	0.314
Field Emission Room Temp.	$\sim 10^4$	300	$\sim 30 \text{ Å}$	0.20	10 ⁸	3×10^{-5}
Temp. Field						
Zr W	$> 10^4$	1400-1800	$\sim 30 \text{ Å}$	0.7-1.0	$\sim 10^{10}$	10 ⁻³
W(100)	$> 10^4$	1850	$< 30 \text{ Å}$	0.8-1.5	$\sim 10^{10}$	10 ⁻³

TABLE 8
ION SOURCE PROPERTIES

Source	Total Current (A)	Current Density (A/cm)	Energy Spread (eV)	Brightness (A/str/cm)	Angular Brightness (A/str)
Duoplasmatron	10 ⁻³ to 10 ⁻¹	10 ⁻² to 1	10	$< 10^3$	-
Field Ion	10 ⁻⁹ to 10 ⁻⁸	10 ³	2-5	10 ⁵	1.5×10^{-6}
Liquid Metal Field Ion	10 ⁻⁸ to 10 ⁻⁶	$\sim 10^5$?	10 ⁷	10 ⁻⁴

$$I_{\max} = \frac{3\pi^2}{16} \beta_i \frac{d^{8/3}}{C_s^{2/3}} \quad (10)$$

where

I_{\max} = maximum current (A)

β_i = beam brightness at the image (A/cm²/str)

d = final spot size at target (cm)

C_s = spherical aberration constant of lens system (cm)

For an ideal point source (a field electron or field ionization source):

$$I_{\max} = \Omega_{\beta_0} \pi m^2 \frac{V_i}{V_o} \left(\frac{2d}{C_s} \right)^{2/3} \quad (11)$$

where

Ω_{β_0} = source angular brightness (A/str)

m = optic system magnification

V_i = beam potential in image space (V)

V_o = beam potential in object space (V)

d = final spot size at target (cm)

C_s = spherical aberration constant of lens system (cm)

Consideration was also given to the basic column configuration to be used for the archival write optics. At least a two-lens system is required for the ion and electron columns to achieve the proper beam current and spot size (Figures 50 and 51). A possible choice for the electron optics is the short focus plus relay (SFPR) matrix lens concept, shown in Figure 52. This is basically a three-lens system. A two-lens collimating system was selected as the fundamental optics building block (Figure 53). A collimating system such as this has several optical advantages: no crossovers between object and image, lower individual lens aberrations, and less sensitivity to stray fields. The SFPR matrix concept adds another lens, namely the relay solenoid, to this basic configuration as shown schematically in Figure 54.

Analytical expressions for the spot size as a function of geometric imaging and aberrations of the optics were developed for the basic column during the last quarter. The final spot size, d_i , for the two-lens collimating system is:

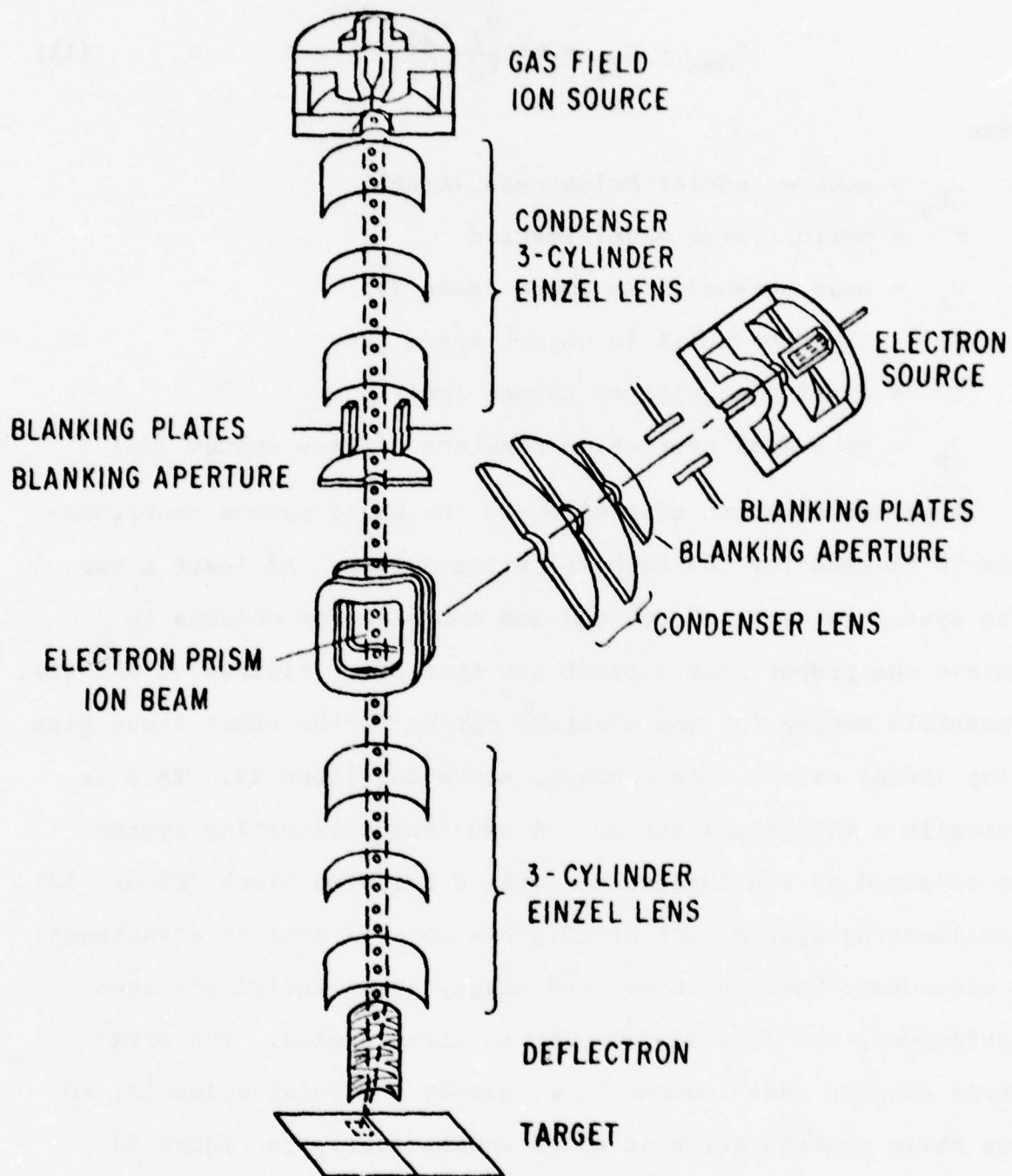


Figure 50. Focused Ion Optics

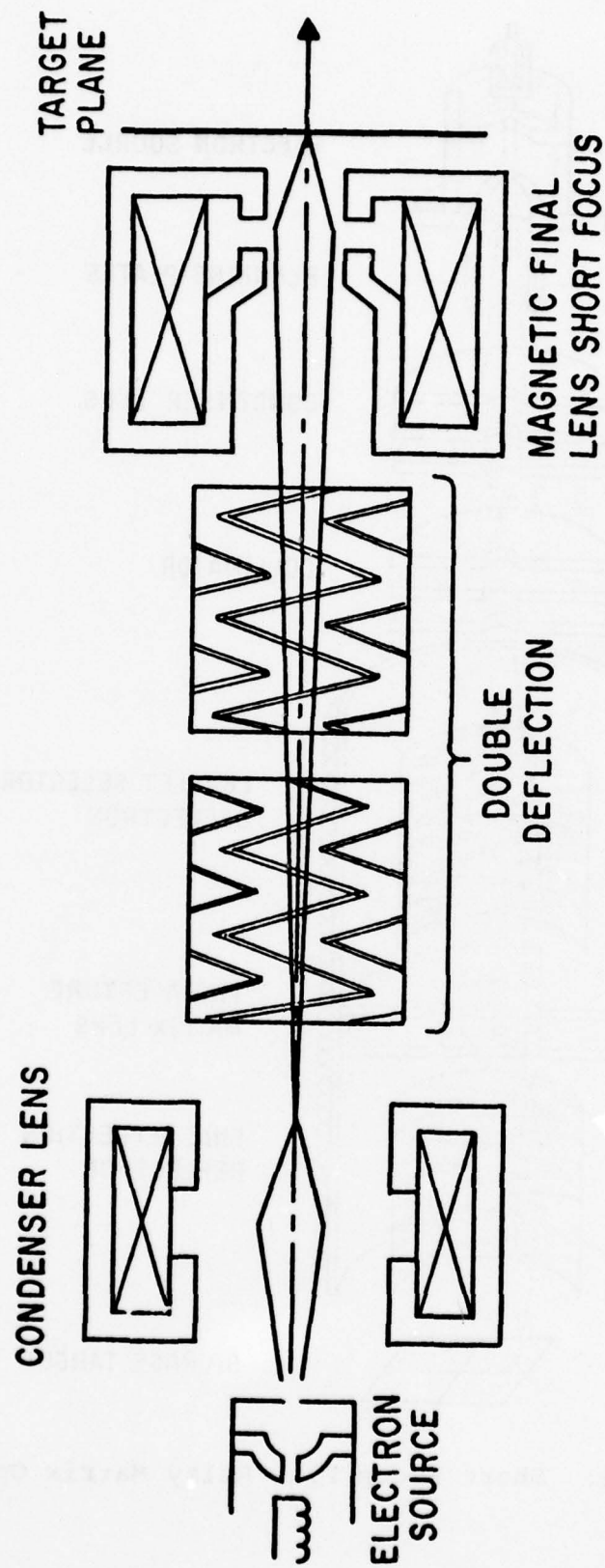


Figure 51. Two-Lens All Magnetic Optics

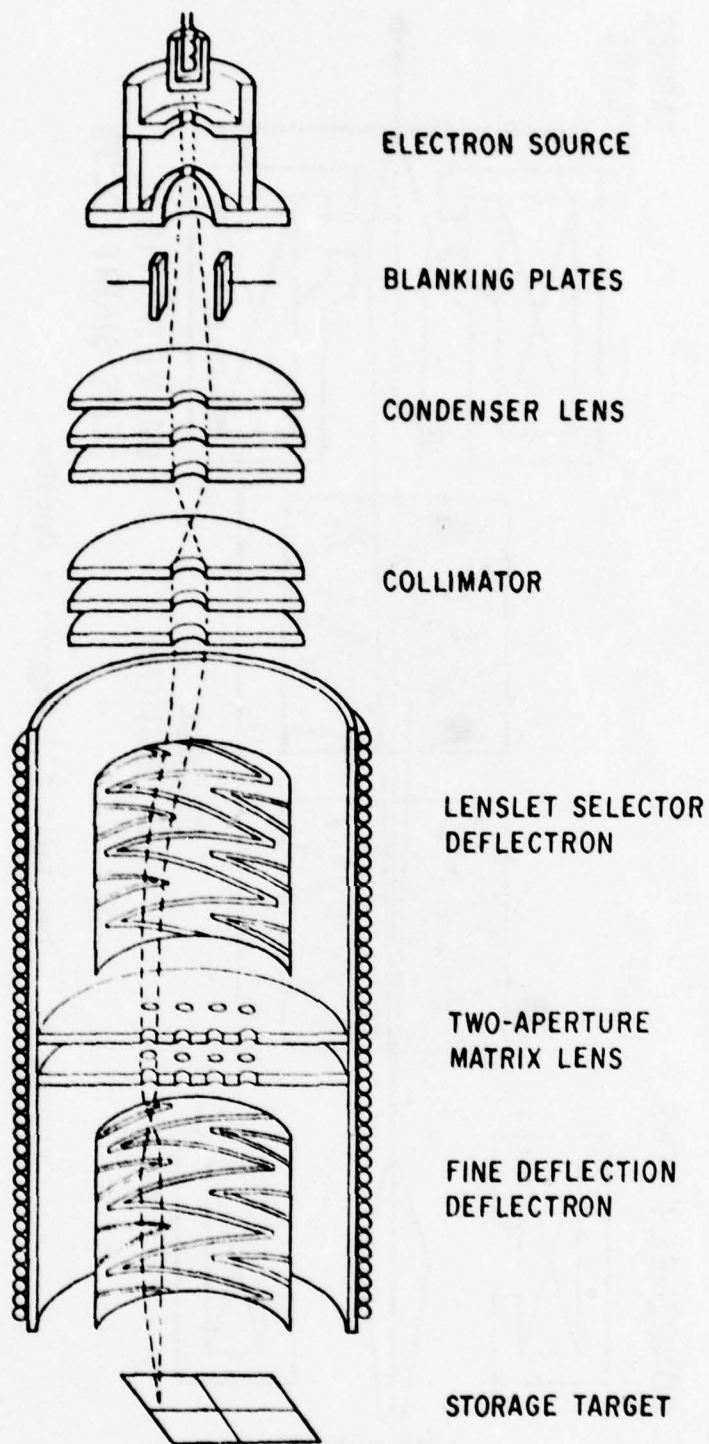


Figure 52. Short Focus Plus Relay Matrix Optics

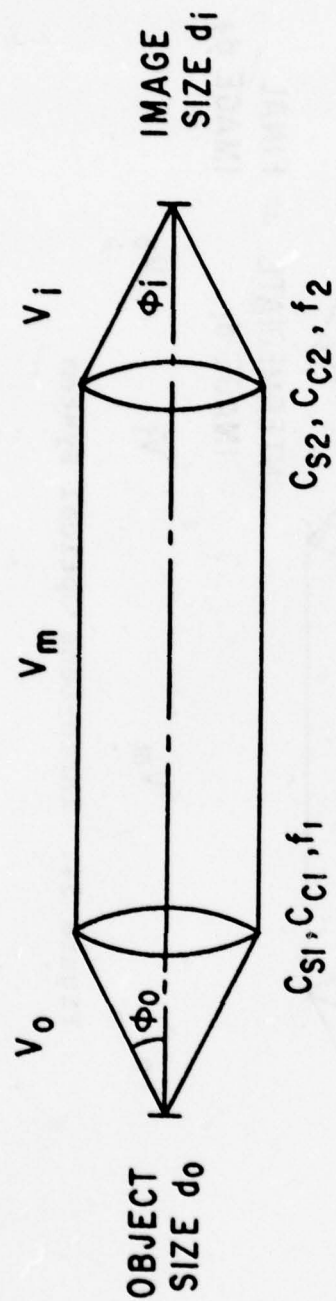


Figure 53. Two-Lens Collimating Optical System

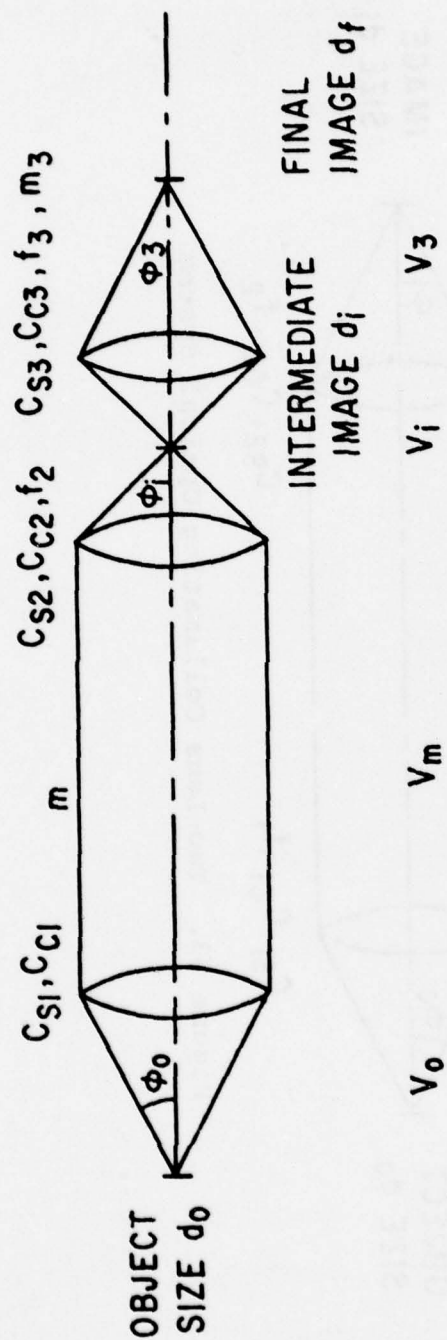


Figure 54. Three-Lens Optical System

$$d_i = \left[m^2 d_o^2 + \frac{1}{4} \left\{ m^8 C_{s1}^2 \left(\frac{V_i}{V_o} \right)^3 + C_{s2}^2 \right\} \phi_i^6 + 4 \left\{ m^4 C_{c1}^2 \frac{\Delta V^2 V_i}{V_o^3} + C_{c2}^2 \left(\frac{\Delta V}{V_i} \right)^2 \right\} \phi_i^2 + \left(\frac{0.61 \lambda_i}{\phi_i} \right)^2 \right]^{1/2} \quad (12)$$

where

m = linear magnification

d_o = source size

C_{s1}, C_{s2} = spherical aberration constants of first and second lenses, respectively

C_{c1}, C_{c2} = chromatic aberration constants of first and second lenses, respectively

ΔV = energy spread of beam

V_i = image space beam potential

V_o = object space beam potential

λ_i = charged particle wavelength

ϕ_i = beam half-angle at the image

With the added relay lens for the SFPR concept the final spot size, d_f , is:

$$d_f = \sqrt{d_i^2 + \frac{1}{4} C_{SR}^2 \phi_i^6 + 4 C_{CR}^2 \phi_i^2 \left(\frac{\Delta V}{V_i} \right)^2} \quad (13)$$

where C_{SR} and C_{CR} are the spherical and chromatic aberration constants of the relay lens.

During the third quarter, several programs used to calculate the optical properties of various electron lenses were reestablished on the time sharing computer network. Aberration properties for various electrostatic lenses that occupy the same space were investigated. The spherical aberration results for these

lenses are shown in Figure 55. Similar data for symmetrical magnetic lenses were also available.

SOURCE SELECTION

For both the electron and ion sources there are two fundamentally different source types. These are the extended object source corresponding to the Radley Pierce electron source and duoplasmatron ion source and the small source size or pointed cathodes represented by the TFE (thermally aided field emission) electron source and FI (field ionization) source. The useful spot size ranges for these sources can be estimated using Eqs. (10) and (11) and the data given in Tables 7 and 8.

C_s , as given in these equations, is the effective spherical aberration coefficient which can be determined from Eq. (12) as:

$$C_{se} = \sqrt{m^8 C_{s1}^2 \left(\frac{V_i}{V_o}\right)^3 + C_{s2}^2} \quad (14)$$

This equation illustrates a very important difference in the imaging properties of magnifying and demagnifying optical systems. In a magnifying system ($m \gg 1$), the spherical aberration of the first lens dominates, whereas in a demagnifying system ($m \ll 1$), the final lens spherical aberration is predominant. For magnifications near unity, the aberrations of the lenses are comparable.

Substituting Eq. (14) into Eq. (10), the maximum current for conventional sources is:

$$I_{\max} = \frac{3\pi^2}{16} \beta_i \frac{d^{8/3}}{\left(m^8 C_{s1}^2 \left(\frac{V_i}{V_o}\right)^3 + C_{s2}^2\right)^{1/3}} \quad (15)$$

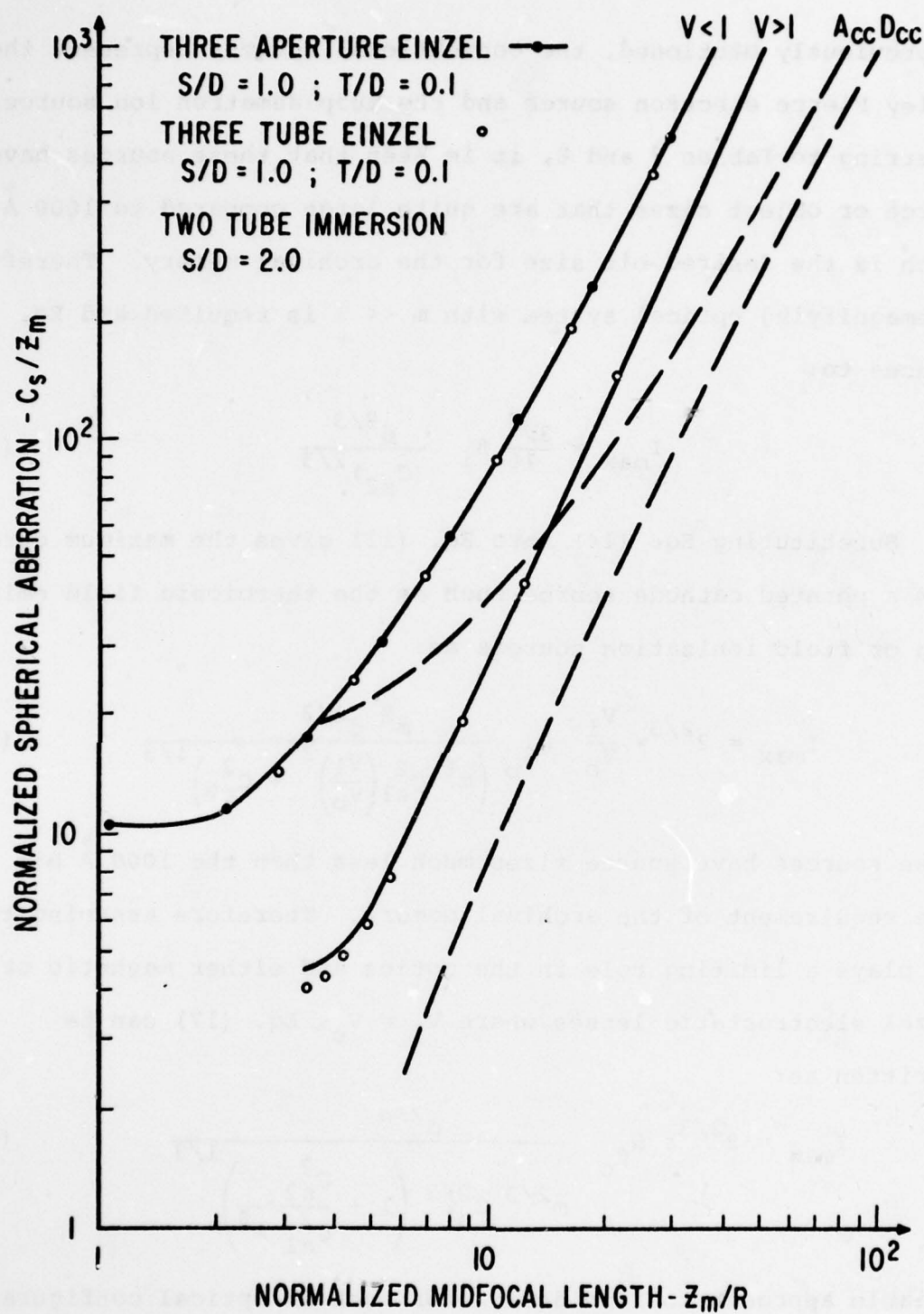


Figure 55. Electrostatic Lens Characteristics

As previously mentioned, the conventional sources represent the Radley Pierce electron source and the duoplasmatron ion source. Referring to Tables 7 and 8, it is seen that these sources have source or object sizes that are quite large compared to 1000 \AA which is the desired bit size for the archival memory. Therefore a demagnifying optical system with $m \ll 1$ is required and Eq. (15) reduces to:

$$I_{\max} = \frac{3\pi^2}{16} \beta_i \frac{d^{8/3}}{(C_{s2})^{2/3}} \quad (16)$$

Substituting Eq. (14) into Eq. (11) gives the maximum current from a pointed cathode source such as the thermionic field emission or field ionization sources as:

$$I_{\max} = 2^{2/3} \pi \frac{V_i}{V_o} \Omega_{\beta_o} \frac{m^2 d^{2/3}}{\left(m^8 C_{s1}^2 \left(\frac{V_i}{V_o} \right)^2 + C_{s2}^2 \right)^{1/3}} \quad (17)$$

These sources have source sizes much less than the 1000 \AA bit size requirement of the archival memory. Therefore assuming that C_{s1} plays a limiting role in the optics and either magnetic or einzel electrostatic lenses where $V_i = V_o$, Eq. (17) can be rewritten as:

$$I_{\max} = 2^{2/3} \pi \Omega_{\beta_o} \frac{d^{2/3}}{m^{2/3} C_{s1}^{2/3} \left(1 + \frac{C_{s2}^2}{C_{s1}^2 m^8} \right)^{1/3}} \quad (18)$$

A viable approach to lens design for such an optical configuration would be to minimize C_{s1} and simply scale the first lens dimensions up to achieve the proper magnification. Under these conditions, $C_{s2}/C_{s1} = m$ and Eq. (18) becomes:

$$I_{\max} = 2^{2/3} \pi \Omega_{\beta_0} \frac{d^{2/3}}{C_{s1}^{2/3}} \frac{m^{4/3}}{(m^6 + 1)^{1/3}} \quad (19)$$

Differentiating I_{\max} with respect to m and setting the result equal to zero results in an optimum value of $m = 1.12$ for maximum current. At this magnification, I_{\max} is given by:

$$I_{\max} = 4.04 \Omega_{\beta_0} \frac{d^{2/3}}{C_{s1}^{2/3}} \quad (20)$$

Using Eqs. (16) and (20), the crossover spot size, where the beam currents achievable from conventional and pointed cathodes are equal, can be determined. Setting Eqs. (16) and (20) equal, with the condition that the spherical aberration constants of the critical lenses can be equalized, gives the crossover point spot size as:

$$d = \sqrt{2.18 (\Omega_{\beta_0} / \beta_i)} \quad (21)$$

For the ion sources, $\Omega_{\beta_0} = 10^{-6}$ A/str, and the maximum β_i is 10^3 giving a crossover spot size of 4670 \AA . This means that for spot sizes greater than 4670 \AA , the duoplasmatron can deliver more current per spot than the gas field ionization source, whereas the converse is true for spot sizes less than 4670 \AA . For the electron sources, $\Omega_{\beta_0} = 10^{-3}$ A/str for the TFE, and the maximum β_i is 2×10^5 for a 10 A/cm^2 cathode at 10 kV . The resulting crossover spot size for these numbers is 9350 \AA . Again this means that the Radley Pierce source produces more current per spot for $d > 9350 \text{ \AA}$, whereas the TFE is capable of more current per spot for $d < 9350 \text{ \AA}$.

For the archival writer, the desired bit size is 1000 \AA . This implies focused ion and electron beam spot sizes in the range of 500 to 1000 \AA for the writer depending on the scattering of the beam in the target. Based on the preceding analysis, the field type sources have a clear advantage for the archival writer because of their increased current capabilities over this spot size range.

At present, gas phase field ion sources have only been developed for hydrogen, argon, and some of the other inert gases. For conventional III-V semiconductor dopants, the most developed and brightest ion source is the duoplasmatron. The liquid metal ion sources, such as Ga or Ga-In, are far too unstable and underdeveloped to be seriously considered for an ion writer at this time. Fortunately it was shown, during the first phase of this contract, that damage writing with inert gas ions was viable and also advantageous from a fluence requirement point of view. Therefore, the advantages of the gas phase field ionization source can be utilized in the writer.

At the beginning of the fourth quarter of this contract, neon was a particularly attractive candidate for ion writing, with argon and xenon also being good candidates. As a result of interactions with the Oregon Graduate Center, it was concluded that neon and argon were good from a source standpoint. However, there were practical problems that would have to be resolved in order to develop a good xenon ion source. The operating voltage is another factor in the choice of the ion source. A large

voltage range could be accommodated by properly designing the source. However, in building the column, lower voltages are easier to accommodate. From the curves of Figure 56, this makes neon even more attractive for the useful beam penetration range of 0.025 to 0.1 μ . Therefore, a gas phase field ionization source, using neon gas and operating over the 20 to 60 kV range, was chosen for further study.

The electron source was easier to select because here only the current capability of the source is important. Therefore the TFE source was selected based on the results of the current capability study described above. It has been shown [8] that there is little difference in the performance of the W100 built-up or Zr/H 100 cathodes.* It was also established that the source properties of Table 7 could be achieved over the required landing potential range of 2 to 4 kV as indicated by the range curves for pertinent materials in Figure 57. Therefore, a W100 built-up TFE source operating over the 2 to 4 kV landing potential range was selected for further optical studies.

ION OPTICS ANALYSIS

During this quarter, the analysis of the optics for an archival ion write station was performed. This column analysis uses tools and techniques developed during the third quarter of this contract and assumes the source configuration selected in the preceding section of this report, namely, neon gas field ionization with 20 to 60 kV landing potential. The analysis was aimed at producing the most current per spot for the column.

*This was also confirmed at the Oregon Graduate Center meeting this quarter.

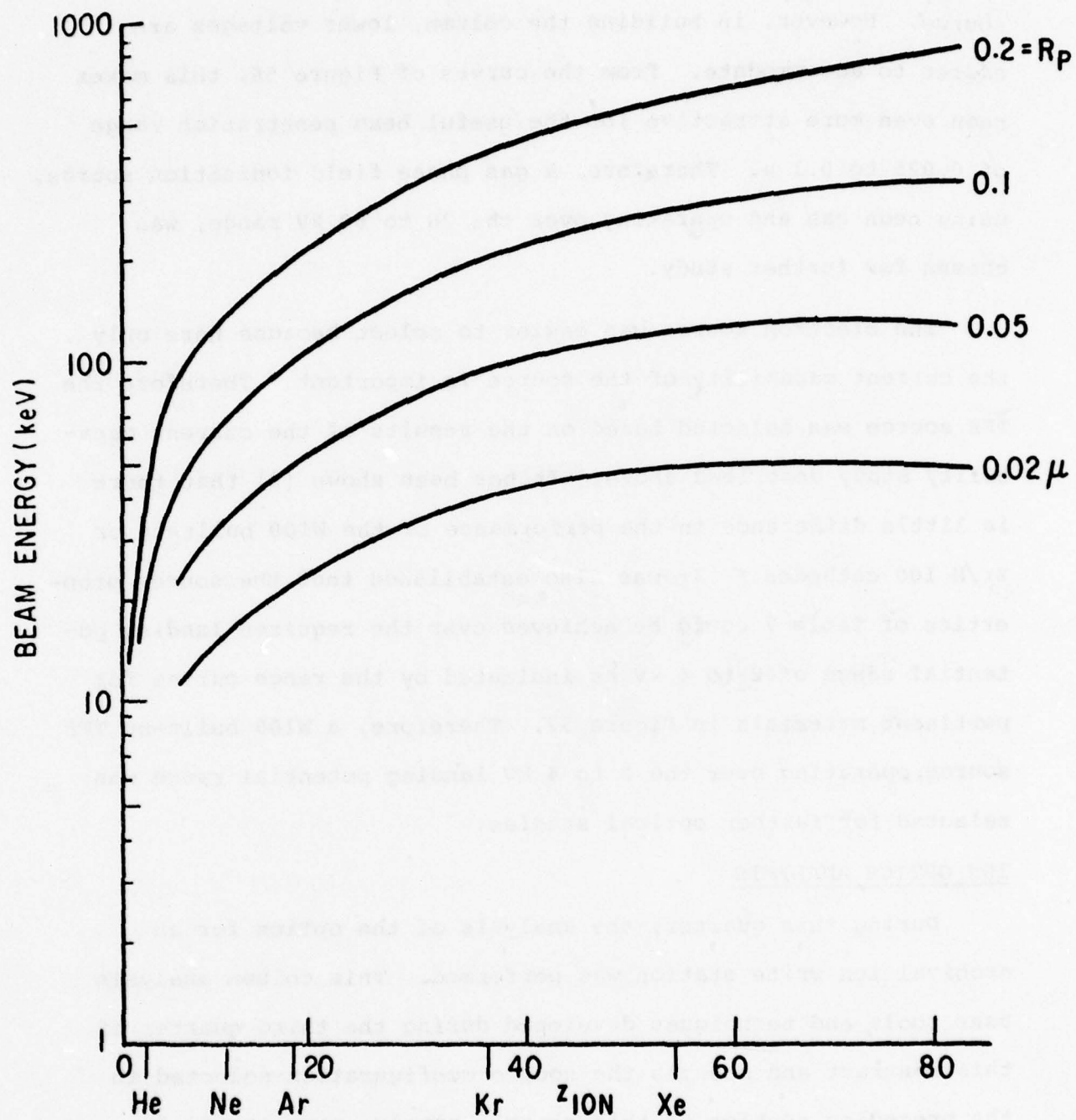


Figure 56. Ion Range Characteristics

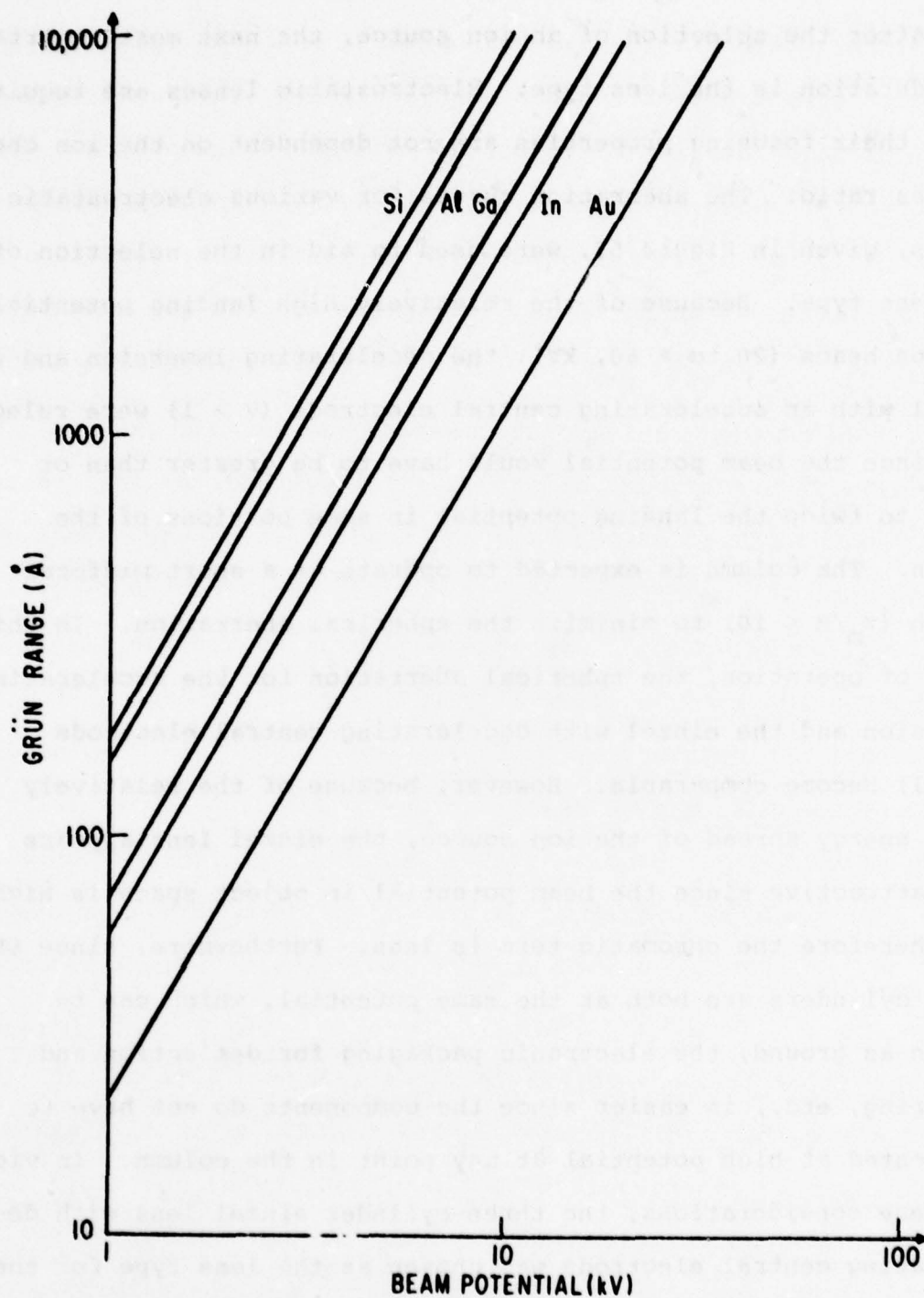


Figure 57. Grün Range vs Landing Potential for Several Materials

After the selection of an ion source, the next most important consideration is the lens type. Electrostatic lenses are required since their focusing properties are not dependent on the ion charge to mass ratio. The aberration curves for various electrostatic lenses, given in Figure 55, were used to aid in the selection of the lens type. Because of the relatively high landing potential for ion beams (20 to > 60 , kV), the decelerating immersion and the einzel with an accelerating central electrode ($V > 1$) were ruled out since the beam potential would have to be greater than or equal to twice the landing potential in some portions of the column. The column is expected to operate at a short midfocal length ($z_m/R \leq 10$) to minimize the spherical aberration. In this range of operation, the spherical aberration for the accelerating immersion and the einzel with decelerating central electrode ($V < 1$) become comparable. However, because of the relatively large energy spread of the ion source, the einzel lens appears more attractive since the beam potential in object space is higher, and therefore the chromatic term is less. Furthermore, since the outer cylinders are both at the same potential, which can be chosen as ground, the electronic packaging for deflection and centering, etc., is easier since the components do not have to be floated at high potential at any point in the column. In view of these considerations, the three-cylinder einzel lens with decelerating central electrode was chosen as the lens type for the ion optics.

Next, specific lens dimensions were determined to minimize aberrations. The cross section of a basic einzel lens is shown

in Figure 58. The optical properties for these lenses can be calculated in a general form by normalizing all lens dimensions with respect to the radius of the lens cylinders, R . Then, the only other variable is the dimensionless voltage ratio

$$V = \frac{V_0 - V_K}{V_1 - V_K} \quad (22)$$

where V_1 , V_0 are the lens potentials with respect to ground and V_K is the cathode potential with respect to ground. The focal and aberration properties normalized with respect to the lens radius are then a function of normalized lens dimensions and V . Using the definition of V given by Eq. (22), a relationship between the lens spacing, S , the landing potential, V_L , and the field strength, E_{gap} , between lens elements can be determined:

$$S = \frac{V_L (1 - V)}{|E_{\text{gap}}|} \quad (23)$$

For a particular operating point, V and V_L , the plate spacing, and hence all lens dimensions, are minimized by maximizing the gap field strength. Therefore, since the lens dimensions are minimized so are the aberrations.

Since the overall magnification $m \geq 1$, due to the field ion source, the aberrations of the first lens are expected to play a limiting role in the optics design [cf. Eq. (14)]. Therefore we consider the first lens and source configuration as shown in Figure 59. As noted on this figure, a typical FI tip to gun aperture distance is 2 mm. The lens field is known to disturb the lens potential for about 1 diameter of length in the outer

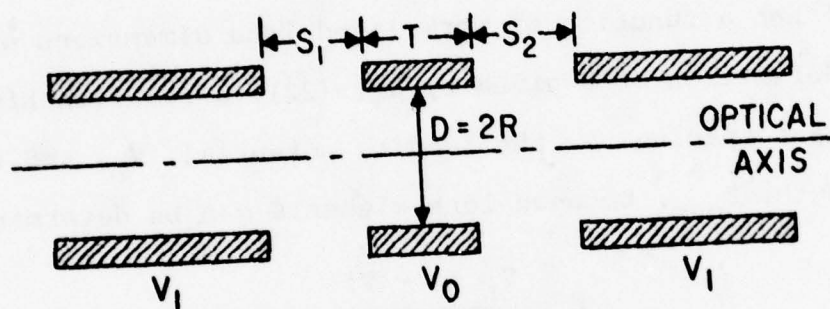
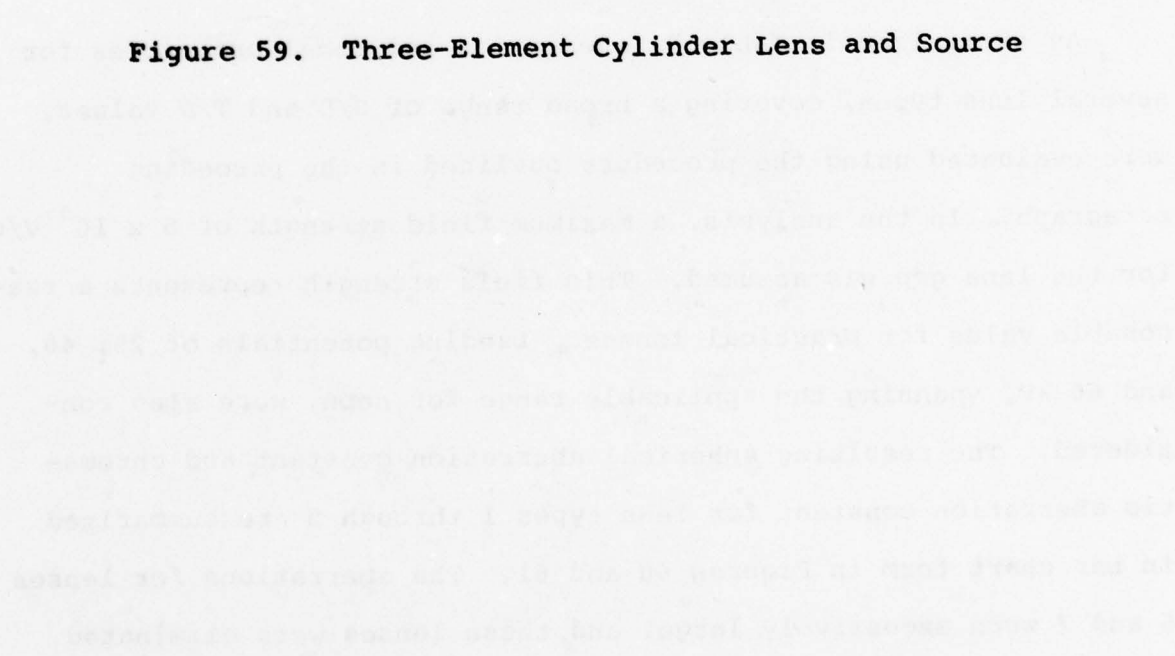


Figure 58. Three-Element Cylinder Lens



123

tube for typical lens types. Therefore, with reference to the figure, a value of $L_{\min}/R = 3.0$ was selected to accommodate the gun and not disturb the lens field. Assuming that the FI tip represents the virtual source location, a minimum midfocal distance for collimated operation is:

$$\frac{z_m}{R} \geq 3.0 + 2.0 \frac{S}{D} + \frac{T}{D} \quad (24)$$

The evaluation of einzel lenses starts by the selection of a specific lens (S/D, T/D) and evaluation of z_m/R with Eq. (24). This value of z_m/R is then used in conjunction with computer calculations of the lens properties to determine the voltage ratio V. Then using this value of V in Eq. (23) for a specific value of V_L and E_{gap} , the lens plate spacing, S, can be calculated. Once S is known, D and R are known for that lens type, and the actual optical properties can be determined from the calculated lens data in normalized form.

As summarized in Table 9, aberration and focal properties for several lens types, covering a broad range of S/D and T/D values, were evaluated using the procedure outlined in the preceding paragraph. In the analysis, a maximum field strength of 5×10^4 V/cm for the lens gap was assumed. This field strength represents a reasonable value for practical lenses. Landing potentials of 25, 40, and 60 kV, spanning the applicable range for neon, were also considered. The resulting spherical aberration constant and chromatic aberration constant for lens types 1 through 5 are summarized in bar chart form in Figures 60 and 61. The aberrations for lenses 6 and 7 were excessively large, and these lenses were eliminated.

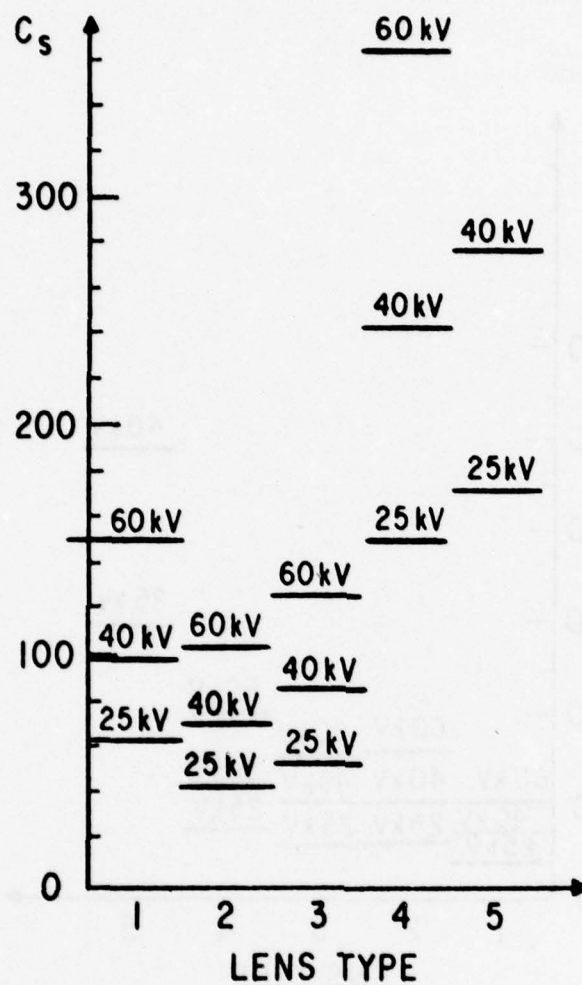


Figure 60. Spherical Aberration Constants for Lens Types 1 to 5

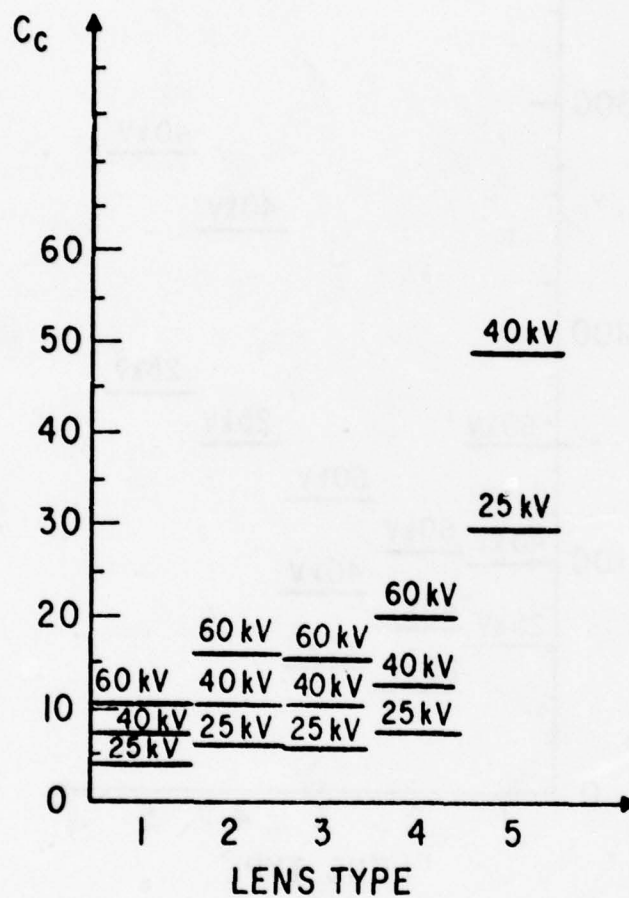


Figure 61. Chromatic Aberration Constants for Lens Types 1 to 5

TABLE 9
EINZEL LENS CASES

Lens #	1	2	3	4	5	6	7
S/D	1	0.5	0.5	0.5	0.1	0.1	0.1
T/D	0.1	1.0	0.5	0.1	2.0	1.0	0.1

The large aberration coefficients arise because of the large lens diameters resulting from the gap, S, required to support the field, and the low S/D ratio.

From Figures 60 and 61, lens #2 has the lowest spherical aberration, whereas lens #1 has the lowest chromatic aberration for a given landing potential. Since the column may be operating in a regime for which both the spherical and chromatic aberrations are important, both lenses have been considered in further studies. Dimensions and optical properties for lenses 1 and 2 are summarized in Table 10.

TABLE 10
PROPERTIES OF LENSES 1 AND 2

Lens Parameter	Lens #1			Lens #2		
	25 kV	40 kV	60 kV	25 kV	40 kV	60 kV
S-Lens Spacing	0.4 cm	0.64 cm	0.96 cm	0.35 cm	0.56 cm	0.84 cm
R-Lens Radius	0.2 cm	0.32 cm	0.48 cm	0.35 cm	0.56 cm	0.84 cm
f-Focal Length	1.40 cm	2.23 cm	3.35 cm	2.05 cm	3.28 cm	4.92 cm
z_m -Midfocal Length	1.37 cm	2.20 cm	3.30 cm	1.98 cm	3.17 cm	4.75 cm
C_s -Spherical Aberration	61.86 cm	98.97 cm	148.46 cm	42.56 cm	68.10 cm	102.15 cm
C_c -Chromatic Aberration Constant	4.56 cm	7.30 cm	10.95 cm	6.67 cm	10.67 cm	16.01 cm

Beam Deflection

As previously noted, the ion column is expected to operate with an overall magnification near unity. Therefore, the focal length and aberrations of the final lens will be quite similar to those of the first lens. If pre-lens deflection is used, the off-axis aberrations of the final lens add to the deflection aberrations. If post-lens deflection is used, the lens must have a long enough midfocal length to accommodate the deflector. Post-lens deflection is desirable since it is simpler, has lower deflection aberrations than pre-lens deflection [9], and requires less drive voltage.

As a first step in the ion column analysis, beam current vs spot size for a two-lens column was calculated for lens #1 and lens #2. Magnifications ranging from 1/2 to 4 and landing potentials of 25, 40 and 60 kV were used in the analysis. Results of these calculations at 25 kV are shown in Figure 62. Note that magnification of unity in these calculations gave the maximum current for both lens types. For spot sizes greater than $\approx 1000 \text{ \AA}$ (where spherical aberration is dominant) lens #2 gave the most current, whereas lens #1 gave the most current for spot sizes less than 1000 \AA (where chromatic aberration is dominant). Similar results were obtained at 40 and 60 kV.

Since $m = 1$ gave the maximum current conditions, the deflection voltage was calculated for these cases. A simple parallel plate deflector (post-lens) as shown in Figure 63 was assumed, giving the plate-to-plate drive voltage:

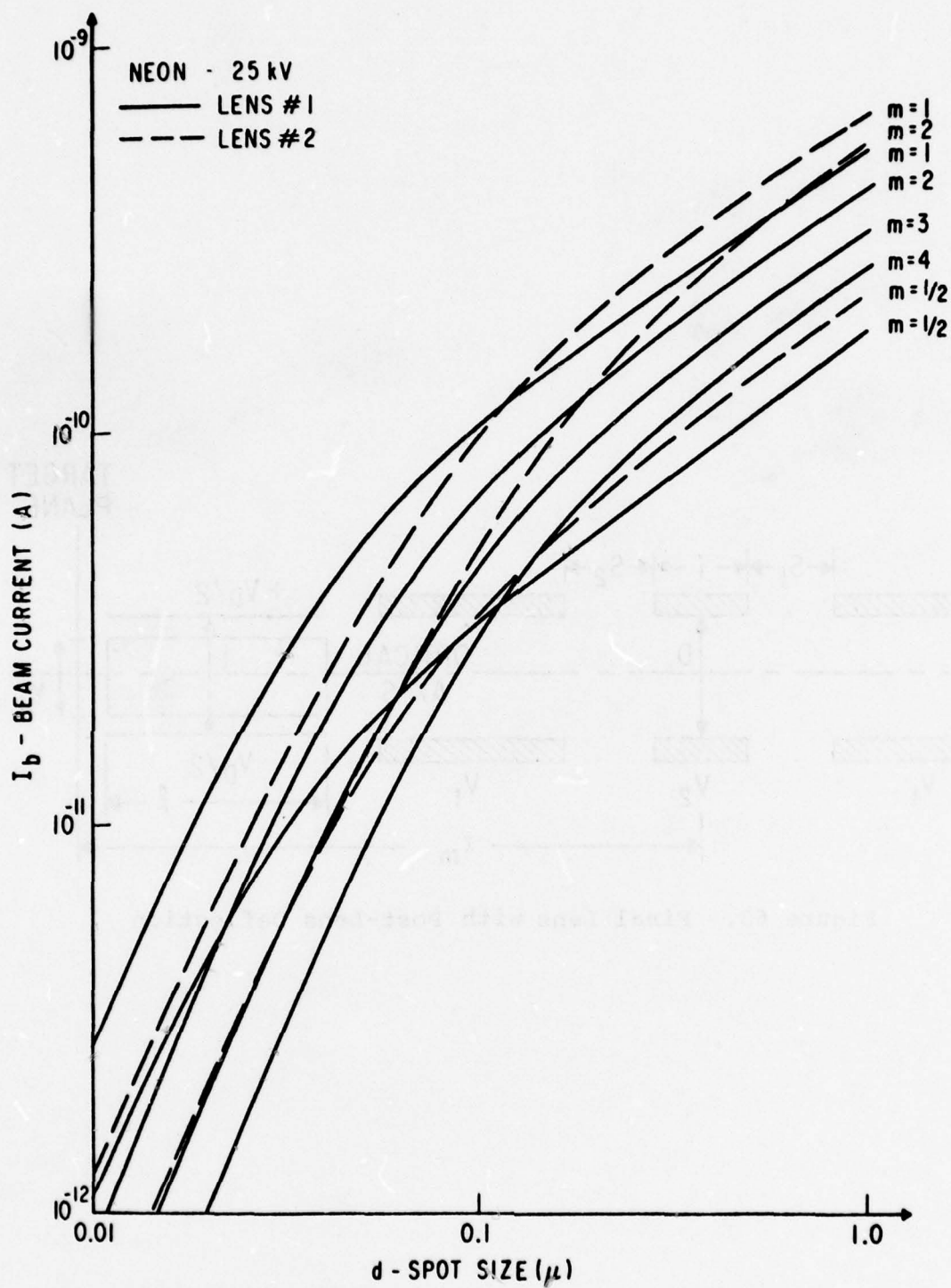


Figure 62. Beam Current vs Spot Size for Focused Ion Optics at Various Magnifications

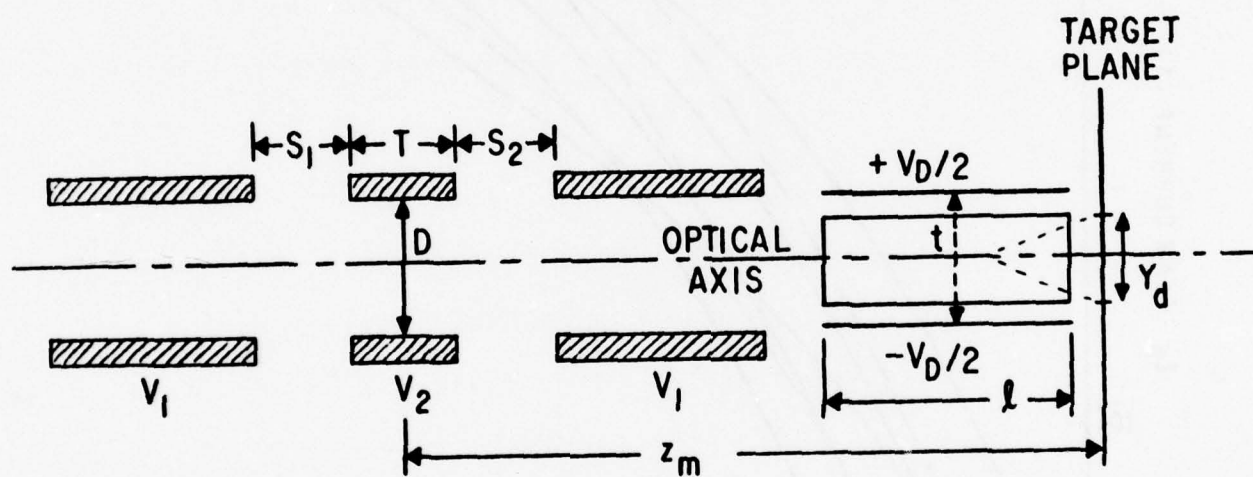


Figure 63. Final Lens with Post-Lens Deflection

$$V_D = \frac{2Y_d V t}{l^2} \quad (25)$$

where

Y_d = the deflection field length

V = beam potential

t = plate spacing

l = plate length.

A plate spacing of 6 mm and deflection field of 1 mm (10^8 bits for 1000 Å spot) were used. The plate length l was determined from the lens data of Table 10 and the equation:

$$l = z_m - T/2 - S - 2R \quad (26)$$

These calculations show that the required deflection voltage would be much greater than 1000 V peak per plate at $m = 1$. Therefore a compromise in beam current (i.e., magnification) would be required for a practical deflection system.

It was then assumed that 500 V peak per plate was a reasonable deflection voltage. Using this value and the previous deflector parameters, Eq. (25) was rearranged and solved for l . This value of l was then used with a rearranged form of Eq. (26) to solve for the minimum z_m . The final lens was then scaled in dimension to achieve this midfocal length and the magnification recalculated for columns based on lenses 1 and 2. Values of minimum lens radius and magnification for 500 V deflection drive per plate are summarized in Table 11. Beam current vs spot size calculations were made for columns using lenses 1 and 2 with the final lens scaled in dimensions to achieve the 500 V peak deflection requirement. Curves resulting from these calculations are

TABLE 11
PARAMETERS AT 500 V PEAK DEFLECTION

Landing Potential (kV)	Lens #1		Lens #2	
	Magnification	Radius	Magnification	Radius
25	1.85	0.37	1.47	0.61
40	1.63	0.52	1.58	0.88
60	1.43	0.68	1.45	1.22

given in Figures 64 and 65. A comparison of these curves shows that the column using lens type 1 achieves more current per spot for spot sizes less than 1000 Å.

Therefore as a final column, lens #1 operating with a scaled-up final lens to keep deflection drive voltage at 500 V peak per plate was selected. The landing potential was chosen as 40 kV which represents an approximately 500 Å penetration for neon ions. For this column configuration, geometric deflection aberrations were calculated assuming previously developed equations for parallel plate deflectors [10]. The geometric deflection aberrations as a function of field size are shown in Figure 66. As seen from this figure, uncompensated aberrations limit the field size to approximately 10^7 bits. Distortion (which represents the largest aberration) can be completely corrected by nonlinear deflection drive. However, the degree of correction that can be implemented for the other aberration terms is not now known. A fundamental uncorrectable aberration for the deflection is chromatic aberration as given by:

$$\delta_c = \frac{y_d}{2} \frac{\Delta V}{V} \quad (27)$$

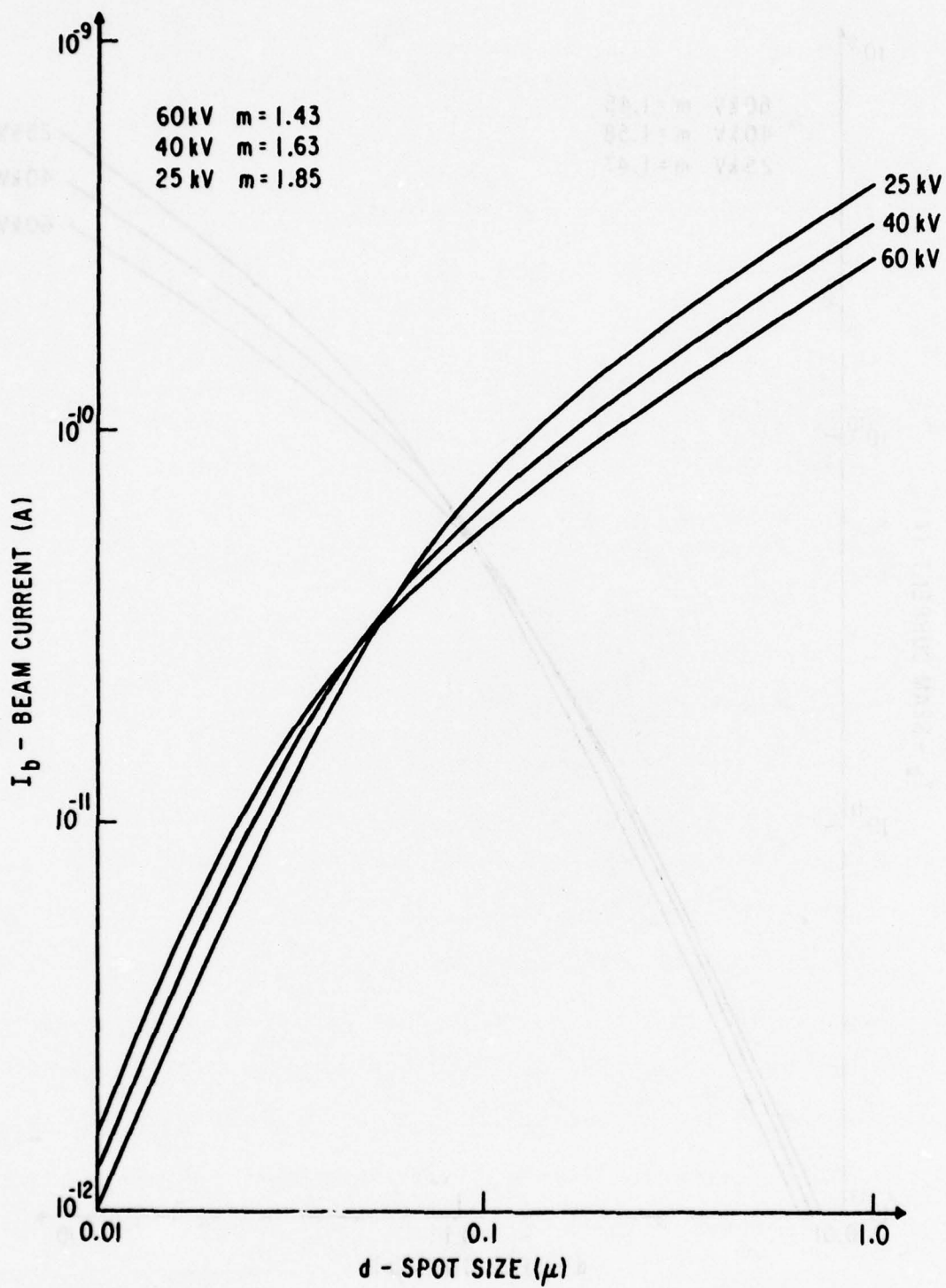


Figure 64. Beam Current vs Spot Size for Deflection Limit on Magnification with Lens #1

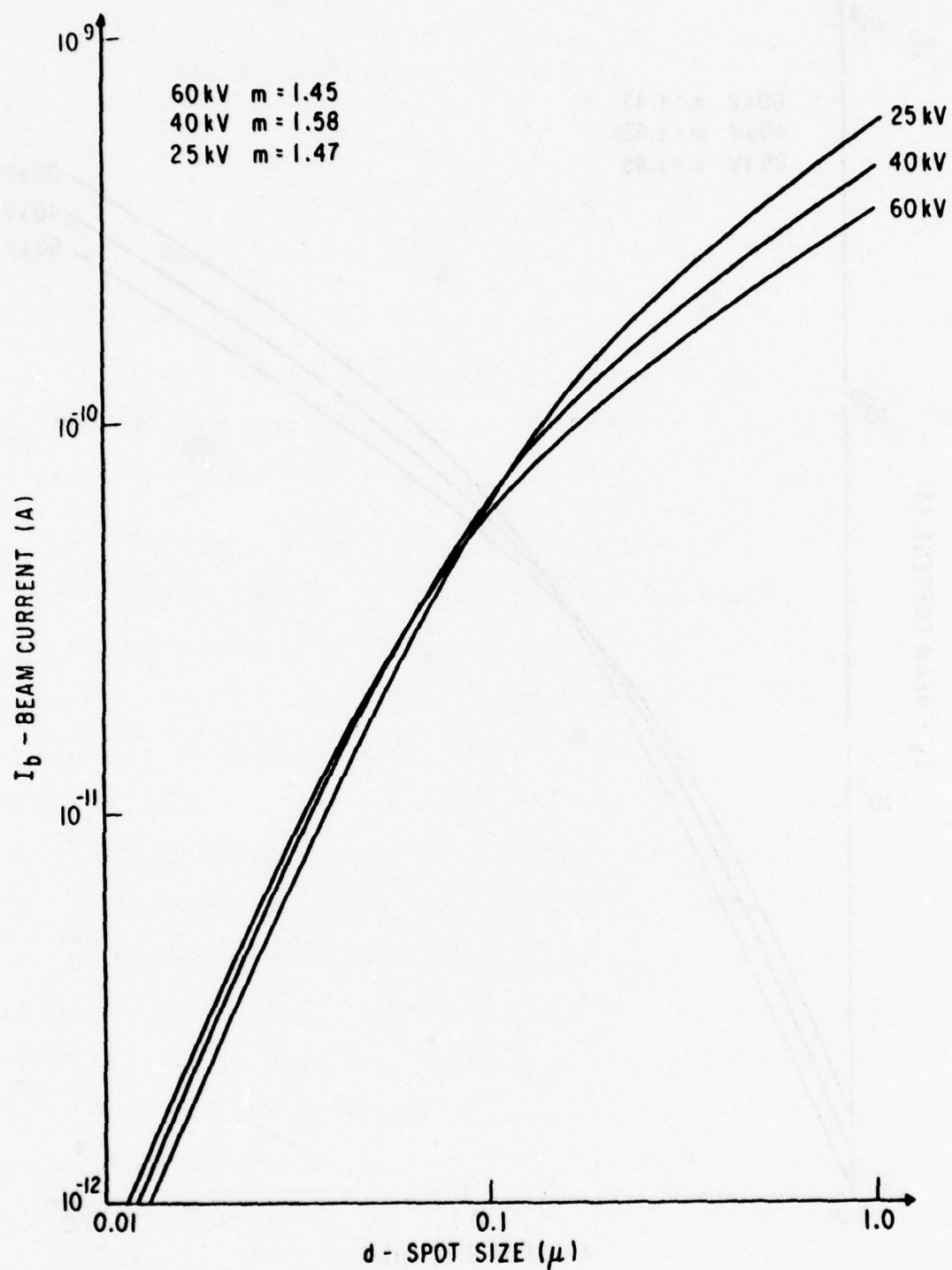


Figure 65. Beam Current vs Spot Size for Deflection Limit on Magnification with Lens #2

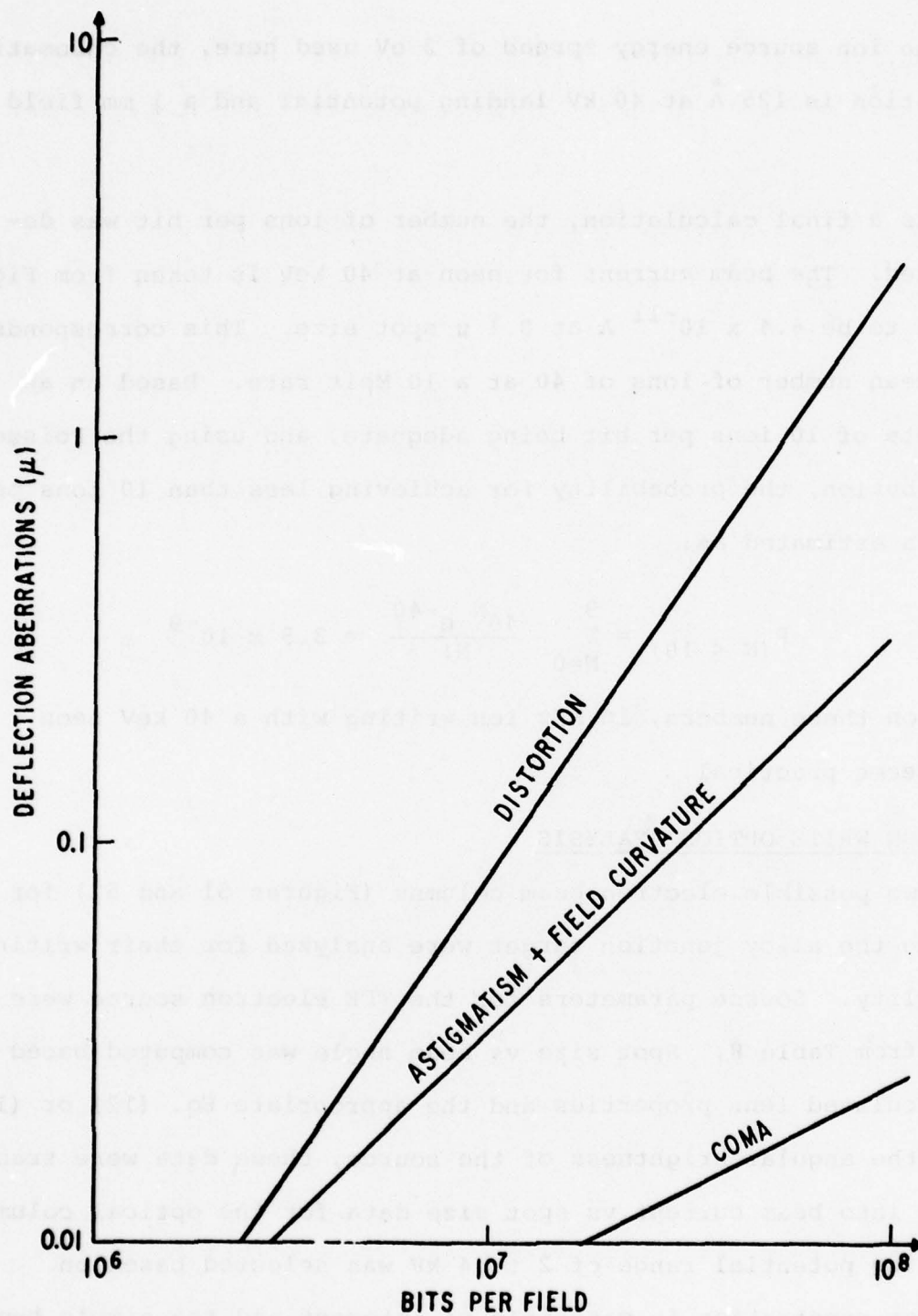


Figure 66. Deflection Aberrations for Ion Optics - 40 kV Neon

For the ion source energy spread of 2 eV used here, the chromatic aberration is 125 \AA at 40 kV landing potential and a 1 mm field size.

As a final calculation, the number of ions per bit was determined. The beam current for neon at 40 keV is taken from Figure 64 to be $6.4 \times 10^{-11} \text{ A}$ at $0.1 \text{ }\mu$ spot size. This corresponds to a mean number of ions of 40 at a 10 Mbit rate. Based on an estimate of 10 ions per bit being adequate, and using the Poisson distribution, the probability for achieving less than 10 ions per bit was estimated as:

$$P(N < 10) = \sum_{N=0}^9 \frac{40^N e^{-40}}{N!} = 3.9 \times 10^{-9}$$

Based on these numbers, 10 MHz ion writing with a 40 keV neon beam seems practical.

ELECTRON WRITE OPTICS ANALYSIS

Two possible electron beam columns (Figures 51 and 52) for writing the alloy junction target were analyzed for their writing capability. Source parameters for the TFE electron source were taken from Table 8. Spot size vs beam angle was computed based on calculated lens properties and the appropriate Eq. (12) or (13). Using the angular brightness of the source, these data were transformed into beam current vs spot size data for the optical column. A landing potential range of 2 to 4 kV was selected based on electron penetration in materials of interest and the simple hemispherical beam heating model used previously [11].

The first column considered is the two-magnetic lens column of Figure 51. In previous work at the General Electric Research

and Development Center, a high quality magnetic condenser lens TFE combination had been designed, built, and tested. The lens that evolved from this work is shown in Figure 67. The lens/TFE combination operated and was optimized for a 10 kV gun with a 0.675 inch gun O.D. For the present design we are interested in a 2 to 4 kV design with a minimum lens I.D. of 1.0 inch. The difference in these requirements is enough to prohibit the use of the previous design, although the knowledge and experience gained on the preceding lens is directly applicable to the present design.

A generalized schematic of a magnetic lens is shown in Figure 68. In the preceding condenser design it was shown:

- $S/D > 0.3$ lenses were too cumbersome.
- Symmetrical lenses with $D_1 = D_2 = D$ have aberration properties as good or better for an over-the-gun condenser.
- Increasing magnetic fields in the iron circuit $> 1W/m^2$ did not reduce optical properties substantially, but do present a threat of deleterious pole piece saturation.

In view of these considerations, a magnetic condenser lens with $S/D = 0.2$ and a $1W/m^2$ pole piece field was assumed. Focal properties, spherical aberration, and chromatic aberration were taken from published computer calculations [12] and are shown graphically in Figures 69, 70, and 71. In these figures the optical properties normalized with respect to lens radius are given in terms of the lens drive parameter

$$k^2 = \beta \frac{(NI)^2}{V} = 0.0087 \left(\frac{B_O}{B_P} \right)^2 \left(\frac{D}{S} \right)^2 \frac{(NI)^2}{V} \quad (28)$$

Figure 67. Low Spherical Aberration
Magnetic Lens

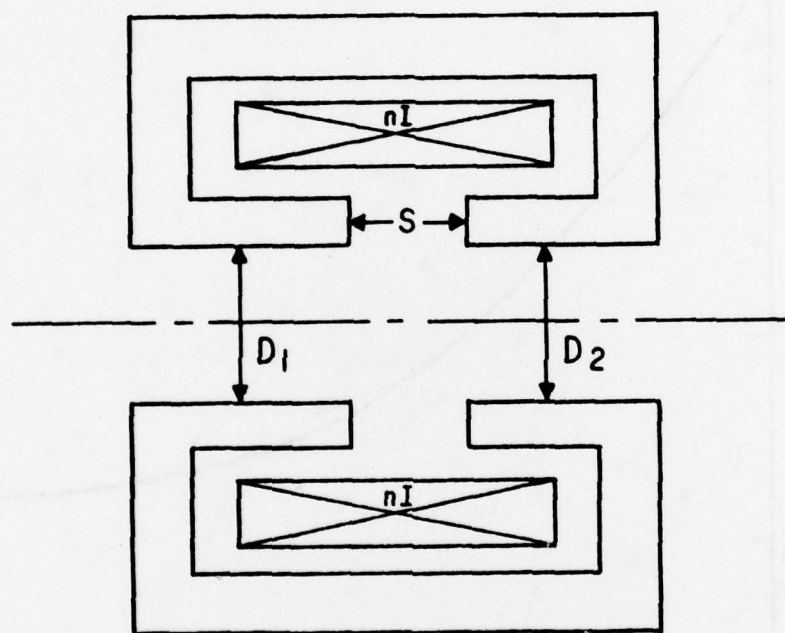


Figure 68. General Schematic for a Magnetic Lens

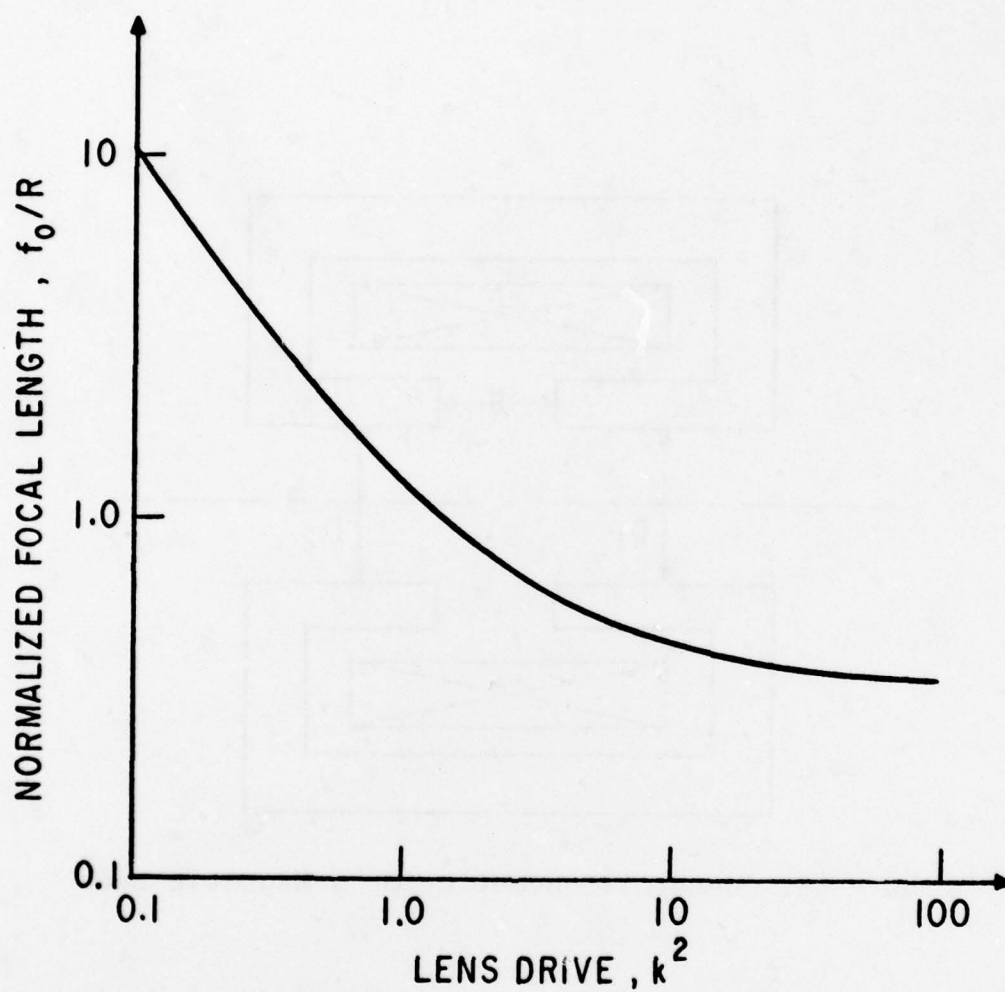


Figure 69. Magnetic Lens Data - Normalized Focal Length, f_0/R , vs Lens Drive, k^2 , for $S/D = 0.2$

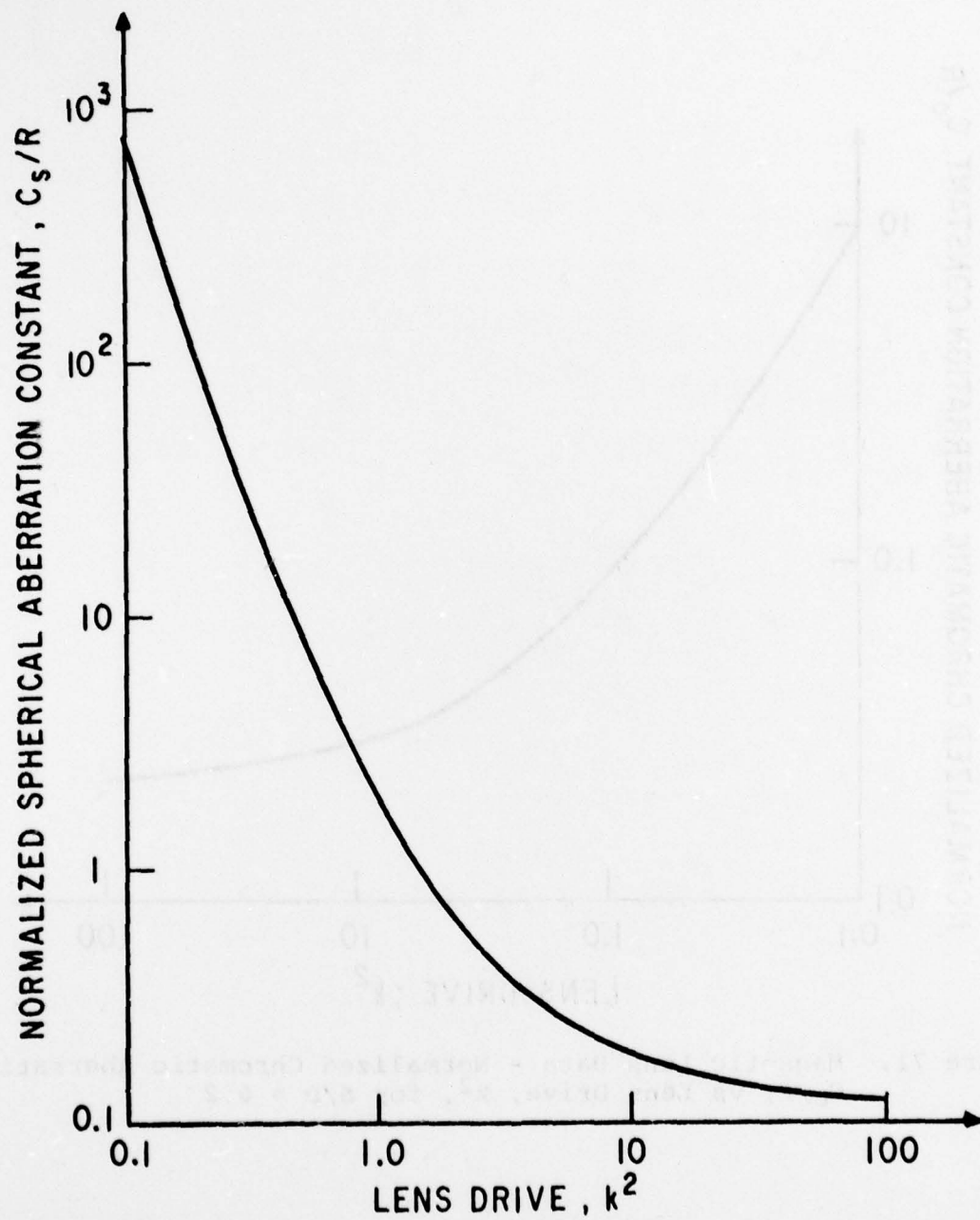


Figure 70. Magnetic Lens Data - Normalized Spherical Aberration Constant, C_s/R , vs Lens Drive, k^2 , for $S/D = 0.2$

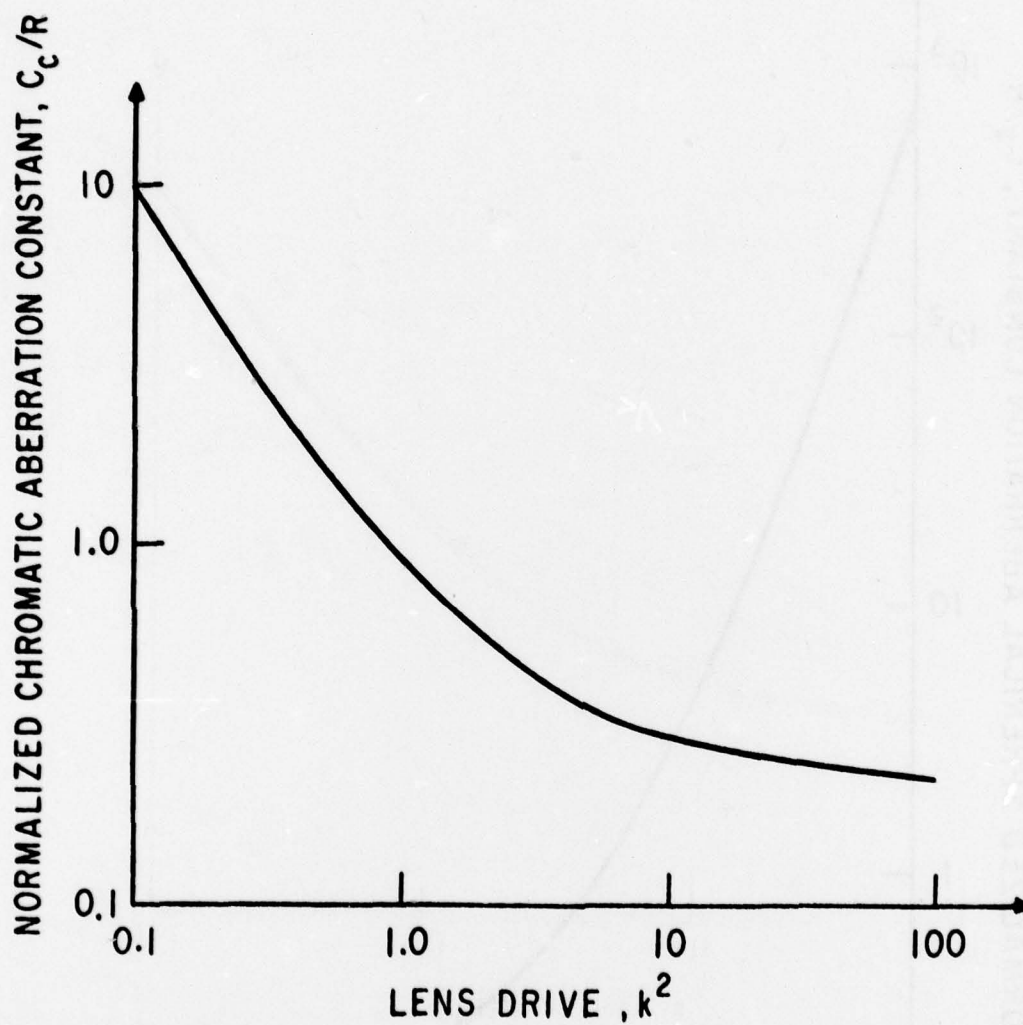


Figure 71. Magnetic Lens Data - Normalized Chromatic Aberration, C_c/R , vs Lens Drive, k^2 , for $S/D = 0.2$

where

B_o = peak on axis field

B_p = magnetic field in lens gap

D = lens diameter

S = lens gap spacing

NI = ampere turns

V = beam potential

Test calculations for the lens were made assuming a 2 inch I.D., $S/D = 0.2$ lens with a $1W/m^2$ field strength in the lens gap. For these conditions it was found that $k^2 = 238$, which is well above the level-off point in C_s vs k^2 as can be seen from Figure 70.

Therefore, a new condenser operating point of $k^2 = 70$, corresponding to the level-off point of C_s , was selected. Operation at this point reduces lens drive requirements and guarantees a gap field strength of less than $1W/m^2$ for all condenser lenses with $D \leq 2.0$ inches and $V < 4$ kV.

Various final lenses were considered with reduced lens drive, k^2 , and various lens diameters, D . The lens diameter was kept > 180 mils for fabrication purposes, and the lens center-to-target distance was kept large enough to accommodate the target.

Calculations of beam current and spot size were made for various condenser and final lens combinations. It was found that the maximum current per spot was obtained with a 1 inch I.D. condenser lens and a 0.25 inch I.D. final lens. Condenser lens and object lens data are summarized in Table 12. Beam current vs spot size calculations for this lens system are shown in Figure 72 for a landing potential range of 2 to 4 kV. Note that at a spot

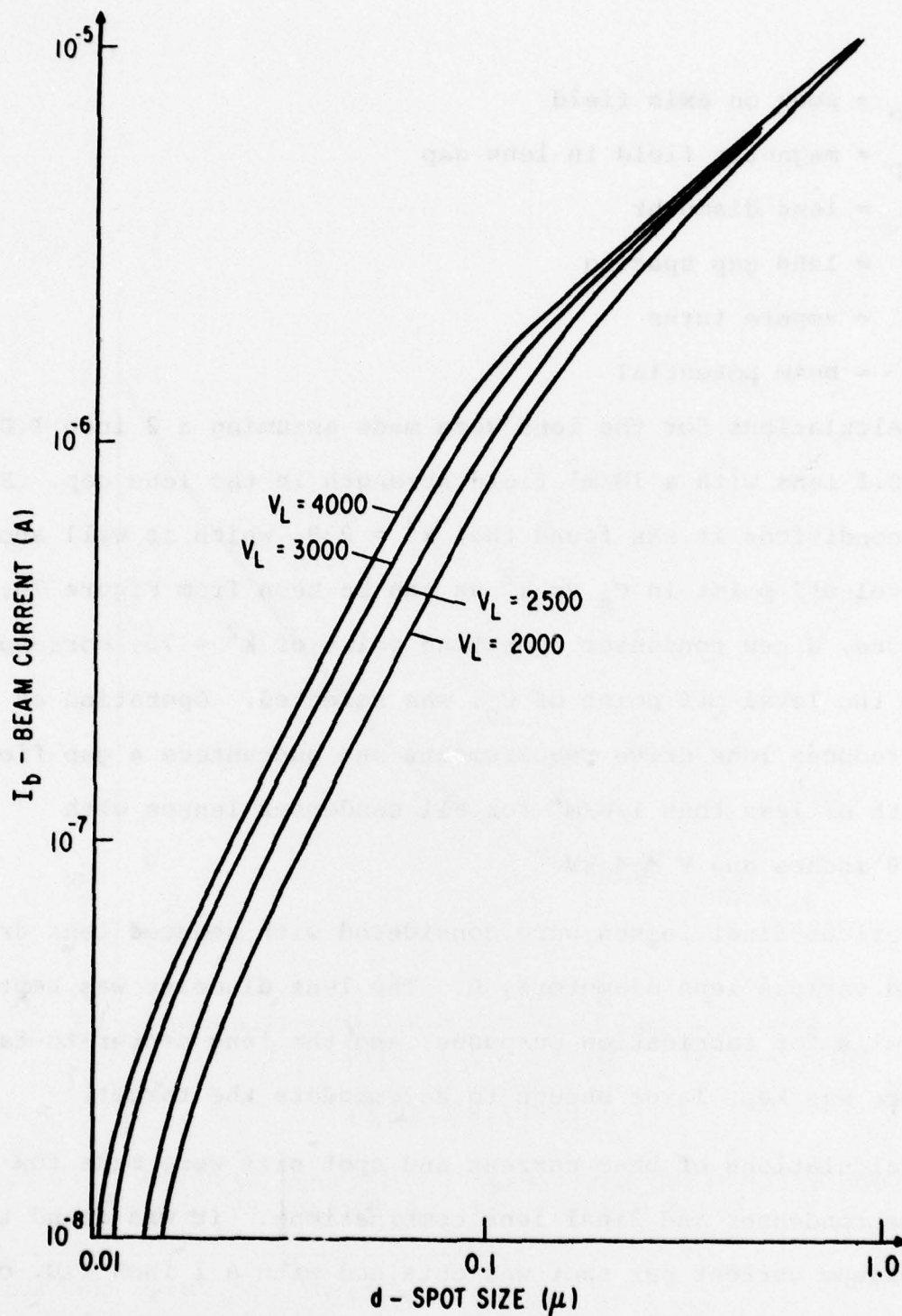


Figure 72. Beam Current vs Spot Size for a Two-Magnetic-Lens Column at Various Landing Potentials - V_L

TABLE 12
MAGNETIC LENS PROPERTIES
FOR MAXIMUM CURRENT COLUMN

lens	k ²	S (inch)	D (inch)	f _o (cm)	C _s (cm)	C _c (cm)
condenser	70	0.2	1	0.47	0.1524	0.292
objective	0.7	0.05	0.25	0.53	1.33	0.460

size of 1000 Å the beam current is typically on the order of 1 μA. At these low landing potentials and high beam currents, the question of space charge spreading of the beam must be investigated. The current at which space charge effects become important was estimated using the universal space charge curve [13]. Beam conditions and the space charge current for the column were checked. The results are summarized in Table 13. In all cases it is seen that the space charge current is well above the beam current. Therefore, space charge should not be a problem.

TABLE 13
RESULTS OF SPACE CHARGE EFFECTS

Beam Voltage	Spot Size (μ)	Half at Target (rad)	Beam Current (A)	Space Charge Current (A)
2500	0.029	4 x 10 ⁻³	6.4 x 10 ⁻⁸	12.5 x 10 ⁻⁶
2500	0.15	10 x 10 ⁻³	1.6 x 10 ⁻⁶	89 x 10 ⁻⁶
2500	1.5	50 x 10 ⁻³	14 x 10 ⁻⁶	3.6 x 10 ⁻³

As the next step in the electron column analysis, the beam current vs spot size for the short focus plus relay matrix lens was calculated. The matrix lens was operated in the decelerating immersion mode which has lower aberrations (cf. Figure 55). The

matrix lens was also operated with maximum field strength between lens plates to minimize the focal length and hence the aberrations. Based on a lenslet field size of 1.0 mm by 1.0 mm corresponding to 10^8 bits and using the 1 inch I.D. condenser and TFE source, various matrix lenses with S/D values ranging from 0.5 to 4.0 were considered. A matrix relay length of 3.0 inches was assumed to allow room for the fine deflection. At 4000 V the S/D = 2.0 matrix lens gave the greatest beam current per spot size, as shown in Figure 73. Note that this lens is operating at a magnification of 1.81, which is somewhat higher than the anticipated maximum value of 1.12. However, this optimum magnification could only be reached by increasing the field strength between lens plates to a value greater than 5×10^4 V/cm. At this time it does not seem wise to operate at higher field strengths. Comparing Figures 72 and 73, the two-lens magnetic column is seen to be capable of approximately a factor of 20 times the current output of the SFPR column at 4.0 kV.

The temperature rise of a local volume of the alloy junction target with these beams was estimated using the simple hemispherical model, in which the beam energy is assumed to be completely dissipated in a hemisphere of radius a . The radius a is determined by the electron scattering in the material and the beam spot size d , and is given approximately by:

$$a = \frac{R_g + d}{2} \quad (29)$$

where R_g is the Grün range shown in Figure 57. For this hemispherical model the temperature rise, ΔT , is:

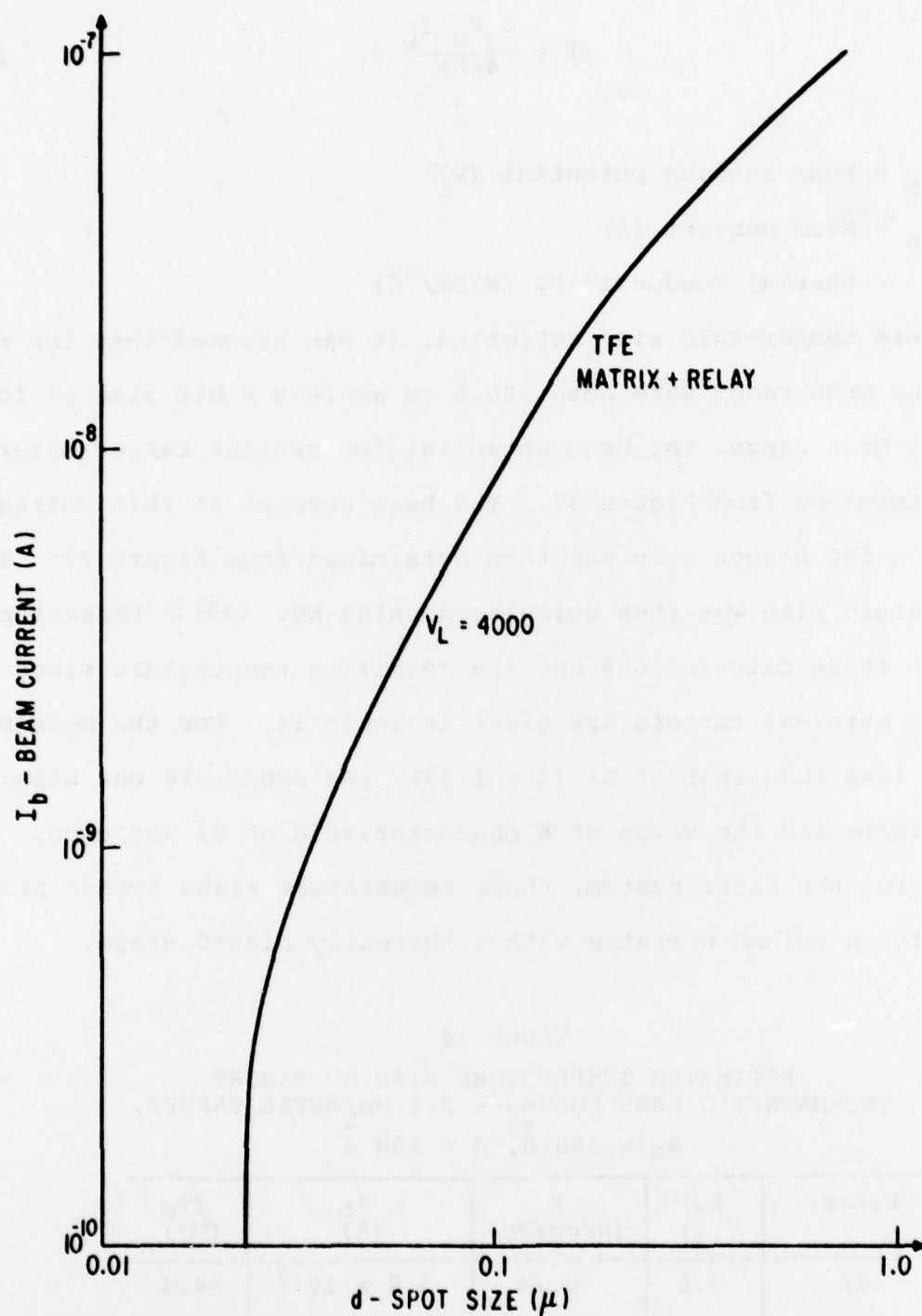


Figure 73. Beam Current vs Spot Size for SFPR Column at Landing Potential of 4000

$$\Delta T = \frac{3 E_o I_b}{4 \pi K a} \quad (30)$$

where

E_o = beam landing potential (V)

I_b = beam current (A)

K = thermal conductivity (W/cm/°C)

For these temperature rise estimates, it was assumed that the spot size and Grün range were both 500 Å to achieve a bit size of 1000 Å. At this Grün range, the beam potential for various target materials was determined from Figure 57. The beam current at this voltage and at a 500 Å spot size was then determined from Figure 72. The temperature rise was then calculated using Eq. (30). Parameters used in these calculations and the resulting temperature rises for various metal-Si targets are given in Table 14. For the metals with K less than that of Si ($K = 1.43$), the substrate was assumed to dominate and the value of K characteristic of Si was used. Except for the Al-Si system, these temperature rises appear practical for a column operated with a thermally biased stage.

TABLE 14
ESTIMATED TEMPERATURE RISE AT TARGET
TWO-MAGNETIC LENS COLUMN - S.I.cm/METAL TARGET,
 $R_g = 500 \text{ Å}$, $d = 500 \text{ Å}$

Element	E_o (kV)	K (W/cm/°C)	I_b (A)	ΔT_o (°C)
In	3.5	0.24	3.8×10^{-7}	44.4
Ga	3.2	0.33	3.2×10^{-7}	34.18
Au	5	2.96	5.8×10^{-7}	46.76
Al	2.0	2.09	10^{-7}	4.56

Temperature rises for the SFPR column were not calculated since the reduction of beam current by a factor of 20 implies a comparable reduction in the temperatures rises, resulting in temperature rises less than 5°C, which would not be usable. More exact estimates of the temperature rise anticipated with the two-lens magnetic column are presented in the alloy junction studies section of this report.

Since the SFPR column does not appear useful for electron writing, it was not studied any further, although it will be investigated in more detail in the forthcoming read optics study, and the aberration properties of the SFPR column will be considered. The two-lens magnetic electron write column is very similar to electron columns used for micromachining [14] and lithography. Ample cases are reported in the literature [15, 16] to verify that spot sizes on the order of 500 to 1000 Å can be held over a 1 mm field with corrected lens/deflection systems.

SUMMARY

The write optics study for ion writing and electron writing was completed during this quarter. It was shown that ion writing was feasible based on present target requirements at a 10 Mbit rate using neon ions at 40 kV. Deflection aberrations of distortion, astigmatism, and coma would limit the field size to approximately 10^7 bits. The extent to which aberration correction can increase this field size will be studied in future phases of this contract if required.

Two possible electron writing columns were studied in detail. These were the all-magnetic two-lens column and the short focus

plus relay matrix lens column. The all-magnetic column appears to have sufficient beam power density to cause local target temperature rises large enough for electron writing if a thermal target bias is used. Estimates of the temperature rise from the beam using a simple hemispherical beam heating model are in 30 to 50°C range for useful target materials. The SFPR matrix column can only achieve about 1/20th of this temperature rise and is therefore not considered useful for alloy junction writing. Deflection aberrations should not limit the all-magnetic electron column field size at the 10^8 bit level.

REFERENCES

1. M.G. Clark, "Interpretation of the Surface Boundary Conditions in the Diffusion Model for NEA Photoemission," Journal of Physics D: Applied Physics, Vol. 9, 1976, pp. 2139-2153.
2. J.F. Gibbons, W.S. Johnson and S. Mylroie, Projected Range Statistics, 2nd ed., Dowden, Hutchinson & Ross, Inc., Stroudsburg, Pa., 1975.
3. H.C. Card, "Collection Velocity of Excess Minority Carriers of Metal-Semiconductor Contacts in Solar Cells," Journal of Applied Physics, Vol. 47, 1976, pp. 4964-4967.
4. F.N. Schwettmann, "Enhanced Diffusion During the Implantation of Arsenic in Silicon," Applied Physics Letters, Vol. 22, 1973, pp. 570-572.
5. W.C. Hughes, Record of the 10th Symposium on Electron, Ion, and Laser Beam Technology, Gaithersburg, Maryland, May 1969, San Francisco Press Inc., San Francisco, Cal., 1969.
6. L.W. Swanson, Proceedings of the Symposium on Advanced Memory Concepts, Stanford Research Institute, Menlo Park, Cal., 1976, p. V-130.
7. R.G. Wilson and G.R. Brewer, Ion Beams with Application to Ion Implantation, John Wiley, New York, 1973.
8. L.W. Swanson, "Comparative Study of the Zirconiated and Built-Up W Thermal-Field Cathode," Journal of Vacuum Science and Technology, Vol. 12, 1975, p. 1228.

9. K. Amboss, Proceedings of the Scanning Electron Microscopy Symposium, IIT Research Institute, Chicago, Ill., April 1976, p. 699.
10. H.G. Parks, et al., Proceedings of the 7th International Conference on Electron and Ion Beam Science and Technology, Washington, D.C., 1976.
11. "Advanced Archival Memory," General Electric Company Proposal to DARPA, Schenectady, N.Y., July 1975.
12. H.G. Parks, MSEE thesis, Syracuse University, Syracuse, N.Y., June 1969.
13. A.B. El-Kareh and J.C.J. El-Kareh, Electron Beams, Lenses and Optics, Vol. 2, Academic Press, New York-London, 1970, p. 256.
14. J.E. Wolfe, "Electron Gun for Data Storage Micromachining," Journal of Vacuum Science and Technology, Vol. 12, No. 6, 1975, p. 1169.
15. T.H.P. Chang, A.D.G. Stewart, Record of the 10th Symposium on Electron, Ion, and Laser Beam Technology, San Francisco Press Inc., San Francisco, Cal., 1969, p. 97.
16. E. Munro, "Design and Optimization of Magnetic Lenses and Deflection Systems for Electron Beams," Journal of Vacuum Science and Technology, Vol. 12, No. 6, 1975, p. 1146.